Investigation of the correlation of electronic and dynamic dislocation properties in ZnO

Dissertation

elektronisches dokument
ULB Sachsen-Anhalt

zur Erlangung des akademischen Grades

doctor rerum naturalium (Dr. rer. nat.)

vorgelegt der

Mathematisch-Naturwissenschaftlich-Technischen Fakultät
(Mathematisch-Naturwissenschaftlicher Bereich)
der Martin-Luther-Universität Halle-Wittenberg

von Serhiy Vasnyov
geb. am 11. April 1974 in Kyiv, Ukraine

Gutachter:
1. PD Dr. habil. H.S. Leipner
2. Prof. Dr. G. Dräger
3. Prof. Dr. J. Christen

Halle (Saale), 26. Oktober 2004

urn:nbn:de:gbv:3-000007406
[http://nbn-resolving.de/urn/resolver.pl?urn=nbn%3Ade%3Agbv%3A3-000007406]

Contents

1 Introduction 1

2 Crystallography of AB compound semiconductors 5
2.1 Zincblende and wurtzite lattice structures 5

3 Dislocations in zincblende and wurtzite lattices 9
3.1 Perfect dislocations in wurtzite lattice 10
3.2 Slip systems in wurtzite lattice 12
3.2.1 Glide dislocation in wurtzite lattice. 14
3.2.2 Core structures of dislocations in the wurtzite lattice 16
3.2.3 Possible super kinks as deduced from the loop model 20
3.3 Partial dislocations in the wurtzite lattice 23
3.3.1 Splitting of the basal perfect dislocations 23
3.4 Structure of fundamental kinks 28
3.4.1 Factors influencing density of fundamental kinks 29
3.5 Dynamical dislocation properties 31
3.5.1 Empirical expression for dislocation velocity 31
3.5.2 Peierls mechanism of dislocation motion 32
3.5.3 Fundamentals of REDG effect 35
3.5.4 Recombination stimulated Peierls mechanism 37
3.5.5 Forces acting on Dislocations 40
3.5.6 Propagation of real glide dislocations 41
3.6 Electrical activity of dislocations 42
3.6.1 Electronic states at dislocations (Read's model) 42
3.6.2 Dislocation recombination activity 44

4 Experimental methods 47
4.1 Sample materials and preparation 47
4.2 Fundamentals of cathodoluminescence mode in SEM 48
4.3 Experimental setup for SEM-CL 50
4.3.1 Kinematical SEM-CL 51
4.4 Description of SEM-CL signal 51
4.4.1 CL contrast of extended defects 53

5 Results and discussions 55
5.1 Investigation of dislocation structures in ZnO 55
5.1.1 As grown dislocation structures 55
5.1.2 Glide dislocations 57
5.1.3 Identification of glide dislocation types 61
5.2 Dislocation dynamics 62
5.2.1 Dislocation movement 62
5.3 Quantitative analysis of dynamics and CL contrast of dislocations 66
5.3.1 Dislocations as recombination centers in ZnO 66
5.3.1.1 Quantitative analysis of CL contrasts of individual single dislocations 66
5.3.1.2 CL contrast behaviour depending on dislocation type 67
5.3.1.3 Revealing of dislocation reactions and CL contrast behaviour 70
5.3.2 Correlated analysis of dynamics and CL contrast properties by means of DCD method 71
5.3.2.1 Introduction to DCD method 71
5.4 Evaluation of dynamic CL contrast behaviour of moving dislocations 76

6 Evidence of different CL contrast and dynamical properties of A(g) and B(g) dislocations 83
6.1 Recombination activity and dynamics of polar A(g) and B(g) dislocations in basal plane slip system 83
6.2 Inversion of glide velocity ratio for A(g) and B(g) dislocations 85

7 Summary and conclusions 89

8 References 93

9 Appendix I
9.1 Refinement of dangling bond densities calculations I
9.2 Peculiarities of CL intensity profile measurement III
9.3 Measurement of CL contrast depending on type of dislocation segments in GaAs IV
9.4 Revealing of Y-luminescence in CdS and ZnSe V
9.5 Abbreviations VI

In Memoriam
my Mother and Father

1 Introduction

ZnO is a rediscovered II/VI semiconductor attracting current interest as a promising wide band gap material for micro and optoelectronic applications such as short wavelength LED LD and electronic nanodevices.

Monocrystalline ZnO has wurtzite lattice structure. Undoped grown bulk crystals show slight n-type conductivity and optical properties in NUV range are governed by excitonic effects even at room temperature. Density of grown-in dislocations has been estimated to be from 10^4 to 10^7 cm^2.

Defect-related real structure appears to be not investigated in greater detail so far. Particularly, representative studies on dislocation structure originating from crystal growth or subsequent materials processing as well as on misfit dislocation configurations are still missing in the literature. Glide dislocations could be identified in various semiconductor materials as very efficient recombination centers which can appear as a limiting factor for the electrical and optical properties by affecting carrier lifetime and corresponding quantum efficiency. Very harmful effect results from recombination-stimulated dislocation dynamics causing extra defect nucleation mechanisms leading to uncontrolled degradation of materials properties.

This work presents a systematic study on structure, dynamics and electrical activity of glide dislocations verified in ZnO bulk crystals. The glide dislocations under consideration are expected to exhibit intrinsic electrical optical properties determined by electronic states originating in dislocation core structure and/or local strain field [reb91]. Scheme in Figure 1 illustrates possible relationship between defect structure and electrical activity.

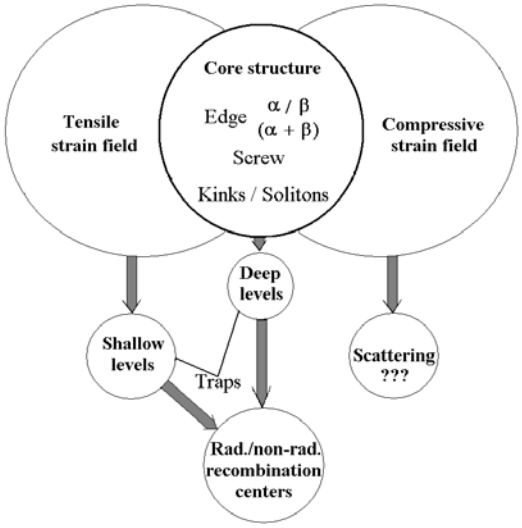

Figure 1. Scheme of possible relationship of dislocation structure comprising core and strain field to defect recombination activity.

Polar character of dislocation core structure as expected in compound semiconductor crystal is considered.

Special issue of the present work is to disclose, for the first time, a certain correlation between structural, dynamic and electrical properties for glide dislocations of different types in crystalline semiconductor. For this purpose, new technique of kinematical SEM-CL has been employed. The tool of kinematical SEM-CL allows to gain correlated results concerning the corresponding dynamic and electrical behaviour of a defect configuration on microscopic scale. High spatial resolution of CL microscopy provides direct access to selected dislocation segments of distinct structural type as emerging in a given dislocation arrangement. This enables a clear distinction of edge- and screw-type dislocation parts or of dislocation line segments with opposite polar core structure, which are collocated in same area. On the other hand, emphasize of consideration can be on the correlation of dislocation dynamics with electrical properties, i.e. any impact of dynamics-related defect structure (missing of decoration, dissociation) on dislocation electronic properties is to be observed. As consequence, very interesting question concerning kinks as possible candidates for carrier recombination centers arises. This difficult problem shall be treated by means of analysing dynamic CL contrast behaviour of moving dislocations in dependence on slip velocity.

The present work starts with a detailed consideration of the fundamentals of dislocation structure in wurtzite type crystal lattices. Basic glide dislocation types are briefly described taking into account distinct core structures and possibility of perfect and partial dislocation configurations if dislocation dissociation is favoured. Models of glide dislocation arrangements like dislocation loops and glide prisms as realized for dislocation propagation on microscopic scale are developed.

Furthermore, in the framework of conventional core structure models the hypothetical arrangements of dangling bonds at the A and B edge atoms are dealt with. In order to get a certain distinction in respect of expected electrical activity of the various dislocation types the line densities of dangling bonds related to the different dislocation types are treated in more detail. As a result of this part of work a dangling bond model of the glide dislocation loop in a basal slip plane will be presented, which illustrates expected variation of electrical activity over the dislocation segments forming the loop structure. Despite of the hypothetical character of the dangling bond model and of recent results of theoretical calculations of dislocation core structures favouring core reconstruction for energetic reasons, the dangling bond model is utilized here as an attempt to quantify differences in electrical activity of dislocation. Finally, this idea holds up also for kink structures.

Following the strategy of this work, an introduction is given to dislocation dynamics based on thermo-activated and recombination-induced (REDG) Peierls mechanism. The REDG effect links up dislocation recombination activity and dynamic behaviour by stimulation of kink dynamics.

Advanced SEM-CL technique have been applied to the dislocation studies in ZnO. New concept of experimental investigation could be realized by employing kinematical CL microscopy to observe correlated dynamic and CL contrast properties of individual defects in context with in-situ micro-deformation and heating-up of sample. Essential advantage of the experiments performed is the yield of information on type-dependent dislocation dynamics on microscopic scale and on simultaneously recorded electrical activity of the defect considered in moving state. Almost all substantial results are documented by means of SEM-CL video movies. The CL movies may be analysed for extracting the correlated dynamic and electrical properties of single defects in given dislocation arrangements A sophisticated new analysing method has been used to handle large series of subsequent CL images. Its basis is the creation of a so-called Dynamic Contrast Diagram (DCD), which reveals patterns representing, at the same time, dynamics and CL contrast behaviour

of selected dislocation segments. This way, the DCD plot leads to contrast-velocity-correlation graphs that indicate dynamics-induced changes of recombination activity of moving dislocations.

Additional very efficient analysing procedure has been made available for determining small changes of CL contrast along a given straight or curved dislocation line in order to find out differences in electrical activity between neighboured dislocation segments of distinct types, responsible for the line shape.

For quantitative discussion of the CL contrast behaviour it will be make use of the method worked out in [hil98] for SEM-CL defect contrast analysis first applied to conventional CL microscopy.

The results obtained by kinematical SEM-CL establish glide dislocations in ZnO as extended mobile recombination centres. Several different glide dislocations with a-type Burgers vector will be identified as electrically active defect structures showing non-radiative carrier recombination. Basal plane as well as prismatic plane slip systems are evidenced and studies on dislocation dynamics under thermal activation and REDG conditions shall be reported. The experimental findings hint at interesting facts regarding single dislocation dynamic behaviour on micrometer scale. Type-dependent CL contrast properties will be proved for the screw- and edge-type dislocations in case of the basal plane slip system. On the other hand, clear difference in recombination activity is shown, for the first time, for the polar A(g) and B(g) edge-type segments. It is worth mentioning, that there is a relationship to the particular dynamic properties observed, too.

Conclusions from contrast-velocity-correlation graphs as derived from DCD patterns result in an exceptional result of great importance. A very weak effect of reduction of CL contrast versus raising slip velocity of dislocation segment is discovered.

Such decrease of recombination activity of the dislocation in dynamic state is unexpected, but may be explained by means of kink dynamics.

2 Crystallography of AB compound semiconductors

2.1 Zincblende and wurtzite lattice structures

Chemical compounds $A^{II}B^{VI}$ and $A^{III}B^{V}$ which are formed from elements of groups II-VI and III-V, respectively, are crystallized in different polymorphic modifications. These compounds may belong to two general structural groups such as cubic zincblende (ZB) structure and hexagonal wurzite (WZ) structure. The topic of current chapter is to describe the crystal structures and pointing out polarity, as well as to consider the origin of dislocations with different core structures and their behaviour as glide dislocations in the crystal lattice. Figure 2 illustrates similarity and difference in stacking order along [111] and [0001].

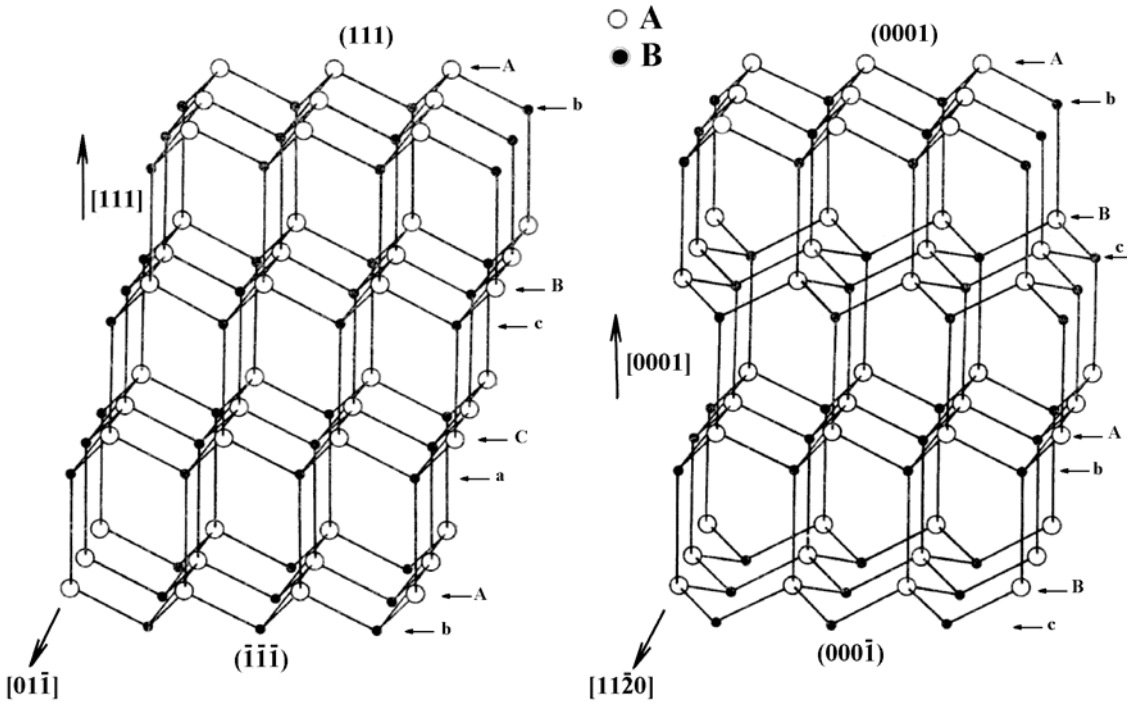

a) b)

Figure 2. Crystal lattices of zincblende (a) and wurtzite (b) structure.

CdTe and GaAs are examples of $A^{II}B^{VI}$ and $A^{III}B^{V}$ compounds which can be crystallized in zincblende lattice. The space group of these compounds corresponds to $F\bar{4}3m$ [schr89a]. Figure 3 shows a zincblende unit cell. Letters A and B denote the metal and non-metal atoms respectively.

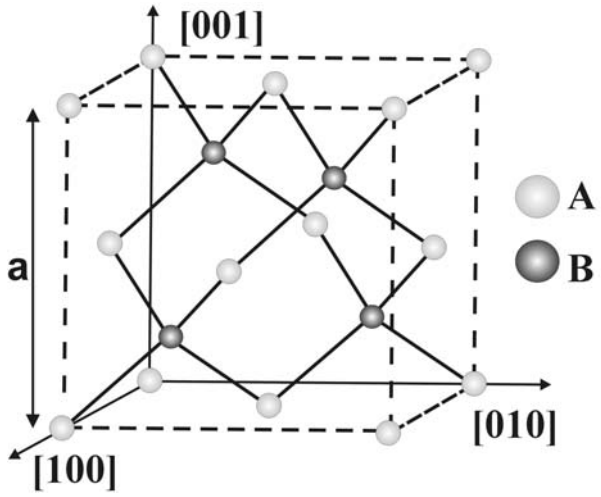

Figure 3. Spatial arrangement of atoms in the zincblende unit cell. Here a≡ lattice constant.

The unit cell consists of four AB molecules made up by those atoms, which are placed at sites with coordinates: 4A at 0,0,0; 0,½,½; ½,½,0; ½,0,½; and 4B at ¼,¼,¼; ¼,¾,¾; ¾,¼,¾; ¾,¾, ¼. The point symmetry in A and B positions corresponds to $\bar{4}3m$. Each atom A(B) has four neighbouring atoms B(A) located in the corners of a perfect tetrahedron in distance $a \cdot \frac{1}{4}\sqrt{3}$, where a is the cubic lattice constant. Each atom A(B) is surrounded by twelve atoms of the same kind, which are the second order neighbours in distance $a \cdot \frac{1}{2}\sqrt{2}$.

An important peculiarity of the zincblende structure is that it does not have a centre of inversion symmetry. The layers A-B (or tetrahedra AB_4) are along <111> directions. As a consequence, zincblende crystals show polar properties, such as distinct planes of opposite orientations (*hkl*)↔(*-h-k-l*) may have A or B termination. The antiparallel directions [hkl]↔[-h-k-l] are not equivalent. The polarity of lattice structure results in pronounced anisotropy of physical and chemical materials properties.

$A^{II}B^{VI}$ and $A^{III}B^{V}$ compounds can also be crystallized in the wurtzite structure. The space symmetry group of such lattice corresponds to $P6_3mc$. In Figure 4 a wurtzite structure unit cell exhibiting "*a*" and "*c*" lattice constants is shown. One unit cell contains two molecules of AB, whose the atomic positions are 0,0,0; 1/3,2/3,1/2 for A and 0,0,*u*; 1/3,2/3,1/2+*u* for the B atom, where $u \approx 3/8$.

The wurtzite structure can be considered as a hexagonal closed-packed stacking of atoms of elements from the group B with atoms of elements of the group A in the tetrahedral interstitial positions of one kind. Such a stacking causes a polarity, thus the "*c*"-axis [0001] has polar character in the wurtzite structure.

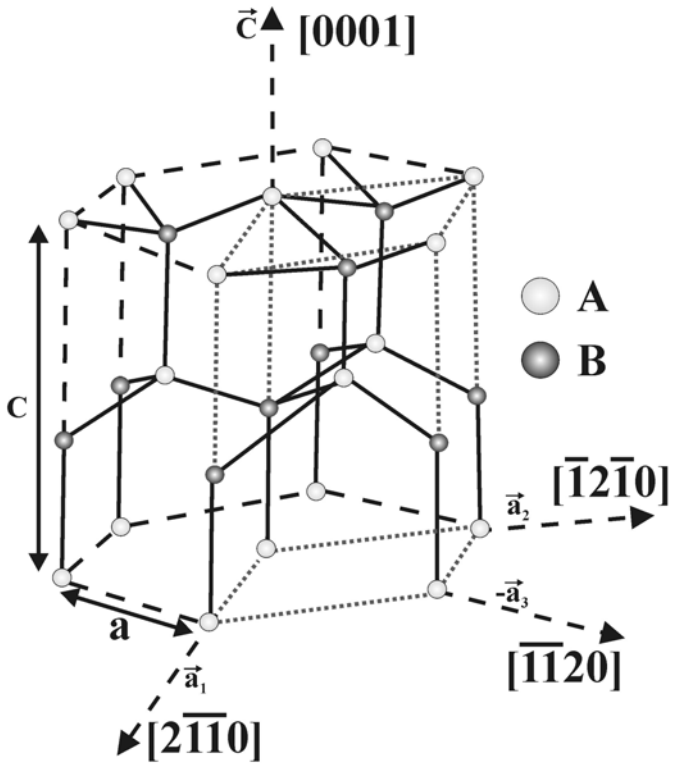

Figure 4. Spatial arrangement of atoms in the wurtzite unit cell, a_1, a_2, a_3, c≡lattice constants.

From the locations of atoms in the wurtzite unit cell it is seen, that each A atom is bound to four B atoms in the corners of a tetrahedron: one in distance *uc*, and the three others in the distance $[(1/3)a^2+c^2(u-1/4)^2]^{1/2}$. Each atom is surrounded by twelve neighbouring atoms of second order: six of them in the corners of hexagon (at the same plane as the atom considered) in distance *a*, and the others six are in corners of trigonal prism in the distance $[(1/3)a^2+(1/4)c^2]^{1/2}$.

In the crystals of wurtzite structure as well as in the case of zincblende structure, one can imagine the polarity of oppositely charged ions A^{II} and B^{VI} as a network of dipole moments. The dipole moments are not compensated in the wurtzite lattice, and as a result the single polar axis is formed. Consequently, wurtzite crystals are capable to show as piezoelectric as piroelectric properties.

3 Dislocations in zincblende and wurtzite lattices

In the zincblende and wurtzite structures, which consist of close packed double layers Ab-Bc-Ca and Ab-Bc-Ab, respectively the {111} and {0001} may be regarded as preferred planes in which lattice slip processes can proceed.

In Figure 5 dislocation glide is demonstrated to be realized in two parallel slip planes differing in their positions indicated as “glide-set” (ss) and “shuffle-set” (gs), respectively.

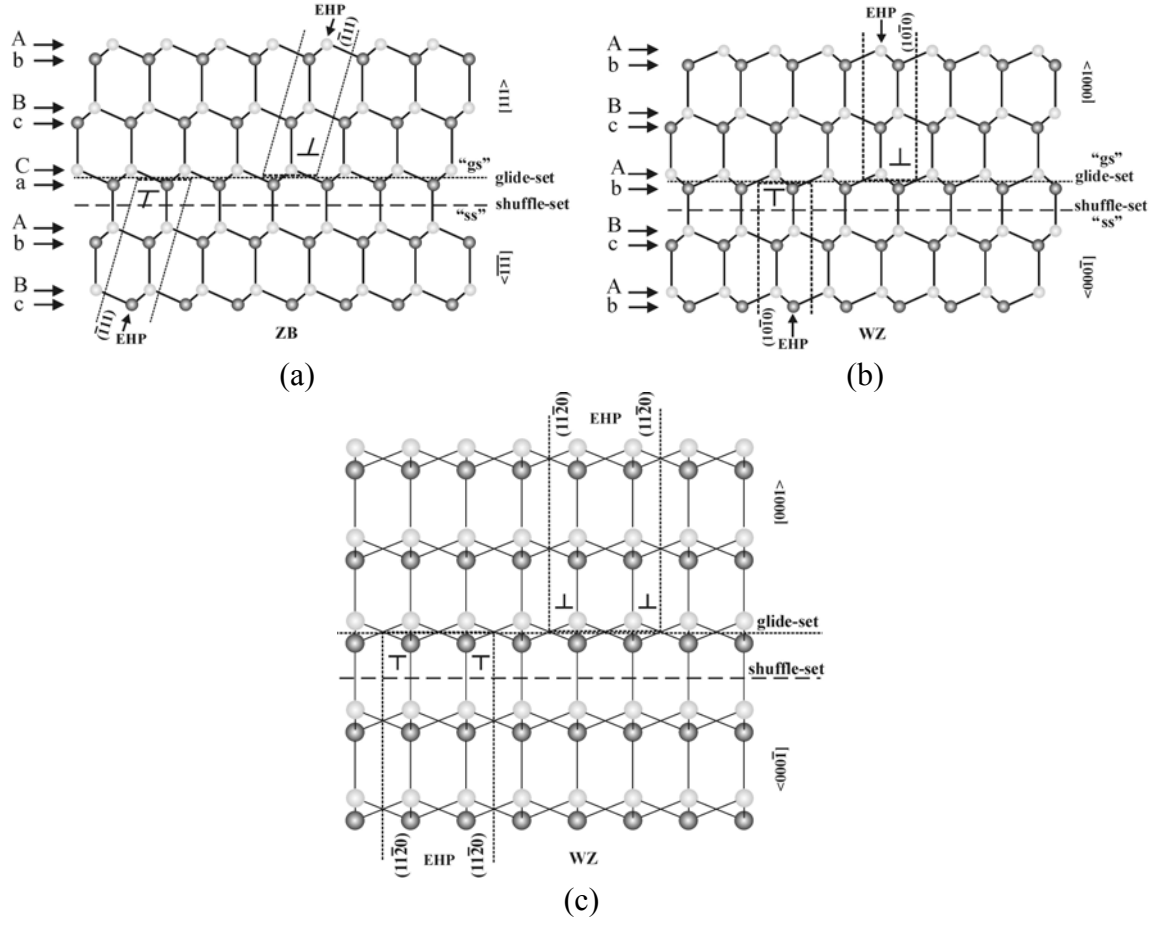

Figure 5. Extra half planes (EHP) terminating on shuffle- and glide-set slip plane of ZB and WZ type lattices. (a) EHP (-111), (b) EHP(10-10), (c) Double EHP (11-20).

Consequently, the extra lattice plane defining an edge dislocation may come about in two modifications as glide-set and shuffle-set [hir82]. They end up in distinct atomic positions as can be deduced from Figure 5. Thus, depending on using ss or gs-type of slip plane, the dislocation core is made up by A or B atoms, respectively. These edge atoms define the A or B polarity of core structure in the ZB and wurtzite WZ structure crystal lattice.

It must be mentioned that if the dislocation turns from gs⇔ss, the polarity of core structure is inverted. The Huenfeld Convention [proc79] gives the following definitions:

Table 3-1.: The Huenfeld convention for polar core structures [proc79].

Glide-set	EHP termination	EHP termination	Shuffle-set
B(gs)	B^{gs}_{core}	A^{ss}_{core}	α
A(gs)	A^{gs}_{core}	B^{ss}_{core}	β

The nucleation and propagation of the perfect glide dislocations is believed to occur in between the neighboured layers of the ss planes. It has to be noted, that the number of dangling bonds is less for dislocations in the ss plane in comparison with that ones situating in gs plane. The dangling bonds in ss configuration are perpendicular to the glide plane. Unlike the shuffle-set core, the dislocations of glide-set configuration have three inclined dangling bonds per core atom and there is a higher probability for dangling bond reconstruction. The properties of dislocations in semiconductors - not only their mobility but also especially their possible electronic states in the band gap - must depend on the configuration realised.

In the earlier works, it was supposed [hor58, hol62] that dislocations are situated in the shuffle-set, but further works [due95, lou87] have came to the conclusion that dominating for the mobile dislocations are the glide-set planes. Main confirmation for this results from transmission electron microscopy (TEM) revealing gliding dislocations to be split up, that indicates gs glide planes to be involved, it is too difficult for dislocations to dissociate being in shuffle-set planes.

3.1 Perfect dislocations in wurtzite lattice

A detailed analysis has been performed for hypothetically possible types of perfect dislocations in the wurtzite lattice structure in [osip68a]. This work has also pointed out possible electrical activity of the dislocations, depending on the number of broken bonds and atomic polarity of the core structures in various dislocation types.

The smallest translation vectors in the wurtzite structure are the two lattice vectors: $\boldsymbol{a} = 1/3 < \bar{1}2\bar{1}0 >$ and $\boldsymbol{c} = <0001>$. The line directions of simple dislocations types are $< \bar{1}2\bar{1}0 >$ and <0001>. Arbitrary directions in crystals with wurtzite lattice can be treated as a combination of steps of these directions. Thus, for instance, a dislocation in the $[\bar{1}\bar{1}01]$ direction consists of steps in the $[\bar{1}2\bar{1}0]$, the $[\bar{2}110]$, and the $[0001]$ directions, which may be written as:

$$[\bar{1}\bar{1}01]=\frac{1}{3}[\bar{1}2\bar{1}0]+\frac{1}{3}[\bar{2}110]+[0001]$$

Dislocations in the $[\bar{1}2\bar{1}3]$ direction consist of steps in the $[\bar{1}2\bar{1}0]$ and the [0001] directions:

$$\frac{1}{3}[\bar{1}2\bar{1}3]=\frac{1}{3}[\bar{1}2\bar{1}0]+[0001]$$

At such a choice of dislocation directions and Burgers vectors, the types of simple dislocations are: screw-type dislocations with the Burgers vector $\boldsymbol{a}$, screw-type with the Burgers vector $\boldsymbol{c}$, and two types of edge dislocations, and a 60^{o} dislocation.

In case of an ***a***–type of dislocations (see Figure 7), splitting into two partial dislocations is possible as schematically shown in Figure 6. Vectors **Aσ, σB** are the Burgers vectors of partial dislocations corresponding to the **AB, AC, AD** Burgers vectors of perfect dislocations.

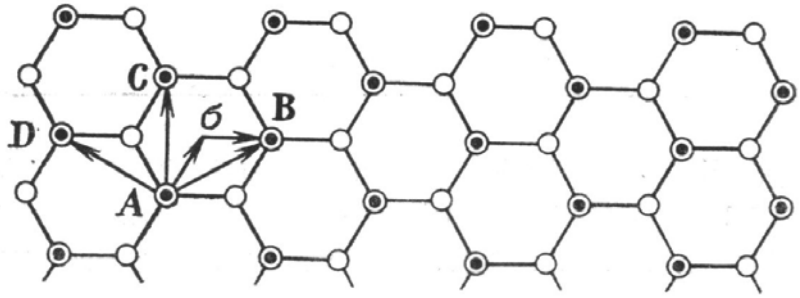

Figure 6. Schematic presentation of wurtzite structure in (0001) plane with vectors of perfect dislocations AB, AD, AC and vectors of partial dislocations **Aσ**, **σB**.

There exist additional possible Burgers vectors and directions for dislocation axes in the wurtzite lattice.

The Table 3-2 presents dislocations whose Burgers vectors and axes point along directions lying all in the basal $\{0001\}$ or in the prismatic planes $\{10\bar{1}0\}$ and $\{11\bar{2}0\}$, which are the glide planes of the dislocations.

Table 3-2.: Possible glide dislocation in wurtzite lattice [osip68].

No.	Axis ξ	Burgers vector $\boldsymbol{b}$	Angle between ξ and $\boldsymbol{b}$	Glide plane
1	$<\bar{1}2\bar{1}0>$	$1/3<\bar{1}2\bar{1}0>$	0^o	-
2	<0001>	<0001>	0^o	-
3	$<\bar{2}110>$	$1/3<\bar{1}2\bar{1}0>$	60^o	{0001}
4	<0001>	$1/3<\bar{1}2\bar{1}0>$	90^o	$\{10\bar{1}0\}$
5	$<\bar{1}2\bar{1}0>$	<0001>	90^o	$\{10\bar{1}0\}$
6	$<\bar{1}100>$	$1/3<\bar{1}2\bar{1}0>$	30^o	{0001}
7	$<\bar{1}010>$	$1/3<\bar{1}2\bar{1}0>$	90^o	{0001}
8	$<\bar{1}100>$	<0001>	90^o	$\{11\bar{2}0\}$
9	$<\bar{1}2\bar{1}3>$	$1/3<\bar{1}2\bar{1}0>$	$58^o24'$	$\{10\bar{1}0\}$
10	$<\bar{1}2\bar{1}3>$	<0001>	$31^o36'$	$\{10\bar{1}0\}$
11	$<\bar{1}10\bar{1}>$	<0001>	43^o	$\{11\bar{2}0\}$
12	<0001>	$<\bar{1}100>$	90^o	$\{11\bar{2}0\}$
13	$<\bar{1}101>$	$<\bar{1}100>$	47^o	$\{11\bar{2}0\}$

The types of dislocations are given in this table by the angles between axes ξ and directions of Burgers vectors $\boldsymbol{b}$.

3.2 Slip systems in wurtzite lattice

From Table 3-2 following slip systems can be combined (Figure 7):

1) $\{0001\} < \bar{1}2\bar{1}0 >$
2) $\{11\bar{2}0\} < \bar{1}100 > , < 0001 >$
3) $\{10\bar{1}0\} < \bar{1}2\bar{1}0 >$,<0001>

Theory [hir82, fra49] shows that for a distinct crystal lattice only these directions and glide planes with small Miller indices will be observed. From the Frank criteria and Peierls stress definition it follows that only perfect dislocations having the Burgers vectors $1/3 < 11\bar{2}0 >$, <0001> and $1/3 < 11\bar{2}3 >$ are stable in crystals with wurtzite lattice and, therefore, can contribute to glide processes. Furthermore, according to eq. (23) Peierls stress is minimal for the dislocations with shortest Burgers vector. Such dislocations have to move easier than that ones with longer Burger vectors. Also, from eq. (23) follows that for the dislocations with a fixed Burgers vector the Peierls stress is minimal at glide planes with maximal plane spacing *d* between neighbouring planes. Planes for dislocation slip are the planes with largest distance *d*. These planes are usually close-packed in the structure under consideration and have smallest Miller indices. Therefore, the magnitude of Peierls stress calculated for a distinct glide system is chosen as a rough indicator for whether the glide system has a preference to be involved into dislocations glide processes under the fixed conditions.

More glide systems expected as theoretically possible for the semiconductor compounds with wurtzite structure are listed in Table 3-3.

Table 3-3.: Possible glide systems expected for the wurtzite structure.

N°	Glide system
1	$\{0001\} < 11\bar{2}0 >$
2	$\{10\bar{1}0\} < 11\bar{2}0 >$
3	$\{10\bar{1}0\} < 0001 >$
4	$\{10\bar{1}1\} < 11\bar{2}0 >$
5	$\{10\bar{1}1\} < 11\bar{2}3 >$
6	$\{11\bar{2}0\} < 0001 >$
7	$\{11\bar{2}2\} < 11\bar{2}3 >$

Table 3-4.: Burgers vector length b in ZnO with the lattice constants as given in [cim64].

direction	type	b, Å
$< 0001 >$	***c***-type	5,2066
$< 11\bar{2}0 >$	***a***-type	3,2495
$< 11\bar{2}3 >$	(***a***/***c***)-type	6,1374

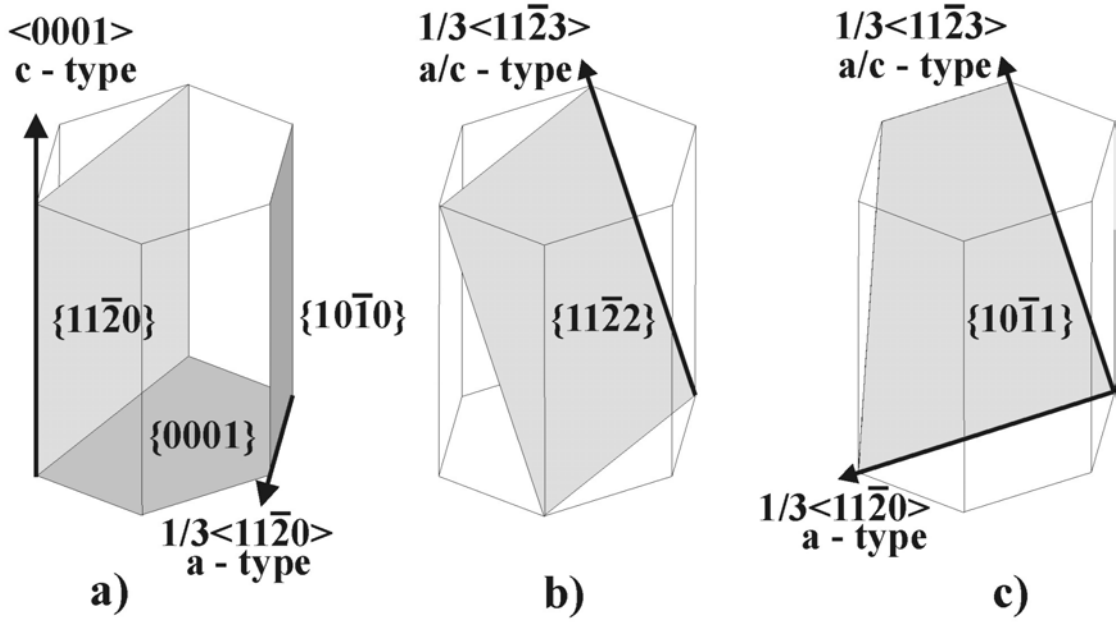

Figure 7. Scheme of glide systems in the wurtzite structure [jahn98].

For a wurtzite lattice the plane spacing d is expressed by Miller indices as:

$$\frac{1}{d^2} = \frac{4}{3}\frac{h^2 + hk + k^2}{a^2} + \frac{l^2}{c^2} \qquad (1)$$

Using the eq. (1) and the values for lattice constants *a* and *c* [cim64] the spacing d for the planes mentioned in Table 3-3 can be calculated. Now, based on calculated plane spacing *d* and values of Burgers vector lengths b from Table 3-4, using eq. (23), it is easy to get the values of Peierls stress. The complete results of latter calculations are given in Table 3-5.

Table 3-5.: Results of calculations of plane spacing d, ratio (d/b) and normalized Peierls stress $\sigma = \sigma_p / \sigma_{\{11\text{-}22\}}$.

Plane	d, Å	b, Å	d/b	σ
{0001}	2,603	3.250	0.801	56.18%
$\{10\bar{1}0\}$	2,814	3.250	0.866	52.65%
$\{10\bar{1}0\}$	2,814	5.207	0.540	72.91%
$\{10\bar{1}1\}$	2,476	3.250	0.762	58.43%
$\{10\bar{1}1\}$	2,476	6.137	0.403	83.63%
$\{11\bar{2}0\}$	1,625	5.207	0.312	91.62%
$\{11\bar{2}2\}$	1,378	6.137	0.225	100.00%

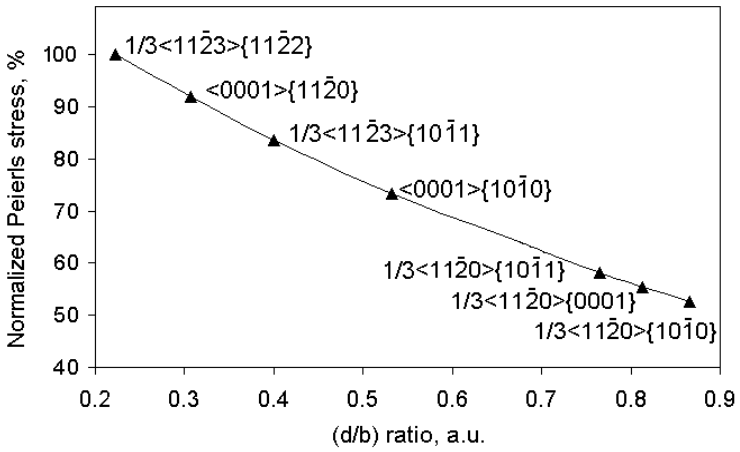

Figure 8. Normalized Peierls stress as a function of the ratio of slip plane spacing d to Burgers vector length b for the glide systems shown in Figure 7.

As can be seen from the plot in Figure 8, the glide systems having higher Peierls stress have to sequentially ruled out from glide processes. This approach is based on the theory of elasticity, which deals with characteristics of dislocations such as Burgers vector length b and plane spacing *d*. The theory takes also into account the elastic characteristics of materials such as shear modulus G and Poisson's ratio *ν*. However, one has to note, that this approach does not consider the dislocation core structures.

3.2.1 Glide dislocation in wurtzite lattice.

From the Table 3-2, the slip systems

1) $\{0001\} < \bar{1}2\bar{1}0 >$
2) $\{11\bar{2}0\} < \bar{1}100 >, < 0001 >$
3) $\{10\bar{1}0\} < \bar{1}2\bar{1}0 >, < 0001 >$

have been chosen to describe dislocation propagation.

These slip systems are expected to be activated in case of plastic deformation by dislocations glide processes. The glide dislocations should develop expanding loop structures to propagate the dislocations in the slip planes. Based on the data in Table 3-2, the models of dislocation loop structures for the slip systems above are proposed as shown in Figure 9.

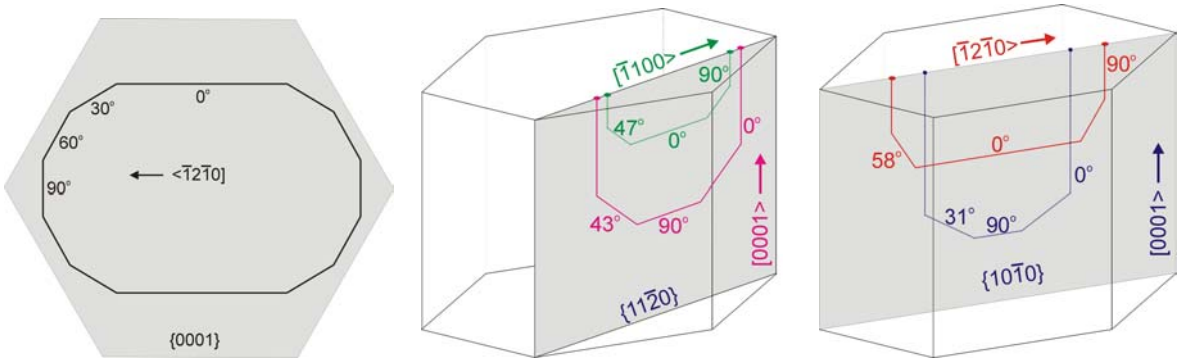

(a) (b) (c)

Figure 9. Possible loop structures for main glide systems in the wurtzite lattice. (a) basal slip plane, (b), (c) prismatic slip planes.

A closed dislocation loop which is formed by 90°-,60°-, 30°- and screw line parts of β-type dislocation in {0001} basal plane is drawn in Figure 9 (a). Same loop structures appear for all $[11\bar{2}0]$ directions in {0001}. The dislocation loop structures of the prismatic slip systems are displayed in Figure 9 (b) and (c). According to the distinct slip systems two kinds of loop structures may occur in the corresponding $\{11\bar{2}0\}$ and $\{10\bar{1}0\}$ glide planes. The existence of these dislocation loop structures in ZnO crystals will be discussed, for the first time, based on the experimental findings derived.

Local plastic deformation as realised by micro-indentation or scratching requires very detailed considerations and analyses of simultaneously activated slip systems. Zones of local plastic deformation around a micro-indent may be analysed in the framework of the glide prism conception [hu75]. Glide prism models proposed for slip processes during indentation on {111} and {110} surfaces of samples with ZB structure are known from literature [schr99], but, there is no detailed work on the complex geometry and dislocation configurations of the active slip systems in the other cases.

Figure 10 (a, b) presents models of possible glide prism configurations, which may be referred to dislocation rosettes built around the indentation sites on {0001} and $\{10\bar{1}0\}$ crystal surfaces. These models can be used to explain the geometry of the real dislocation rosette arms formed.

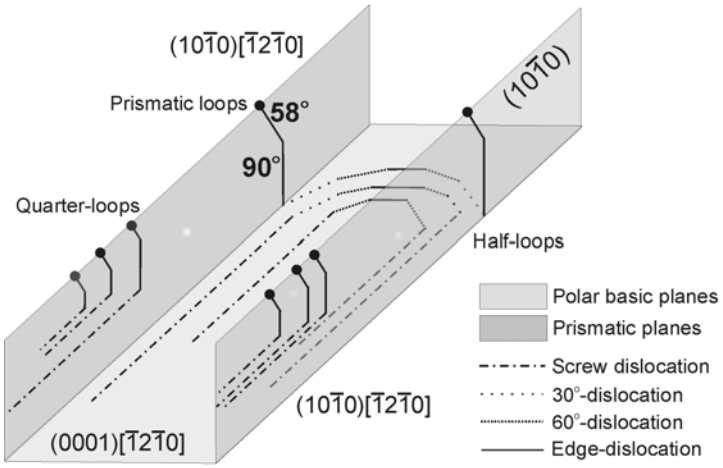

(a)

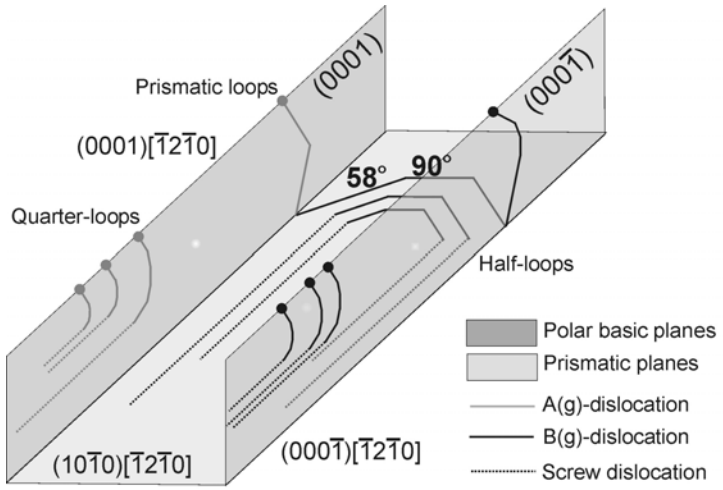

(b)

Figure 10. Models of possible glide prism configurations. Glide prism configuration for local deformation on {0001} planes (a), and on {10-10} planes (b) in wurtzite lattice.

The glide prisms shown as constructed by three corresponding slip planes allowing material to be pushed out within the prism area by strain pointing along the prism axis. Correlated dislocation slip in a glide prism occurs simultaneously in the two surface-perpendicular glide planes and in the surface-parallel glide plane as well. Assuming the formation of the dislocation loop structures mentioned above, threading dislocations are produced and surface parallel dislocation half loops may be generated. In consequence of reactions between the dislocation loop structures propagating in the distinct slip systems prismatic loops made up by two threading segments and a connected surface–parallel line part can be built. A verification of the proposed glide prism configurations and recognition of the type of the slipping dislocation structures is still open issue, which is dealt with in the experimental studies presented.

3.2.2 Core structures of dislocations in the wurtzite lattice

For the perfect screw, 30°, 60° and 90°-type dislocation segments gliding in basal plane (0001) models of core structures have been developed by the authors in [osip68]. A detailed insight into the core configurations is given in Figure 11 - Figure 14.

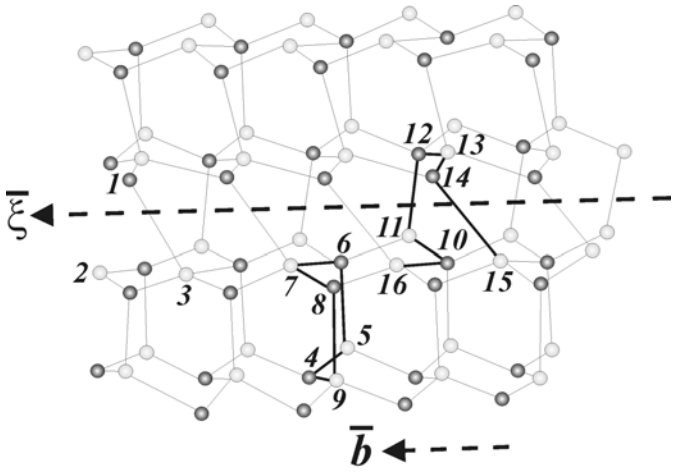

Figure 11. Screw dislocation core structure with the 1/3[-12-10] Burgers vector. ξ axis, $\boldsymbol{b}$ Burgers vector.

Figure 11 shows the core structure of a screw dislocation with $1/3[\bar{1}2\bar{1}0]$ Burgers vector. This screw dislocation may be understood as a result of the displacement of basal planes with respect to each other. The vector 2-3 is the displacement vector. Comparing the undisturbed hexagon 9-4-5-6-7-8-9 and the circuit 16-10-11-12-13-14-15, the screw character of the dislocation can be clearly seen. In first case, the circuit is closed – atom 4 locates at the beginning and the end. In second case, the circuit is non-closed between 15-16. The vector 15-16 is the Burgers vector of this dislocation with the direction $[1\bar{2}10]$. It is seen from this core model that the dislocation has no dangling bonds.

In Figure 12 the model of a 60° dislocation core in shuffle-set state is presented. Its direction ξ and the Burgers vector $\boldsymbol{b}$ form the 60° angle between themselves. In this case, the Burgers vector is $1/3[\bar{1}2\bar{1}0]$ and the direction of the dislocation line is $\xi=[2\bar{1}\bar{1}0]$. Its edge-type component is clearly seen; an extra half plane can easily be assigned to the dislocation. The extra half plane $(01\bar{1}0)$ is indicated by heavy lines in this figure. The ss glide plane of this dislocation is (0001). It is seen that the extra half plane ends along ξ in row of the A atoms with single dangling bonds. A dislocation with the opposite sign will end in row of B atoms with single dangling bonds.

In this regard the basal planes of the wurtzite structure are analogous to the planes of type {111} in the zincblende structure, where there are two kinds of 60^o dislocations depending on the type of atoms, which form the edge of the extra half plane.

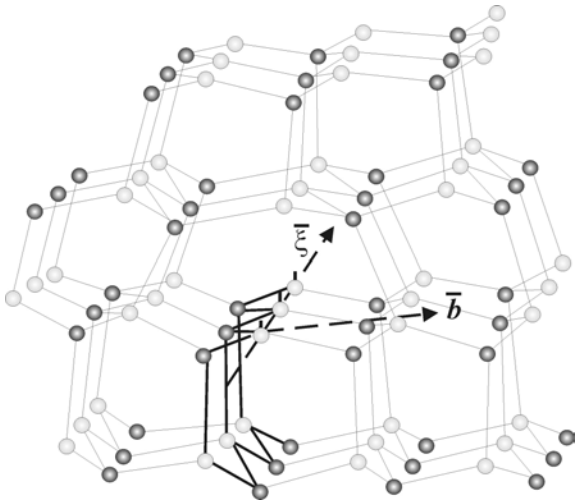

Figure 12. 60^o dislocation: ξ axis, $\boldsymbol{b}$ Burgers vector, EHP (-1010).

The 30^o dislocation model is shown in Figure 13. It has a considerable screw-type component, as can be seen from the distorted circuit drawn with bold lines. Its extra half plane is the $(11\bar{2}0)$-type plane. Along the $<\bar{1}100>$ dislocation axis the atoms of A(B) kind with single broken bonds are located.

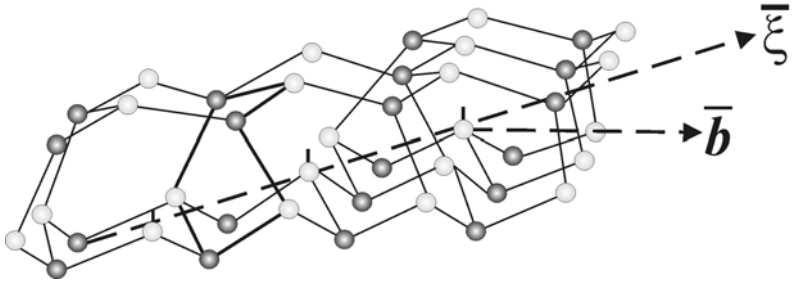

Figure 13. 30^o dislocation: ξ axis, $\boldsymbol{b}$ Burgers vector.

The model of an edge dislocation in the basal plane is shown in Figure 14. Along its axis $<\bar{1}010>$ the traces of the two parallel extra half planes $(11\bar{2}0)$ are lying, which result in parallel rows of A(B) edge atoms.

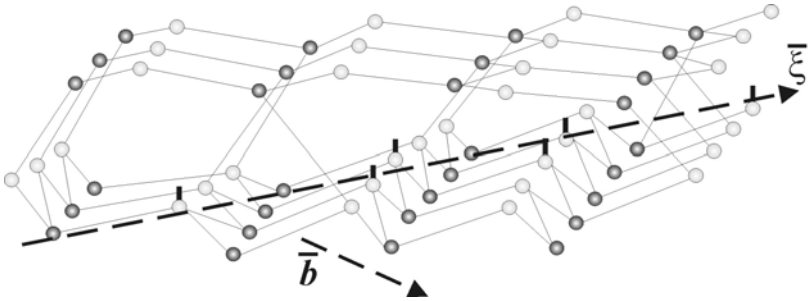

Figure 14. Edge dislocation with (0001) glide plane in wurtzite lattice. ξ axis, $\boldsymbol{b}$ Burgers vector.

Similar models of core structures are available for all dislocation types listed in Table 3-2. Utilizing these models gives a possibility to reveal the core structure characteristics of the complete set of dislocations as seen in the right-hand columns in Table 3-6. Here, the column called as "Types of core atoms" denotes the types and sequences of atoms at rows forming corresponding dislocation cores. For instance, indices A-B||B-A mean sequentially varying types of atoms placed along two parallel rows, while such notation as A-A||B-B denotes two parallel rows with atoms of distinct type.

These four additional columns describe the types of atoms terminating the extra half planes, the dangling bond line density calculated by means of the scheme explained in Figure 16 (a), and the polarity revealed in the shuffle-set configuration.

Table 3-6.: Extended table of dislocation glide systems with indications of core structure polarity

No.	Axis ξ	Direction of Burgers vector $\boldsymbol{b}$	Angle between ξ and $\boldsymbol{b}$	Glide plane	Extra half plane	Types of core atoms	Dangling bond line density, 1/a	Polar type
1	$<\bar{1}2\bar{1}0>$	$<\bar{1}2\bar{1}0>$	0°	-		-	0	
2	<0001>	<0001>	0°	-		-	0	
3	$<\bar{2}110>$	$<\bar{1}2\bar{1}0>$	60°	{0001}	$(10\bar{1}0)$	A-A	1	α (β)
4	<0001>	$<\bar{1}2\bar{1}0>$	90°	$\{10\bar{1}0\}$	$(11\bar{2}0)$	A-B		(α + β)
5	$<\bar{1}2\bar{1}0>$	<0001>	90°	$\{10\bar{1}0\}$		A-A||B-B		(α + β)
6	$<\bar{1}100>$	$<\bar{1}2\bar{1}0>$	30°	{0001}	$(11\bar{2}0)$	A-A	0.577	α (β)
7	$<\bar{1}010>$	$<\bar{1}2\bar{1}0>$	90°	{0001}	$(11\bar{2}0)$	A-A||A-A	1.154	α (β)
8	$<\bar{1}100>$	<0001>	90°	$\{11\bar{2}0\}$		B-A||A-B		(α+β) and (β+α)
9	$<\bar{1}2\bar{1}3>$	$<\bar{1}2\bar{1}0>$	58°24'	$\{10\bar{1}0\}$		B-B||A-A		(α + β)
10	$<\bar{1}2\bar{1}3>$	<0001>	31°36'	$\{10\bar{1}0\}$		B-B-||A-A		(α + β)
11	$<\bar{1}10\bar{1}>$	<0001>	43°	$\{11\bar{2}0\}$		B-B||A-A		(α + β)
12	<0001>	$<\bar{1}100>$	90°	$\{11\bar{2}0\}$		A-B||B-A		(α+β) and (β+α)
13	$<\bar{1}101>$	$<\bar{1}100>$	47°	$\{11\bar{2}0\}$		B-B||A-A		α and β

The configurations and types of atoms terminating the extra-half planes in edge-type dislocations as drawn in the Figure 12 - Figure 14 yield the complex behaviour of the polarities of different dislocation cores as well as the differences in the densities of dangling bonds. The latter follows from the distances between the core atoms along the traces of the extra-half planes in the {0001} slip plane. The diagram in Figure 15 shows the different dangling bond densities estimated in dependence on dislocation type.

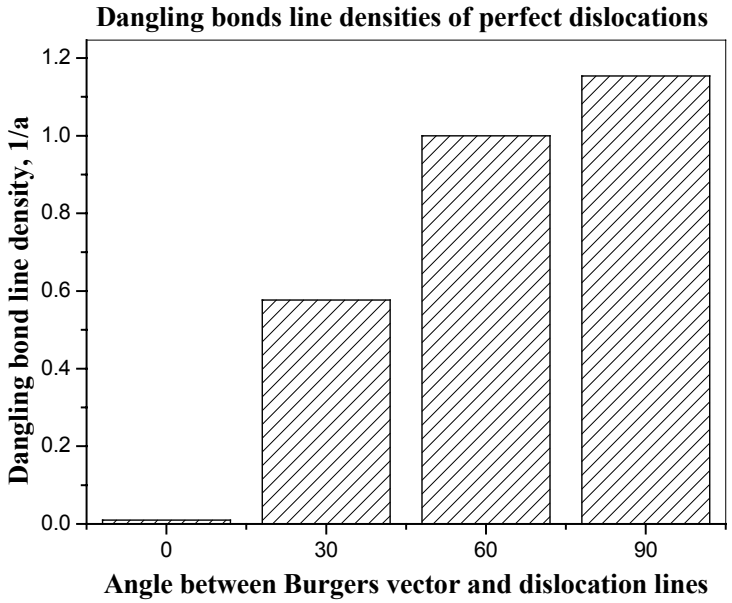

Figure 15. Dangling bond line densities for different perfect ***a***-type dislocations in basal plane.

The gradual increase of line bond density with the raise of the angle between Burgers vector and dislocation line is seen. The 90° dislocation should possess the highest calculated bond density.

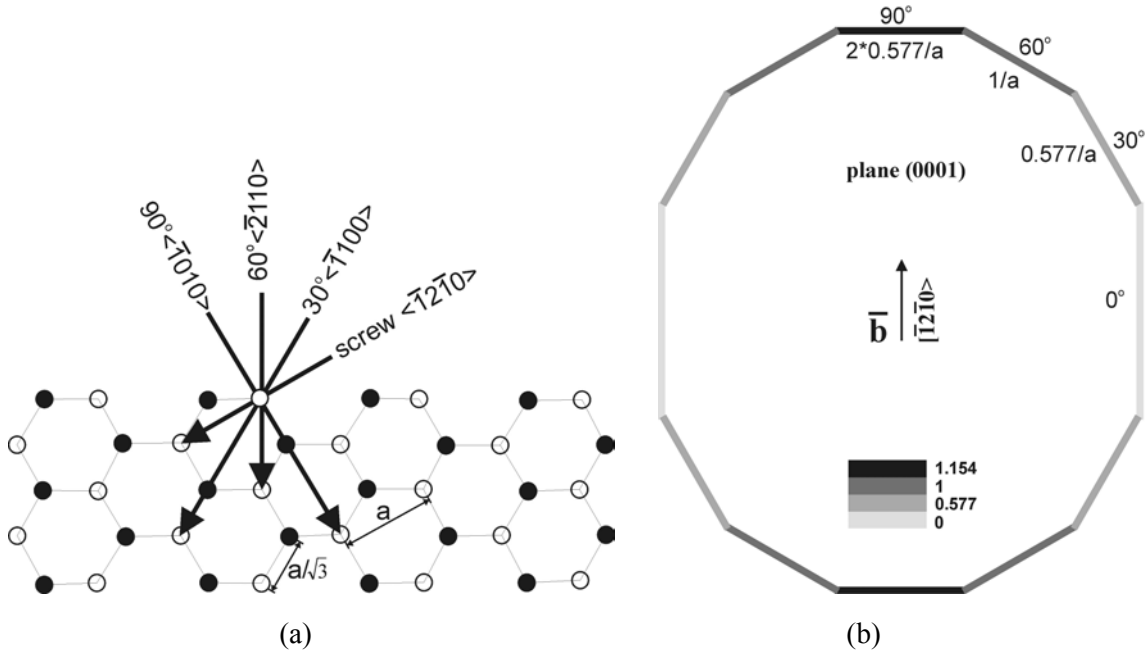

(a) (b)

Figure 16. (a) Scheme for counting of dangling bonds per lattice constant length along certain dislocation line directions shown by the arrows. (b) Calculated dangling bond line density of 0°, 30°, 60° and 90° dislocation segment in relation to their position in dislocation loop structures.

In Figure 16 (b) the dangling bond density for the distinct segments of the dislocation loop lying in basal plane is shown. This picture represents in a grey scale how the distribution of the dangling bond density should vary systematically over the entire loop. It can be seen from this scheme that the edge segment of the loop has the largest magnitude of possible dangling bond

density. The dangling bond density is believed to be related to the electrical activity of dislocations. Thus, the dislocation loop should exhibit varying recombination behaviour depending on type of the line segment considered.

As it could also be seen from the Figure 16 (a) the screw segment possesses exactly the same length of period in the arrangement of atoms along the dislocation line as that one of 60^o-type dislocation segment. But nevertheless, electrical activity of the screw is believed to be lower in comparison to a 60^o dislocation because the former has no broken bonds as deduced from Figure 11. It is supposed that the dangling bond line density equals to zero in our model.

3.2.3 Possible super kinks as deduced from the loop model

Based on the model of dislocation loop structure in Figure 9 (a), possible super kink configurations as shown in Figure 17 can be proposed. Symmetrical as well as asymmetrical double super kinks can be formed depending on type of the dislocation line part considered. The distinct segments belonging to the super kink have different dangling bond densities.

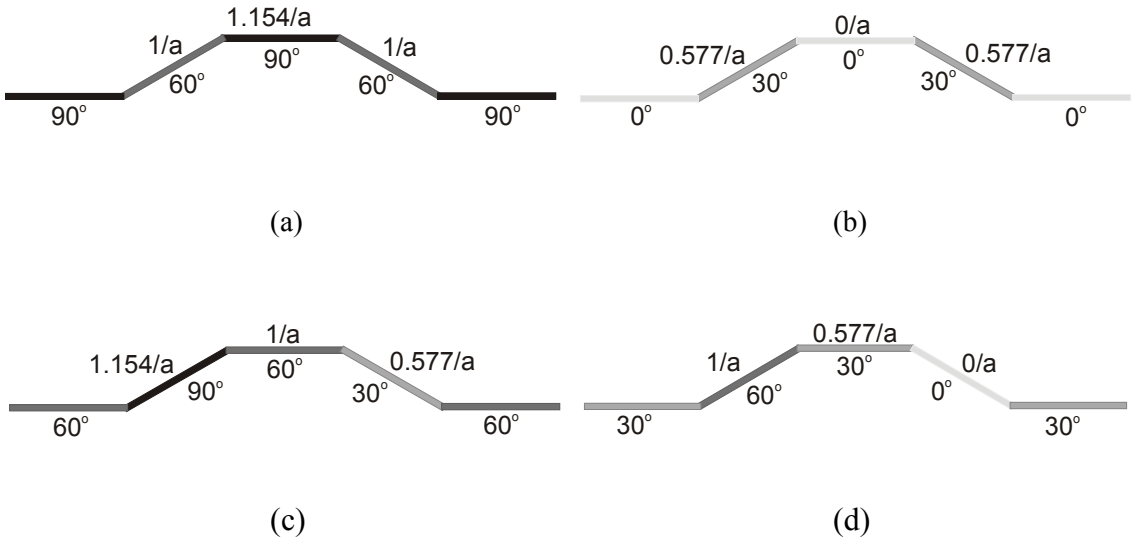

Figure 17. Possible geometrical kink configurations for perfect basal dislocations in wurtzite structure. Symmetrical super kinks at the edge (a) and the screw (b), and non-symmetrical ones at the 60^o (c) and 30^o (d) perfect dislocations.

Thus, the integral bond density of the super kinks is altered compared to the originating dislocation line (let us mark it by index "m"). For instance, super kinks formed along an original 60^o dislocation line (Figure 17 (c)), the average dangling bond density of the super kink part will be determined by the total number of dangling bonds coming from segments of 30^o- and 90^o-type inclusive the 60^o segment belonging to the kink structure. It can be revealed from the pictures that for 30^o, 60^o and 90^o types dislocation lines the super kinks will decrease the *average dangling bond line density*. The only super kinks on screw-type dislocation line (Figure 17 (b)) will increase the average dangling bond density coming from zero up to a magnitude corresponding to that one of a 30^o-segment. As a consequence, dislocations having super kinks should show change in recombination activity.

It would be more convenient to come from quantity of average dangling bond density, characterising a single super kink to *total dangling bond density* describing density of dangling

bonds at longer dislocation segment. Depending on whether the super kinks formed will possess increased or decreased total dangling bond density, the recombination activity of the whole dislocation segment will be higher or lower, respectively.

From Figure 18, it can be deduced that each super kink contributes with two additional segments of length h/sin30° to the *total length* (sum of lengths of all type segments), thus total dangling bond line density may be changed.

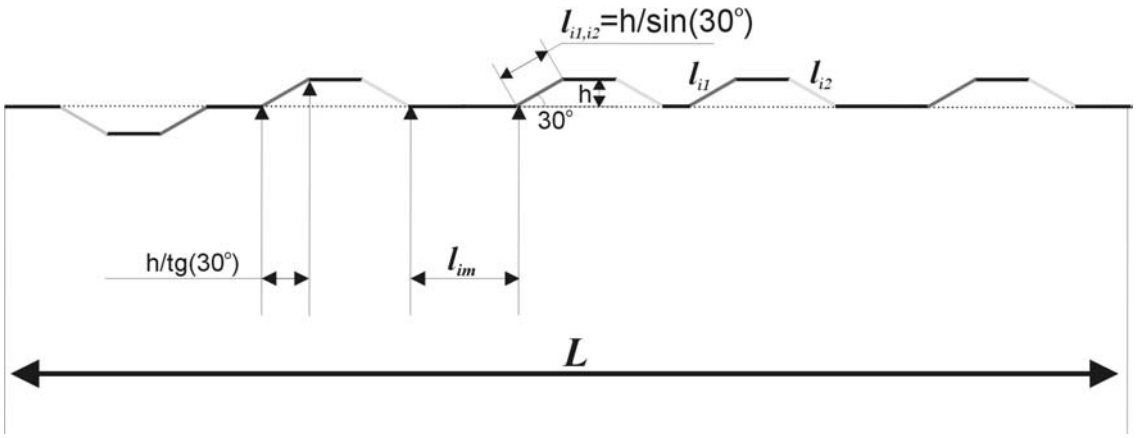

Figure 18. Change of specific effective length L of the dislocation by means of super kinks.

Formation of a double super kink excludes two part of length (h / tg30°) reducing the length of the main type straight dislocation line, which initially was equal to L. But, instead these two segments of main type, the other two parts of type 1 (left) and 2 (right) with length (h / sin30°) are formed and came into play.

Presence of super kinks of number n_K decreases effectively the initial length of the straight dislocation line of main type by:

$$\Delta L_m = L - \sum_i l_{im} = 2n_k (h/tg30^o) \tag{2}$$

However, due to presence of number $2n_K$ of additional segments with length of (h / sin30°) the total length is increased, and for the change of total length we have:

$$\Delta L_{tot} = 2n_k (h/sin30^o) - 2n_k (h/tg30^o) = \frac{2n_k h\left[1 - \cos 30^o\right]}{\sin 30^o} \tag{3}$$

Change of number of dangling bonds is caused by effectively variation of the total length and depends on dangling bond densities in each segment 1 and 2 of super kink formed. Thus, in asymmetric case of super kinks both contributions to total length from single super kink 1 and from 2 have to be separated because of different dangling bond densities.

In order to calculate the contribution of each type of super kink to total dangling bond number n_{tot}, the lengths of all segments as at kinks as at straight dislocation line have to be summed up and multiplied by corresponding magnitudes of dangling bond densities γ_i:

$$\begin{aligned} n_{tot} &= \gamma_m \sum_i l_{im} + \gamma_1 \sum_i l_{i1} + \gamma_2 \sum_i l_{i2} = \gamma_m [L - 2n_k (h/tg30^o)] + \gamma_1 n_k (h/sin30^o) + \gamma_2 n_k (h/sin30^o) = \\ &= \gamma_m L + \frac{n_k h\left[(\gamma_1 + \gamma_2) - 2\gamma_m \cos 30^o\right]}{\sin 30^o}; \end{aligned} \tag{4}$$

It is seen from this expression, that if n_k=0 we have: $n_{tot} = \gamma_m L \equiv n_{init}$.

Taking into account that super kink density is determined as number of super kinks per unit length $N_k = n_k/L$, and coming from quantities of dangling bond numbers to densities, defining the *total dangling bond density* as total number per unit length $\gamma_{tot} \equiv n_{tot}/L$, from eq. (4) we have:

$$\gamma_{tot} = \gamma_m + \frac{N_k h\left[(\gamma_1 + \gamma_2) - 2\gamma_m \cos 30^o\right]}{\sin 30^o} \tag{5}$$

Analysing the derived formula, it is seen, for instance, that if $N_k = 0$, than $\gamma_{tot} = \gamma_m$.

In case of $\gamma_1 = \gamma_2 = \gamma_m$ the total density increases. However, depending on magnitude of the net dangling bond density in segments of super kinks $(\gamma_1 + \gamma_2)$, some cases could be distinguished. So, from eq. (5) is seen that total dangling bond density can:

1) be constant if $(\gamma_1 + \gamma_2) = 2\gamma_m \cos 30^o$;

2) increase if $(\gamma_1 + \gamma_2) > 2\gamma_m \cos 30^o$;

3) decrease if $(\gamma_1 + \gamma_2) < 2\gamma_m \cos 30^o$;

Taking into account that $\sin 30^o = 1/2$ and $\cos 30^o = 0.866$, finally we get:

$$\gamma_{tot} = \gamma_m + 2N_k h\left[(\gamma_1 + \gamma_2) - 1.732\gamma_m\right] \tag{6}$$

It is seen that eq. (6) describes a linear dependence of dangling bond density on concentration of super kinks. The consequences of the eq. (6) is that total dangling bond density in the dislocation containing super kinks can as increase as decrease depending on the net dangling bond density $(\gamma_1 + \gamma_2)$.

Substituting the calculated data on dangling bond densities for super kinks constructed (Figure 17) into eq. (6), one comes to conclusion, that total dangling bond density should remain constant for 30^o, 60^o, and 90^o and increase for the screw dislocations.

3.3 Partial dislocations in the wurtzite lattice

3.3.1 Splitting of the basal perfect dislocations

Gliding perfect dislocations in the wurtzite structure are preferably to be split into partial dislocations for the energetic reasons. The partial dislocations move in a common glide-set plane belonging to a Shockley-type stacking fault. The energy balance of the two partials including stacking fault is negative, so that the dislocations are split following Frank's energy criteria. For instance, the perfect ***a***-type dislocation lying in the basal plane (0001) dissociates into the two partials with Burgers vectors $1/3[\bar{1}100]$ and $1/3[01\bar{1}0]$, respectively, according to:

$$\frac{1}{3}[\bar{1}2\bar{1}0]=\frac{1}{3}[\bar{1}100]+\frac{1}{3}[01\bar{1}0]$$

As it was mentioned earlier, for the perfect dislocations in glide-set planes the number of dangling bonds is higher than in shuffle-set configuration. One can suppose that the splitting of perfect dislocation will increase the dangling bond density.

Table 3-7.: Possible types of partial dislocations in basal slip plane of wurtzite lattice [osip70].

No.	Type of polar dislocation	Axis	Burgers vector	Notation
1	Frank	$<2\bar{1}\bar{1}0>$	$1/6<0\bar{2}23>$	F_1
2	Frank	$<1\bar{1}00>$	$1/6<2\bar{2}0\bar{3}>$	F_2
3	Shockley-30°	$<2\bar{1}\bar{1}0>$	$1/3<1\bar{1}00>$	Sh_{1B}
4	Shockley-90°	$<2\bar{1}\bar{1}0>$	$1/3<01\bar{1}0>$	Sh_{2B}
5	Shockley-0°	$<10\bar{1}0>$	$1/3<10\bar{1}0>$	Sh_{3B}
6	Shockley-60°	$<1\bar{1}00>$	$1/3<01\bar{1}0>$	Sh_{4B}
		$<1\bar{1}00>$	$1/3<0\bar{1}10>$	Sh_{4B}
7	Shockley	<0001>	$1/3<\bar{1}011>$	Sh_{1P2}
8	Shockley	$<0\bar{1}\bar{1}0>$	$1/3<\bar{1}011>$	Sh_{2P2}
9	Shockley-30°	$<2\bar{1}\bar{1}0>$	$1/3<1\bar{1}00>$	Sh_{5B}
10	Shockley-30°	$<2\bar{1}\bar{1}0>$	$1/3<1\bar{1}00>$	Sh_{6B}
11	Shockley-90°	$<2\bar{1}\bar{1}0>$	$1/3<01\bar{1}0>$	Sh_{7B}
12	Shockley-90°	$<2\bar{1}\bar{1}0>$	$1/3<01\bar{1}0>$	Sh_{8B}
13	Shockley-60°	$<1\bar{1}00>$	$1/3<01\bar{1}0>$	Sh_{9B}
14	Shockley-60°	$<1\bar{1}00>$	$1/3<01\bar{1}0>$	Sh_{10B}
15	Shockley-0°	$<10\bar{1}0>$	$1/3<01\bar{1}0>$	Sh_{11B}
16	Shockley-0°	$<10\bar{1}0>$	$1/3<01\bar{1}0>$	Sh_{12B}
17	Shockley-60°	$<1\bar{1}00>$	$1/3<01\bar{1}0>$	Sh_{13B}
18	Shockley-60°	$<1\bar{1}00>$	$1/3<01\bar{1}0>$	Sh_{14B}

A large variety of possible types of partial dislocations in the wurtzite structure has been reported in [osip70] (see Table 3-7). Reactions between the partial dislocations were also proposed (see Table 3-8). Same notations of the dislocation types as proposed by authors are used in this table. Abbreviations “Sh” and “F” denote Shockley and Frank dislocations, respectively. Subscript letters B and P note basal and prismatic dislocations, respectively.

In Table 3-7 only perfect dislocations contributing to the dislocation loop structure (Figure 9 (a)) are considered, i.e. screw, 90^o, 30^o and 60^o type dislocations. These perfect dislocations are split up according to the scheme given in Figure 19. From the Table 3-7, axes and Burgers vectors of these perfect dislocations have been taken and some general reactions are schematically drawn by vector diagrams in Figure 19.

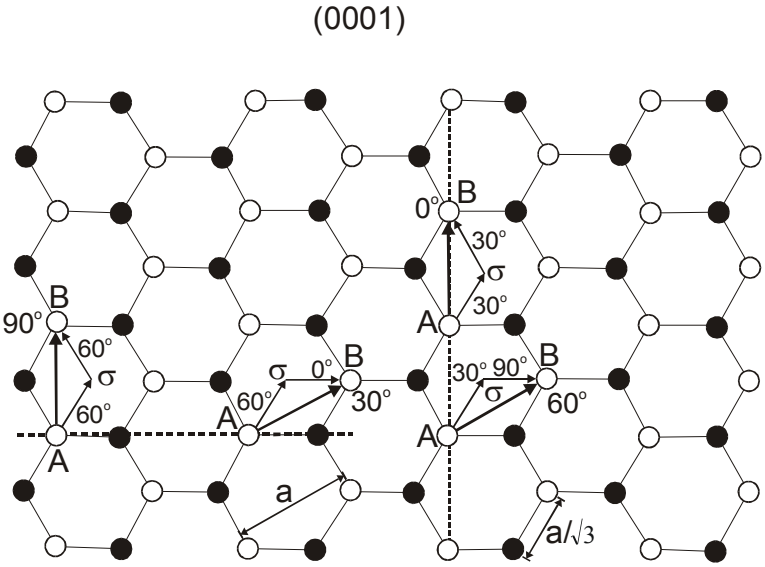

Figure 19. Scheme of splitting of basal perfect dislocations into partials for wurtzite lattice.

Practically, there are more types of reactions than shown in Figure 19 due to the facts that splitting can occur either above or below the plane of location of the perfect dislocation and the shear can be of **σB** or **Aσ** type. These reactions are written in the Table 3-8.

Table 3-8.: Possible general splitting reactions for basal perfect dislocations in the wurtzite lattice.

$0^o \rightarrow 30^o(\alpha) + 30^o(\beta)$
$90^o \rightarrow 60^o + 60^o$
$30^o \rightarrow 0^o + 60^o$
$30^o \rightarrow 60^o + 0^o + 0^o$
$60^o \rightarrow 90^o + 30^o$

As it could be seen from presented reactions, the splitting of a screw and edge are going on in one way only, whereas a 30^o perfect dislocation may split up in accordance to two types of reactions, and the 60^o does this in four different ways (Table 3-9).

A model of the basal loop structure constructed by means of partial dislocations is proposed as shown in Figure 20. Its slip plane is in the glide set configuration.

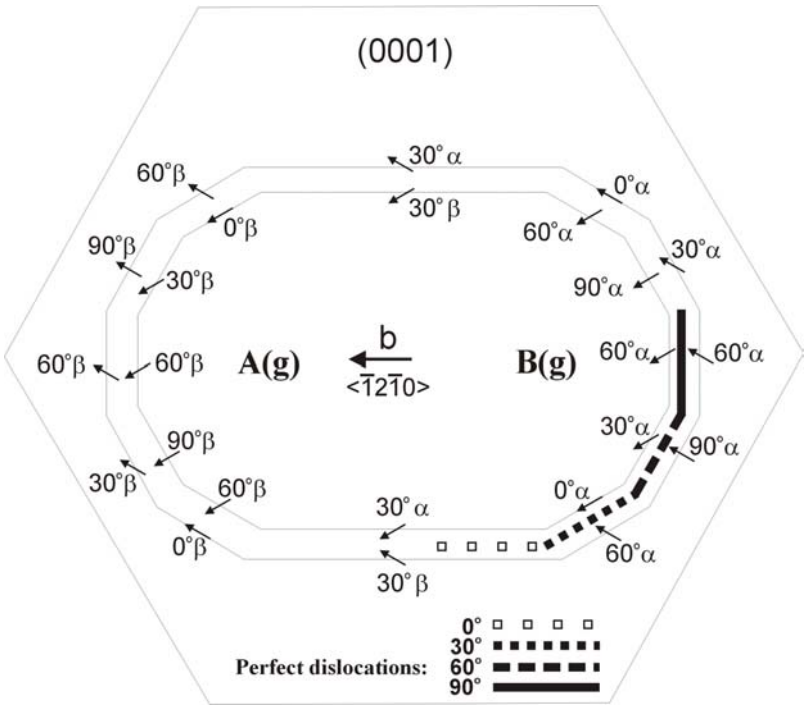

Figure 20. Model of splitting of basal dislocation loop structure for wurtzite lattice.

In order to determine the dangling bond line densities all types of partials of interest, one has to consider the corresponding core structures in more detail.

As shown in [osip70], the Sh_{1B} is a 30° Shockley dislocation. Its core consists of a homoatomic row with broken bonds and, therefore, can have A or B type edge atom.

The Sh_{2B} is a 90° partial dislocation. Its core consists of two parallel homoatomic rows with one broken bond per atom.

Sh_{3B} is a screw partial Shockley dislocation without dangling bonds.

For Sh_{5B} partial the core consists of two parallel homoatomic rows, each core atom has one broken bond in one row and two broken bonds per atom in another row.

In the Sh_{6B} partial the core consists of 3 parallel rows of atoms in two planes with one broken bond per atom. Two homoatomic rows lie in the upper double layer, and the row consisting of atoms of different types, lies in lower layer. By means of extra elastic displacement, one of the upper rows can be chemically closed up with the lower one, which decreases the number of broken bonds in the core.

Sh_{7B} is formed in result of splitting the 30° Sh_{1B} dislocation. It consists of a double row of atoms of different kinds with one dangling bond per atom.

For Sh_{8B} the core consists of parallel rows of atoms of one kind, each atom has one broken bond per atom. It is formed in result of splitting the 30° Sh_{1B} dislocation.

Sh_{9B} is a 60° Shockley dislocation terminating a stacking fault formed during splitting a perfect 30° dislocation. The core has on average 0.5 dangling bond of one kind atom per lattice constant length.

Sh_{10B} is a 60° partial dislocation with 0.5 dangling bond of one kind atom per lattice constant length.

The dislocations Sh_{11B} and Sh_{12B} are no longer screw-type dislocations in the usual sense, because they show broken bonds.

The dislocations 60^o Sh_{13B} and 60^o Sh_{14B} are two partial dislocations having great number of broken bonds. The atomic configurations in these cores are rather complex.

Analysing the core structure models proposed by Osipyan [osip70] for the partial dislocations in more details, data concerning atom types responsible for the dangling bonds and these line densities could be obtained. The results of calculations of dangling bonds per lattice constant for the various partial dislocations under consideration are given in Table 3-9.

Table 3-9.: Separated numbers of A- and B- type atoms per period length *l* for partial dislocations. Values of total line dangling bond densities of partial dislocations and splitting reactions for perfect basal dislocations.

#	Possible reaction of dislocations	Number of A(g)/B(g) type atoms per unit period at dislocation line, n		Period length *l*,a	Dangling bond density, $\gamma = n_{DB}/l$
		B(g)-core	A(g)-core		
1	$0^o \rightarrow 30^o(\alpha)\ Sh_{1B} + 30^o(\beta)\ Sh_{1B}$	**2** (1_A, 1_B)	**2** (1_B, 1_A)	1	**2/a**
2	$30^o \rightarrow 0^o\ Sh_{3B} + 60^o\ Sh_{9B}$	**0.5**$_B$	**0.5**$_A$	$1/\sqrt{3}=1.732$	**0.29/a**
3	$30^o \rightarrow 60^o\ Sh_{10B} + 0^o Sh_{11B} + +0^o Sh_{12B}$	**6.5** (1.5_A, 5_B)	**6.5** (1.5_B, 5_A)	$1/\sqrt{3}=1.732$	**3.75/a**
4*	$30^o \rightarrow 60^o\ Sh_{10B} + 0^o Sh_{11B} + +0^o Sh_{12B}$	**2.5** (1.5_A, 1_B)	**2.5** (1.5_B, 1_A)	$1/\sqrt{3}=1.732$	1.443/a
5	$60^o \rightarrow 90^o\ Sh_{2B} + 30^o\ Sh_{5B}$	**5** (2_A, 3_B)	**5** (2_B, 3_A)	1	**5/a**
6*	$60^o \rightarrow 90^o\ Sh_{2B} + 30^o\ Sh_{5B}$	**3** (2_A, 1_B)	**3** (2_B, 1_A)	1	**3/a**
7	$60^o \rightarrow 90^o\ Sh_{2B} + 30^o\ Sh_{6B}$	**5** (2_A, 3_B)	**5** (2_B, 3_A)	1	5/a
8*	$60^o \rightarrow 90^o\ Sh_{2B} + 30^o\ Sh_{6B}$	**3** (1_A, 2_B)	**3** (1_B, 2_A)	1	3/a
9	$60^o \rightarrow 90^o\ Sh_{7B} + 30^o\ Sh_{1B}$	**3** (1_A, 2_B)	**3** (1_B, 2_A)	1	3/a
10	$60^o \rightarrow 90^o\ Sh_{8B} + 30^o\ Sh_{1B}$	**3** (1_A, 2_B)	**3** (1_B, 2_A)	1	3/a
11	$90^o \rightarrow 60^o\ Sh_{13B} + 60^o\ Sh_{14B}$	**5.5** (2_A, 3.5_B)	**5.5** (2_B, 3.5_A)	$1\sqrt{3}=1.732$	**3.176/a**
12*	$90^o \rightarrow 60^o\ Sh_{13B} + 60^o\ Sh_{14B}$	**4.5** (2.5_A, 2_B)	**4.5** (2.5_B, 2_A)	$1\sqrt{3}=1.732$	**2.6/a**
* The number of dangling bonds is reduced due to reconstruction of core structure.					

The results of the dangling bond densities calculations presented in Table 3-9 are plotted in Figure 21. Here the only highest and lowest values for each partial have been plotted. It should be noted, that only the total numbers of dangling bonds at partials were taken into account, and no difference in the properties of bonds for A- or B-atom types was considered.

It is seen from the diagram (Figure 21), that both the maximum and minimum magnitude of dangling bond densities are for the 60^o–partial dislocation. The minimum value can appear either for the 30^o- or for the screw-type partial depending on dislocation core conditions. If dangling bond reconstruction is realised then the 30^o-type partial dislocation has lowest dangling bond density.

The distribution of the total dangling bond density over the loop structure of a basal glide dislocation is sketched in Figure 22. The density picture of the loop structure earlier introduced in Figure 16 (b) has to be modified as shown in Figure 22.

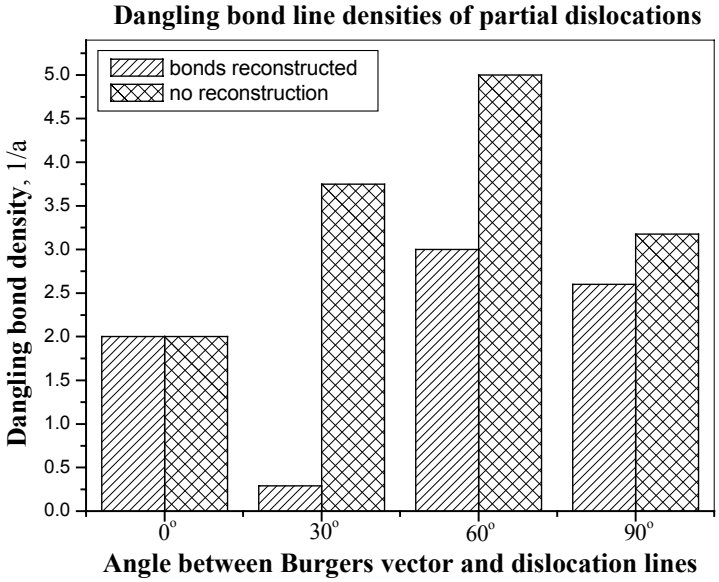

Figure 21. Relation of as calculated dangling bond densities to dislocation type given by angle between Burgers vector and dislocation line for basal partial dislocations in wurtzite lattice. The case of minimal dangling bond density is realized when bonds are reconstructed.

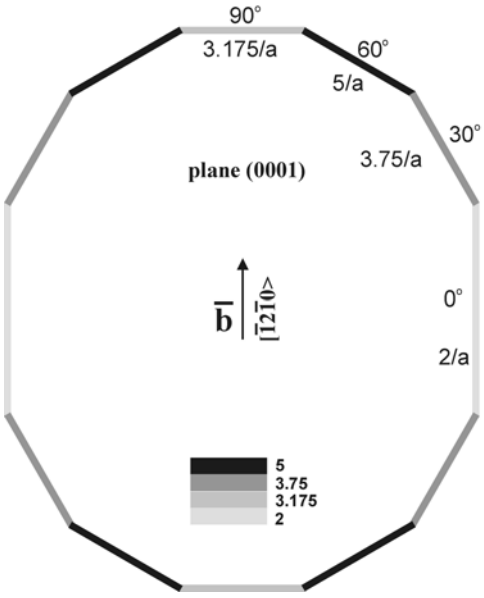

Figure 22. Distribution of total dangling bond density given in Table 3-9along dislocation loop structure for dissociated dislocation configuration.

Now, passing along the line of the loop structure shown in Figure 22 from left-hand side screw-segment toward the right-hand side screw part, one could note that the edge segment is neighboured by two 60°-dislocations of higher dangling bond density that differs from the model presented in Figure 16 (b).

The basal partial dislocations have the polar character (Figure 20), but the results of dangling bond calculations presented in Table 3-9 did not make any distinction between the types of atoms responsible for the dangling bonds.

3.4 Structure of fundamental kinks

For understanding dynamic behaviour of dislocations a complicated picture of dislocation motion via formation, migration and reactions of kinks must be developed. In case of strong dislocation lattice coupling as characterized by high Peierls potential, dislocations are known to move by forming elementary double kinks (kink pairs), which spread laterally along the dislocation line. The formation of kink pairs results in specific local core structure site as illustrated in Figure 23 (a, b). The pictures show a top view of the (111) glide plane with core structures of kinked 90^o partial dislocation line segment in ZB/Diamond lattice. The graphics display a left (LK) and right (RK) single kink part of a double kink pair. The kink region shows a specific arrangement of the core atoms, which is seen to be different in the LK and RK parts (Figure 23 (b)). Such kink asymmetry can arise from distinct lattice symmetry and mixed character of the dislocations under consideration. Furthermore, the kink structure is affected by an atomic reconstruction of the entire dislocation core. It has been proposed [stil82, bul95, big92] that dislocation cores reconstruct in order to eliminate dangling bonds. Thus, each under-coordinated core atom forms a new bond with an adequate partner in the core region. Several authors have shown theoretically [han95, ari94, huan95] that this reconstruction lowers the energy of core structure. Moreover, EPR measurements prove a low density of dangling bonds, suggesting full reconstruction. Thus, a consensus seems to have emerged that this reconstruction represents the physically correct core structure under equilibrium conditions, and a large volume of work has come to rely on this assumption [got93, no91].

The dislocation core structure given in Figure 23 (b) illustrates the change of atomic arrangement due to reconstruction. Remaining kink asymmetry and full eliminating of dangling bonds except of one atom in the kink area can be recognised. Moreover, a combination of possible reconstruction defects appearing along the dislocation line leads to particular complexes of kinks with such defect, that originate in doubling of numbers of dangling bonds.

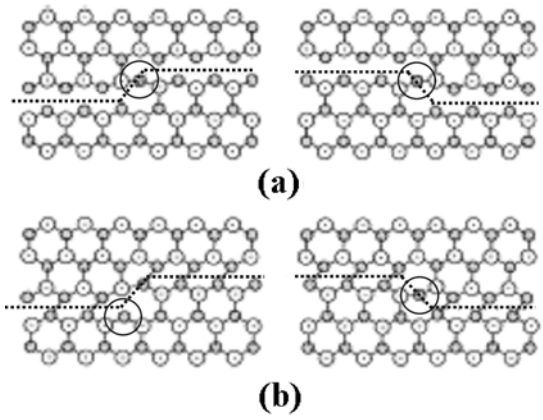

Figure 23. Kinks in a 90^o partial e.g. in Si with atoms above and below the (111) glide plane, shown as open and closed circles, respectively for, (a) LK and RK kink parts in unreconstructed core, (b) LK and RK kink parts after reconstruction which breaks the mirror symmetry [bul97].

A more detailed insight in other possible core structure configurations reveals additional kinds of kink structures containing completely reconstructed dangling bonds. It is predicted in [jon80] that fully reconstructed kinks would be strongly favoured energetically.

Due to the remaining unreconstructed dangling bonds the fundamental kinks appear to be possible candidates as electrically active sites at a dislocation line exhibiting otherwise a reconstructed core structure.

3.4.1 Factors influencing density of fundamental kinks

Temperature

A dislocation exists at low temperature in mechanical equilibrium as a straight line lying parallel to its Peierls valley. At finite temperature there should be a certain amount randomly distributed fundamental kinks originating from thermal activation of double kink pairs.

In the case of low external stress the kink density at the straight dislocation line located in the Paierls valley remains about the same as under mechanical equilibrium. The concentration of the thermal double kinks depends on the formation energy E^*_{DK} for kink pairs and the temperature T [hir82], and is given as:

$$N_{DK} = \frac{2}{a}\exp\left(-\frac{E^*_{DK}}{kT}\right) = N^+_{DK} + N^-_{DK} \tag{7}$$

where $N^+_{DK} + N^-_{DK} = N_{DK}$ denotes the sum of positive and negative kinks concentrations respectively, "a" is the period of the Peierls potential of second kind, N_{DK} represents the total kink pair density that comprises both the parts of positive N^+_{DK} as well as that of the negative kink pair N^-_{DK}. If there is no force acting on the dislocation line, the concentration of positive and negative kink pairs balance. It can be seen, that the given relation possesses saturation when the temperature rises, and kink pair concentration aspires to maximum value 2/a.

All these kinks have small drift velocity, at that, positive and negative kinks move in opposite directions.

Dislocation velocity

The dislocations start to move when the concentration of positive kink pairs N^+_{DK} exceeds the concentration of the negative ones N^-_{DK}. The net density of kink pairs per unit length of line is given as:

$$N_K = \left|N^+_{DK} - N^-_{DK}\right| \tag{8}$$

The dislocation velocity normal to the defect line will be expressed as:

$$V = N_k \cdot v_k \cdot h \tag{9}$$

Thus, for the kink concentration we have:

$$N_k = \frac{V}{h v_k} \tag{10}$$

This simple formula shows that kink concentration has to decrease as the kink velocity v_K rises.

On the other hand, the dislocation glide velocity is proportional to single kink migration speed v_K obtained from the Peierls mechanism at low stresses and high temperatures as [hir82]:

$$v_k \approx \frac{\nu_D b^3 \sigma h}{kT} \tag{11}$$

where ν_D is Debye frequency, σ is stress, b – Burgers vector length and h is distance between two neighbour Peierls valleys. Here also assumed that a≈b.

From (10) and (11) follows:

$$N_k \approx \frac{v}{\nu_D b^3 h^2} \cdot \frac{kT}{\sigma}, \tag{12}$$

i.e. the kink concentration can be governed by the stress applied as well as by the temperature.

Under conditions of constant stress and temperature there is a direct proportionality of kink concentration to dislocation velocity.

Geometry of dislocation line

Beside of the kink pairs produced by thermal fluctuations, whose density is governed by temperature, there exist another kind of kinks, which are formed for geometrical reasons.

Gottschalk [got83a] has shown, for instance, if there are two interconnected dislocation segments laying along two different Peierls valleys then a transition from one crystallographic direction to the other one is realized by a smoothed bend but not by a sharp corner because of an effect of line tension [see section 3.5.5]. The bend is made up of elementary kinks. The static dislocation bend with radius R of curvature and a 60^o angle is sketched in Figure 24 (a). To get a bend between the two straight dislocation segments, a certain quantity of kinks with distinct distribution is required. Supposing that the bend segment A_1A is formed of single kinks belonging to segment 1 and A_2A results from single kinks belonging to segment 2, a simple geometrical consideration yields the total number n of single kinks contained in within the bend:

$$n = 2 \cdot (1\text{-}\cos 30^o) \cdot \left(\frac{R}{h}\right) = 0.27 \cdot \left(\frac{R}{h}\right) \tag{13}$$

Here h is the distance between two parallel Peierls valleys. For example, if for Si h=0.33nm and R=100 nm, then we obtain n=82.

The local distance y of the single kinks depends only on the angle between the “average” dislocation line and the <110> direction:

$$y = \frac{h}{\sin\beta_i}, \quad i=1,2 \tag{14}$$

and thus the local kink density:

$$\bar{n} = \frac{1}{y} = \frac{\sin\beta_i}{h} \tag{15}$$

These values both are independent of R. If $\beta_{imax} = 30^o$,

$$y_{min} = 2h; \quad \bar{n}_{max} = \frac{1}{2h} \tag{16}$$

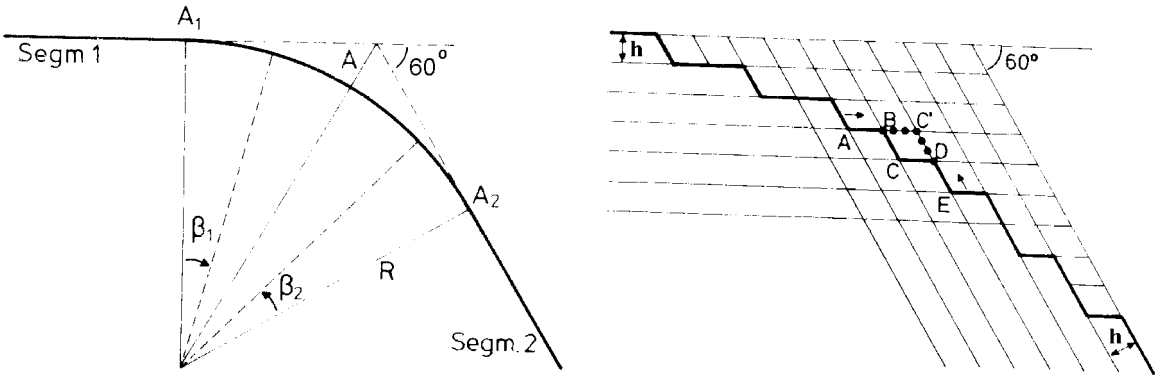

(a) (b)

Figure 24. (a) 60^o- dislocation bend. (b) Kink annihilation in a forward moving bend [got83].

The kinks present in the segment A_1A are all elementary kinks with same sign. In [hir82], Hirth and Lothe have shown that there exists a mutual repulsive force between the kinks of same sign and that the force exerted by the line tension of a bent dislocation segment can be derived from this kink-kink interaction.

Considering the apex of a bend one can notice (Figure 24 (b)) that it is by no means possible to reduce the distance of neighbouring kinks below the minimal length 2h because of crystallographic reasons. It can be seen, too, that the two sorts of kinks, e.g. BC (or ABCD) on segment 1 and CD (or BCDE) on dislocation 2 cannot be distinguished in this region.

Finally, we can note that the number of "geometrical kinks" in bent area is fixed, while kink concentration at the straight-line segments depends on temperature if stress is constant. The ratio of the thermal kink concentration to that one of at a bend depends on temperature. If the temperature is high enough, the concentration of thermal kink approaches maximal value 1/h, and the ratio of the concentrations of thermal and geometrical kinks becomes higher. On the other hand, at low temperatures, when concentration of thermal kinks is decreased, the concentration of geometrical kinks remains constant.

3.5 Dynamical dislocation properties

3.5.1 Empirical expression for dislocation velocity

As follows from experiments, the velocity of a dislocation depends on stress, temperature and presence of internal obstacles hindering dislocation slip motion. From numerous experimental measurements the dislocation motion is found to be a thermally activated process with velocity [cha62]:

$$v \sim \exp(-Q/kT) \tag{17}$$

where T-temperature, Q-activation energy. One should note that the activation energy changes distinctly below a certain critical shear stress σ_k, where the activation energy is a decreasing function [ale86, geo79].

At a fixed temperature, the dislocation velocity increases with raise of shear stress in a wide range:

$$v \sim (\sigma/\sigma_0)^m \tag{18}$$

Here, σ is the applied shear stress, σ_o is a constant having dimension of stress, and *m* is a stress exponent typically ranging between 1 and 2 for glide processes.

Thus, based on eq. (17) and eq. (18) the dislocation glide velocity may be described in the stress range above σ_k by an empirical relation given as:

$$v(\sigma,T) = v_0(\sigma/\sigma_0)^m \exp(-Q/kT) \tag{19}$$

Here, v_o is a material dependant constant with dimension of velocity, Q is mostly considered in the stress range $\sigma > \sigma_k$. This activation energy Q differs from crystal to crystal depending on type of conductivity and type of dislocation studied in various materials.

The stress exponent m is found to be slightly temperature dependant and splits up into two terms, one depending on temperature and type of dislocation and the other one only depends on geometrical dislocation parameters like line direction and type of glide system i.e.:

$$m = E_i / kT + m_0 \tag{20}$$

For instance, E_i is different for screw and 60° dislocations, $m_0 \leq 0$. Also, the stress exponent *m* is a varying function of stress. In some cases there is a threshold stress, called the starting stress, for the dislocation motion. Consequently, the eq. (19) is only an approximate expression of the dislocation velocity for a narrow stress range.

Combining equations (19) and (20) we have for the activation energy from eq. (17):

$$Q = Q_0 - E_i \ln(\sigma / \sigma_0) \tag{21}$$

that confirms a particular stress dependence of activation energy Q within the stress range $\sigma > \sigma_k$.

3.5.2 Peierls mechanism of dislocation motion

As it can be seen from a lot of electron microscopy pictures, isolated dislocations segments occur as straight lines, which are oriented along certain crystallographic directions in their glide planes. This can be explained by the existence of pronounced potential valleys, the Peierls potentials of 1st kind [pei40], which lie parallel to distinct lattice rows.

Gliding of a dislocation line corresponds to the motion of the dislocation from one Peierls valley into the next one overcoming the potential barrier. The potential valleys are situated in the most close packed planes and point exactly along the close-packed atomic rows assigning the minima of potential energy.

Peierls potential and Peierls stress

If dislocations move in a potential relief, which is described by a periodical function, interatomic distances in the crystal determine the period of this function (Figure 25).

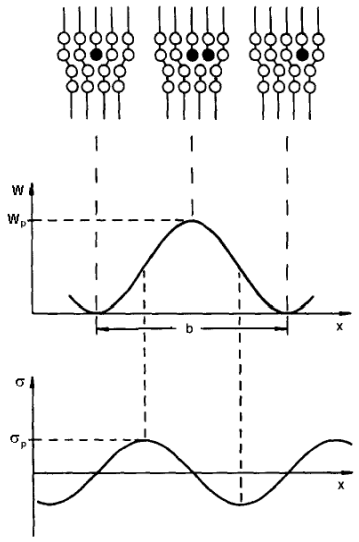

Figure 25. Sketch illustrating the definition of the Peierls potential W_p and σ_p the Peierls stress. The σ_p is given by the negative gradient of the periodical potential and is the stress which a dislocation requires to overcome the Peierls potential in order to glide on a slip plane. In materials with relatively large σ_p, e.g., in Ge $\sigma_p \approx G*10^{-2}$, dislocation can move at $\sigma << \sigma_p$ by thermally activated formation of kink pairs, which can then propagate sideward.

Cottrell and Nabarro have calculated the displacement energy of this periodical potential [cot53]:]

$$W(\alpha)=\frac{Gb^2}{4\pi(1-\nu)}+\frac{Gb^2}{2\pi(1-\nu)}\exp\left(-\frac{2\pi d}{(1-\nu)b}\right)\cos(4\pi\alpha)= \\ =\frac{Gb^2}{4\pi(1-\nu)}+\frac{1}{2}W_p\cos(4\pi\alpha) \tag{22}$$

Where G - shear modulus, ν - Poisson ratio, d – glide plane spacing, b - Burgers vector length, α=x/b displacement and W_p is called "Peierls potential". The stress required to overcome the Peierls potential is called *Peierls stress* and denotes the stress that a dislocation needs to glide on its slip plane.

Peierls stress σ_p is given by negative gradient of the periodical potential:

$$\sigma_p=\frac{1}{|b^2|}\left[\frac{\partial W(\alpha)}{\partial\alpha}\right]_{max}=\frac{2\pi W_p}{|b^2|}=\frac{2G}{(1-\nu)}\exp\left(-\frac{2\pi}{(1-\nu)}\frac{d}{|b|}\right) \tag{23}$$

Peierls stress separates the modes of viscous ($\sigma>\sigma_p$) and thermo-activated ($\sigma\le\sigma_p$) dislocation motion, therefore σ_p is the critical shear stress mentioned above.

It is established [hir82], that for a given kind of crystal, σ_p has to decrease as the temperature raise, and σ_p has to be lower for edge-type dislocations compared to the value for screw ones.

The motion of a dislocation as a whole is known, however, to be energetically not favourable. Instead of this, the dislocation motion occurs by means of kink pairs [kol96, spe97, lun99, joo97]. This way, a dislocation can easier reach the next valley. The moving kinks have also to move over a potential relief – the 2nd kind Peierls potential. To perform an elementary step of the dislocation movement, the kink pair called double kink (DK) has to be generated (Figure 26) as smallest pair of left kink (LK) and right kink (RK) while expands and disappears by LK-RK kink annihilation or by propagation along the Peierls valley [hir82] up to the ends of dislocation.

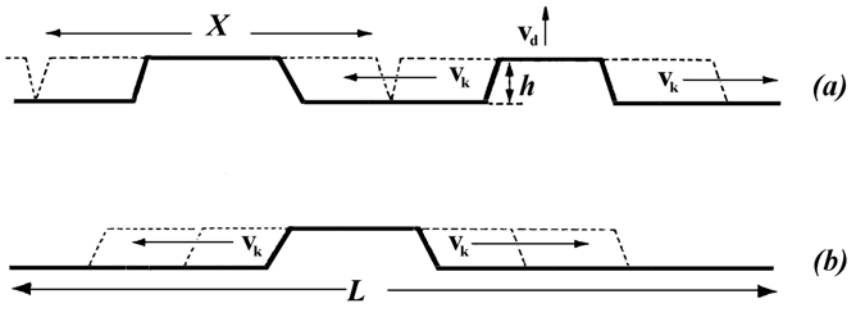

Figure 26. Nucleation of kink pairs and subsequent single kink migration in the kink-collision regime (a) and in collision free regime kink propagation (b).

Thus, the elementary process of this Peierls mechanism includes kink pair formation, kink diffusion/drift and single kink annihilation or escape of kinks. Nucleation of kink pairs is a thermally activated process. There is a critical minimum width X^* (Figure 27) of DK affected by thermal fluctuations. The DK with critical width is able to spread along the dislocation line due to acting stress σ, because it is energetically more favourable to have DK spreading than converging.

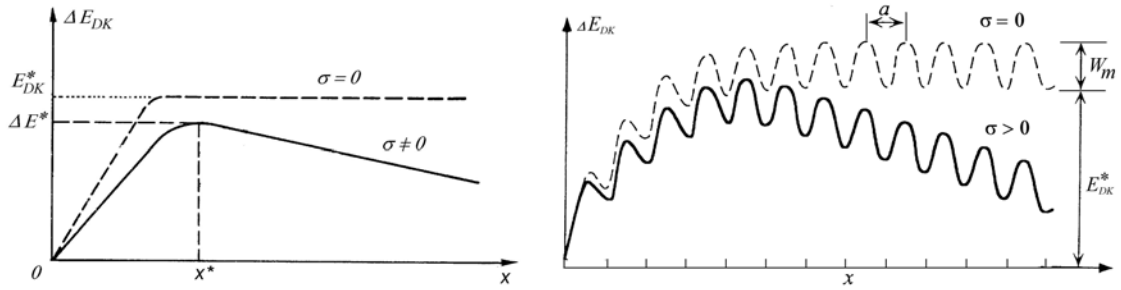

(a) (b)

Figure 27. The potential energy of a DK as a function of kink pair width X separation [hir82] in the kink diffusion model (a) and in the Peierls model (b) illustrating 2nd kind potential.

The whole expression for kink pair energy $E_{DK}(X)$ includes the terms of kink interaction in the pair and of work done by the applied stress [hir82]:

$$E_{DK}(x) = E^*_{DK} - \frac{Gb^2h^2}{8\pi X} - \sigma bhx \tag{24}$$

The formation energy of the critical double kink E^*_{DK} is slightly dependent on stress σ according to [krou61]:

$$E^*_{DK}(\sigma) = E_{0DK} - a'\sigma^{1/2} \tag{25}$$

where E_{0DK} is the self-energy of the double kink, a`- proportionality factor.

Steady velocity of a dislocation segment is simply given by the product of the kink line density N_k, the kink's diffusion velocity v_k and distance *h* between the valleys of the 1st order Peierls potential, as given above in eq. (9).

The line density N_k is obtained from the temperature-dependent nucleation rate:

$$J = J_0 \exp(-E^*_{DK} / kT) \tag{26}$$

and the kink pair lifetime X/v_k:

$$N_k = JX/v_k \tag{27}$$

where X is the mean free path of the kinks. Therefore,

$$V = J \cdot X \cdot h \tag{28}$$

There are two processes terminating kink motion:

1) The kink can reach an impassable obstacle on the dislocation line, such as the end of the segment.
2) The kink annihilates with another kink of opposite sign due to collision.

Let's assume that L is the distance between obstacles. Then the free mean path X of a DK is:

$$1 / X = 1 / L + N_k / 2 \tag{29}$$

Now two extreme cases can be considered:

1) If the kink line density is low ($N_k << 1/L$), than most of the kinks will reach the ends of the segment, and
2) Most of kinks annihilate ($X \rightarrow 2/N_k$) because they collision. Here the kink nucleation rate J equal to the collision rate $v_k N^2_k$, that results in ($X << L$):

$$X = 2\sqrt{v_k/J} \tag{30}$$

Finally, for the dislocation velocity in this we have:

$$V = 2h\sqrt{v_k J} = 2h\sqrt{v_k J_0}\exp(-E^*_{DK}/2kT) \tag{31}$$

It is very likely that under most experimental conditions used the case 2 is verified and intrinsic kink dynamics plays most important role. In order to get the kinks diffusing, they have to overcome the energy barrier W_m (2^{nd} order Peierls potential) that is higher then kT. Applying Einstein's relation, the kink velocity is found to be:

$$v_k = \frac{\sigma bh}{kT} a^2 \nu_D \exp\left(-\frac{W_m}{kT}\right) \tag{32}$$

where the ν_D denotes Debye frequency and a is the distance between two valley of the 2^{nd} order Peierls potential.

As shown in [hir82], the DK nucleation rate J is proportional to the kink velocity v_k:

$$J = \frac{v_k}{b^2}\exp\left(-\frac{E^*_{DK}}{kT}\right) \tag{33}$$

Therefore, we have:

$$V = 2h\sqrt{v_k J} = 2\frac{\sigma bh^2}{kT}\frac{a^2}{b}\nu_D \exp\left(-\frac{E^*_{DK}/2+W_m}{kT}\right) \tag{34}$$

From the eq. (34) and eq. (19) for the activation energy Q we can obtain the following expression:

$$Q = E^*_{DK}/2+W_m \tag{35}$$

Combination of the eq. (30) and eq. (33) yields:

$$X = 2 \cdot b \cdot \exp(E^*_{DK}/2kT) \tag{36}$$

The maximum of the 2^{nd} order Peierls potential for kink migration according to [geo87] is obtained as kink migration energy:

$$W_m = kT \cdot \ln\left(\nu_D \frac{2hba^2}{kT}\right)/v_K \tag{37}$$

3.5.3 Fundamentals of REDG effect

Electronic excitation of semiconductor crystals containing glide dislocations may often lead to the effect of so-called **R**ecombination **E**nhanced **D**islocation **G**lide (REDG). The REDG phenomenon is a softening effect and means increase of the dislocation glide velocity in the sample under electron beam excitation in comparison with the velocity in "darkness". This phenomenon is essentially due to a modification of the Peierls mechanism and is of intrinsic nature.

The enhanced dislocation velocity is described by two terms: the term of thermally activated dislocation glide (v_d) and an additional REDG-term (v_i), thus:

$$v = v_d + v_i \tag{38}$$

The temperature dependence of the enhanced velocity is quite characteristic. Both parts of the velocity expressions obey an Arrhenius low:

$$v_d = v_{0d} \exp(-E_d/kT) \quad \text{and} \quad v_i = v_{0i} \exp(-E_i/kT) \tag{39}$$

where E_d and E_i are the activation energies in darkness and under irradiation. E_i is independent of excitation and smaller then E_d, so $E_i = E_d - \Delta E$.

The velocity enhancement is brought about by the substantial reduction ΔE of the apparent activation energy. However, since the pre-exponential factor is simultaneously reduced by irradiation, the effect can be observed only at temperatures below a critical temperature T_c when $v_i >> v_d$.

The dislocation velocity increases with e-beam current density I as:

$$\Delta v \sim I^{\chi}, \tag{40}$$

where the exponent χ is about unity with a small variation depending on the dislocation systems.

Increase of irradiation intensity does not affect the slope of the velocity vs. temperature relation in the enhanced state; in other words, irradiation reduces the activation energy of dislocation glide by an amount independent of the irradiation intensity.

All of these facts are summarized by an empirical formula for the dislocation velocity as a function of temperature T, stress σ and irradiation intensity I:

$$v(T,\sigma,I) = v_{0d}(\sigma) \cdot \exp\left[\frac{-E_d}{kT}\right] + \xi_i \cdot v_{0i}(\sigma) \cdot R \cdot \exp\left[\frac{-(E_d - \Delta E)}{kT}\right] \tag{41}$$

Here R – rate of defect bound recombination under e-beam excitation (I); ξ_i - REDG coefficient; T – temperature; σ - shear stress on dislocation. Figure 28 illustrates the phenomenon of electron beam-induced enhancement of the slip velocity of dislocations in GaAs.

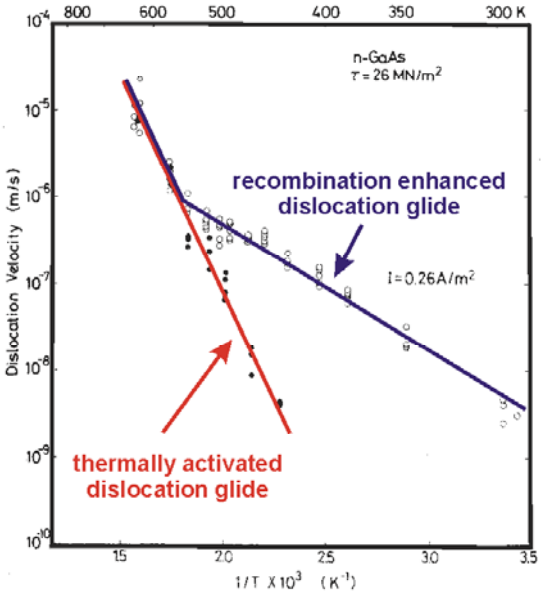

Figure 28. Temperature dependences of dislocation velocity for three types of dislocations in n-GaAs in the dark and under electron beam irradiation [mae83].

The first term dominates at high temperatures and at low temperatures the second term is relevant for the enhanced glide movement.

The critical temperature T_c is given by equating the first and the second term and is expressed by:

$$T_c = \left(\frac{\Delta E}{k} \right) / \ln \left(\frac{\mathrm{v_t}}{\mathrm{v_e}} \left[\frac{I_0}{I} \right]^{\chi} \right) \tag{42}$$

The magnitude of ΔE is independent of intensity I and stress σ, and does not exceed E_D. The magnitudes of E_D and ΔE are both dependent on the material and the dislocation type. The ΔE is in all cases smaller than the band gap energy E_g.

Physical origin of REDG effect is still an open issue. Heating of lattice could be most trivial cause of the enhancement, since, one may suspect a heating of lattice by the electron irradiation. However, the effect of lattice heating by irradiation is concluded to be negligible [mae83, mae81, mae83b]. Also charge state effect or doping effect [pat66, cho77] doesn't explain the REDG. In GaAs, the mobility of the α-dislocation is known to be insensitive to doping while that of β-dislocation is very sensitive [cho77]. If the role of the electron irradiation is to change the quasi-Fermi level, the resultant effect should be less pronounced in the α-dislocation than in β-dislocation, which is contradictory with experiments. Furthermore, while the doping effect manifests itself with a change in activation energy of dislocation velocity, the activation energy in REDG does not depend on the irradiation intensity that would change the quasi-Fermi level as the doping does. Thus, the charge state effect is unlikely to be the cause of the enhancement effect.

3.5.4 Recombination stimulated Peierls mechanism

During electron beam irradiation the electrons and holes are generated and travel through the crystal lattice until they are either recombined with each other or another trapping centers such as dislocations acting as very efficient recombination sites. After a pair of carriers is captured by the center, the system relaxes to stable ground state by releasing energy, which may be transformed to lattice vibrations (non-radiative electron-hole pair recombination), that results in the emission of a large number of phonons giving rise to phonon-kick mechanism [mae96].

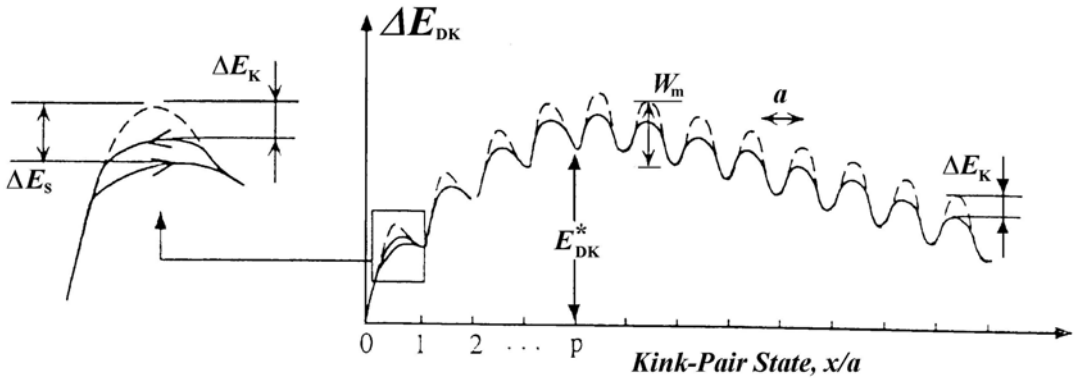

Figure 29. The potential barrier profile in the course of DK nucleation that proceeds by formation of a SDK (state 0→1) and kink for migration over the saddle-point state p.

The phonon-kick mechanism is likely to operate in defect processes in which only a small number of atoms are involved [mae96]. Although dislocation glide requires a collective motion of a large number of atoms, the fundamental processes as the formation of a smallest double kink and

the kink migration, proceed by rearrangement of a small number of atoms. The centers providing a nonradiative path for carrier recombination can be:

1. Kinks, which possibly introduce electronic energy levels in the band gap [hirs81, jon80]. If it is the case, the carrier recombination at the kink can stimulate the kink migration.
2. There must be a site on a straight dislocation where non-radiative recombination can take place for enhancement of DK formation [mae96].

Since the atomic structure of such a straight dislocation site will be different from that of the kink, the energy levels associated with them will be also different. This requires differentiating the magnitude of the phonon-kick energy and the barrier height for carrier capture for kink migration from those for DK formation.

This explanation of recombination enhanced Peierls mechanism is illustrated in Figure 29. Here ΔE_k and ΔE_s denote the net reduction of activation energy in possibly enhanced kink migration and possibly enhanced DK formation, respectively. The index $\boldsymbol{i}$=0 indicates the state before a DK is formed, and other states $\boldsymbol{i}$=1,2,… are those at which kinks can make diffusive jump to the neighboring states over the 2nd kind Peierls potential. The state $\boldsymbol{i}$=p indicates the saddle point configuration. One has to note that the energy reduction is different between DK formation (0→1) and its reverse process (1→0) that is needed for backward migration of kink.

To reveal which process is responsible for the REDG effect, the enhanced dislocation glide process has to be decomposed into its elemental steps within the framework of Peierls mechanism. This way, the expression for kink velocity v_k has to be rewritten as:

$$v_k = \nu_k \frac{\sigma b h a^2}{kT} \exp\left(-\frac{W_m}{kT}\right) \tag{43}$$

Here instead ν_D is used ν_k because the latter may depend on the recombination rate.

The kink-pair nucleating rate $\boldsymbol{J}$ is derived from a set of rate questions which describe the forward and backward jumps over the respective barriers shown in Figure 29 with E_i^+ and E_{i+1}^- denoting respectively, the barrier height for the forward jump from the state $\boldsymbol{i}$ to the state (i+1) and for the backward jump from state (i+1) to the state $\boldsymbol{i}$, $\boldsymbol{J}$ is written in form:

$$J = \nu_s \frac{\sigma b h}{kT} \exp\left[-\frac{1}{kT}\left\{\sum_{i=0}^{p-1}\left(E_i^+ - E_{i+1}^-\right)\right\}\right], \tag{44}$$

where again instead ν_D is used ν_s to express its possible dependence on recombination rate. Substituting eq. (43) and eq. (44) into eq. (31) and (V=J·L·h) we obtain the generalized formulae for dislocation velocity:

$$V = \sqrt{\nu_s \nu_k}\, \frac{2\sigma b h^2 a}{kT} \exp\left[-\frac{1}{kT}\left\{\frac{1}{2}\sum_{i=0}^{p-1}\left(E_i^+ - E_{i+1}^-\right) + W_m\right\}\right] \quad \text{for } L \gg X^* \tag{45}$$

In darkness, since $\sum\left(E_i^+ - E_{i+1}^-\right) = E_{DK}^*$ and $\nu_s \approx \nu_k \approx \nu_D$ (the Debye frequency), we get the same formulae as those derived by Hirth and Lothe [hir82].

For the REDG effect, one has to analyze separately the respective cases differing in the processes that are enhanced.

Case (i). Both the double kink formation and the kink migration are enhanced, that means a recombination occurs on both straight (s) dislocation sites and kink (k) sites. In this case, the frequency factors ν_s and ν_k are related to the recombination rate R with an efficiency factor η.

Since R and η should depend on distinct process, it must be set $\nu_s=\eta_s R_s$ and $\nu_k=\eta_k R_k$ with indices expressing the specific process. For the energy terms, $\sum(E_i^+ - E_{i+1}^-) = E_{DK}^* - \Delta E_s + \Delta E_k$ and E_k = W_m-ΔE_k. Therefore,

$$V = \sqrt{\eta_s \eta_k}\sqrt{R_s R_k}\,\frac{2\sigma b h^2 a}{kT}\exp\left[-\frac{E_{DK}^*/2 + W_m - (\Delta E_s + \Delta E_k)/2}{kT}\right] \quad \text{for } L \gg X^* \qquad (46)$$

Case (ii). Recombination occurs only at straight dislocation sites and hence only double kink formation is enhanced. In this case, $\nu_s = \eta_s R_s$ but $\nu_k = \nu_D$, and $\sum(E_i^+ - E_{i+1}^-) = E_{DK}^* - \Delta E_s$ and $E_k = W_m$, yielding

$$V = \sqrt{\eta_s \eta_D}\sqrt{R_s}\,\frac{2\sigma b h^2 a}{kT}\exp\left[-\frac{E_{DK}^*/2 + W_m - \Delta E_s/2}{kT}\right] \quad \text{for } L \gg X^* \qquad (47)$$

Case (iii). Recombination occurs only at kink sites and hence only kink migration is enhanced. In this case, $\nu_k = \eta_k R_k$ but $\nu_s = \nu_D$, and $\sum(E_i^+ - E_{i+1}^-) = E_{DK}^* - \Delta E_k$ and $E_k = W_m - \Delta E_k$, so that one obtains:

$$V = \sqrt{\eta_k \eta_D}\sqrt{R_k}\,\frac{2\sigma b h^2 a}{kT}\exp\left[-\frac{E_{DK}^*/2 + W_m - \Delta E_k/2}{kT}\right] \quad \text{for } L \gg X^* \qquad (48)$$

The interpretation of the net reduction of glide activation energy ΔE differs depending on which process is enhanced. In any case, the magnitude of ΔE does not exceed the bandgap energy E_g. Dissociated dislocations may be strongly reconstructed so that the dangling bonds along the dislocation cores are all eliminated with the electronic bandgap free from deep states [hir79, mark79, jon79]. Solitons or anti-phase defects bounding reconstruction domains give rise to dangling bond levels located deep in the bandgap. Thus, the solitons fulfill the conditions, deep levels and a strong electron-lattice coupling, favorable for them to act as non-radiative recombination centers operative of the phonon-kick mechanism. Hence it is likely that solitons act similarly to straight dislocation sites for the enhanced DK formation in the REDG effect. In this case, since the kink-pair formation occurs preferentially at the soliton sites, the kink-pair nucleation rate J so far considered must be modified by multiplying a factor a/d, where d is the mean separation of solitons. As d is given by $a\cdot\exp(E_s/kT)$ with the E_s, the soliton formation energy, the kink pair formation energy E_{DK}^* must be interpreted as including E_s. Therefore, if the kink-pair nucleation in darkness can occur everywhere on a dislocation line while that under excitation occurs only at soliton sites, the energy reduction to be observed is smaller by $E_s/2$ in the kink-collision regime and E_s in the kink-collisionless regime.

For kinks, on the other hand, Hirsch [hir79] assumed an unreconstructed kink, whereas Jones considered a reconstructed kink, both trying to account for the doping effect on dislocation mobility. While unreconstructed kink having a dangling bond should give rise to electronic states in the bandgap, the reconstructed kink, according to calculations by Heggie and Jones [heg83, heg82], has no gap states. However, for the REDG effect to occur the kink pair formation must in any case be enhanced. This suggests that kinks formed at solitons, conceivable sites of enhanced DK formation in Si, necessarily have dangling bonds, which may act as non-radiative recombination centers in the kink migration process.

These speculative arguments, however, lack experimental evidences, especially the actual depth of electronic levels associated with the solitons and kinks have not been identified on a definite experimental basis.

3.5.5 Forces acting on Dislocations

Peach-Koehler force

Dislocation movement is based on the presence of driving forces as documented by eq. (49). Detailed calculations of forces on dislocations originating from external stress **σ** applied are complicated and must be done numerically in most cases. For the movement of a dislocation in its glide plane, only the shear stress on this plane needs to be considered. This is so, because only force components lying in the glide plane of the dislocation can have any effect on dislocation glide motion. The component of shear stress acting on the dislocation in the glide plane (Figure 30) in direction of the Burgers vector is called resolved shear stress σ_{res}.

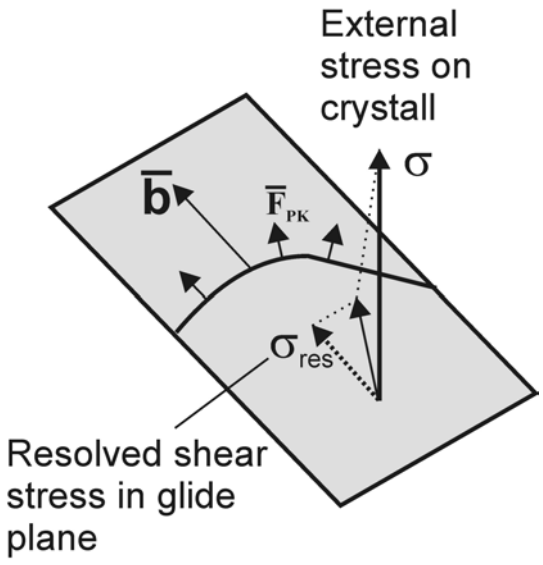

Figure 30. Resolved shear stress acts in slip plane along slip direction.

However, while the resolved shear stress points into the direction of the Burgers vector, the direction of the force component acting on the dislocation, is always perpendicular to the dislocation line direction.

This force component is called Peach-Koehler force and is given by equation [pea50]:

$$F_{PK} = (\hat{\sigma} \cdot \vec{b}) \times \vec{\xi} = \vec{g} \times \vec{\xi} \tag{49}$$

where $\mathbf{g}=\boldsymbol{\sigma}*\mathbf{b}$ so that $g_i=\Sigma\sigma_{ij}b_i$.

The Force F_{PK} as defined above by eq.(49) is always perpendicular to the dislocation line.

The external stress **σ** must exert a same force on a screw dislocation segment that is perpendicular to the force acting on the edge dislocation part to achieve the in-plane expansion of a dislocation loop structure.

One has to note that F_{PK} always perpendicular to plane defined by **b** and **g**, and is always perpendicular to dislocation line labelled as **ξ**. Only in case if the **σ** is shear stress, we obtain the simple Peach-Koehler equation, i.e. (force per unit length) $F_{PK}= \sigma_{res}b$.

Line tension

In reality, dislocations can rarely move in total because they are usually firmly anchored somewhere. For a straight dislocation anchored at two points the Peach-Koehler forces resulting from the resolved shear stress will "draw out" this dislocation into a strongly curved dislocation line.

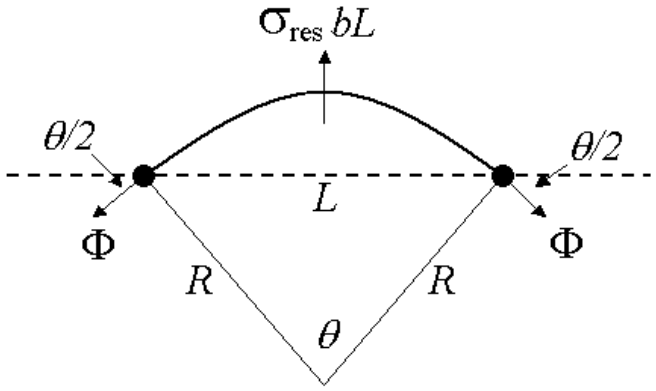

Figure 31. Balance of Peach-Koehler forces acting on dislocation segment with line tension developed.

The illustration in Figure 31 shows that for a certain stress σ_{res}, the Peach-Koehler forces will draw the dislocation into a curved line, but for some configuration there will be a balance of forces, because the line tension pulls the dislocation back.

The dislocation line tends to shorten to minimize energy, as if it had a line tension. Line tension Φ equals to strain energy W per unit length ***l*** and can be expressed as [hir82]:

$$\Phi = \frac{dW}{dl} \approx \frac{1}{2} Gb^2 \tag{50}$$

A mechanical equilibrium will be established as soon as the force $F_{PK}L$ acting on whole segment of length L is balanced by the line tension Φ as a function of curvature radii R. Under equilibrium conditions it holds:

$$F_{PK} \cdot L = \sigma_{res} \cdot b \cdot L = 2\Phi \cdot \sin\left(\frac{\Theta}{2}\right) \tag{51}$$

where Θ-angle between lines perpendicular to the segment in anchor points and b-Burgers vector. From the sketched geometry follows that:

$$\sin\left(\frac{\Theta}{2}\right) = \frac{L}{2R} \tag{52}$$

The formula gives the resolved shear stress necessary to maintain a certain radius of curvature for a dislocation.

3.5.6 Propagation of real glide dislocations

The Peach-Koehler force acting on unit length of dislocation line segment is of the same magnitude for all parts belonging to an identical dislocation loop structure in distinct glide plane. The response to the acting force is amount of all dislocation parts of the loop structure. Since the acting force is shown to be equal for all dislocation segments, the velocity has to be also the same. As a consequence, the expanding dislocations loops should possess a symmetrical shape. However,

experimentally obtained loop structures do not reveal strong symmetry. Clear asymmetry of real loop configurations hints at differences in mobility of the screw and edge type dislocation segments in the loop configuration.

The dislocation mobility, which is expressed as ratio of the dislocation velocity to the acting Peach-Koehler force

$$\mu = \frac{V}{F_{PK}}, \tag{53}$$

may be employed to characterise the specific dynamic dislocation properties relating to the different core structures.

Concept of dislocation mobility can be very useful to analyse behaviour of moving dislocations under similar experimental conditions.

Although by first principle calculations of Peach-Koehler forces are rather difficult, and thus, mobility values cannot be calculated. However in many cases, if for geometrical reasons the Peach-Koehler force may be supposed to be comparable for different dislocation segments, then values of mobility should directly reflect the dynamic states of the distinct dislocation cores.

3.6 Electrical activity of dislocations

3.6.1 Electronic states at dislocations (Read's model)

Dislocations introduced into ideal crystal lattice disturb the periodic lattice potential. Consequently, local electrical, mechanical and optical properties of the crystal are altered in the area of dislocation. The presence of dislocations in the crystal is responsible for the existence of localised electronic states in the energy gap, which give rise to donor and acceptor activity or cause scattering, trapping and recombination properties affecting the behaviour of charge carriers as proved by numerous electrical and optical measurements in several semiconductor materials.

Initiated by an observed amphoteric behaviour of dislocations if the semiconductor matrix converts its type of conductivity, Shockley and Read [hol96] developed a model, which ascribes dislocation-induced electrical effects to the broken chemical bonds assumed to exist in core structures of the dislocations. In the framework of this model, each "dangling bond" may release or capture an electron, i.e. all dangling bond states along the dislocation line represent a half-filled energy band with certain position in energy gap.

Analysing data of photoconductivity spectra, Hall measurements, and electron spin resonance Schröter in [schrö79] states, that the existence of dangling bonds at edge-type dislocations in Si and Ge, and some features of their electronic energy spectrum are well established. Labusch and Schröter [lab75] have derived some basic properties of the dislocation electron states from the experimental results on the Hall effect and carrier lifetime measured in deformed Si and Ge by means of a statistical treatment. The results are summarised in Figure 32.

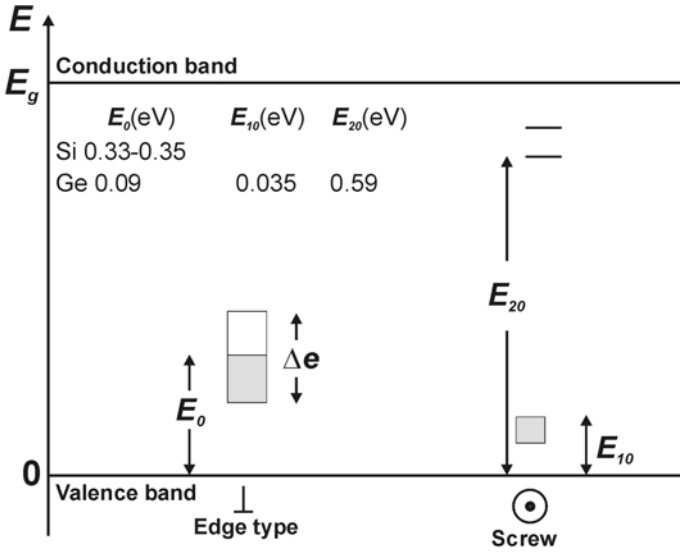

Figure 32. Parameters of dislocation states for Si and Ge, as derived from Hall measurements [lab75].

Within the simple dangling-bond model, a 60° dislocation (Figure 12) of the shuffle- or the glide-set is associated with a half-filled band. A screw dislocation has no dangling bonds, but dissociated into two 30° partials, having dangling bonds for which half-filled bands have to be expected.

The dangling bond concept offers an empirical quantitative aspect by means of the line density of dangling bonds. This quantity is available as a structure parameter of the dislocation core under consideration and may be correlated with experimentally determined dislocation properties such as line charge built up due to carrier trapping at the defect. The line charge q is given [read54, read54a] by:

$$q = f \cdot n_{DB},$$

where n_{DB} is the dangling bond density and f is an occupation factor ($f \approx 0.1$). The situation of charged dislocation is illustrated in Figure 33 (a).

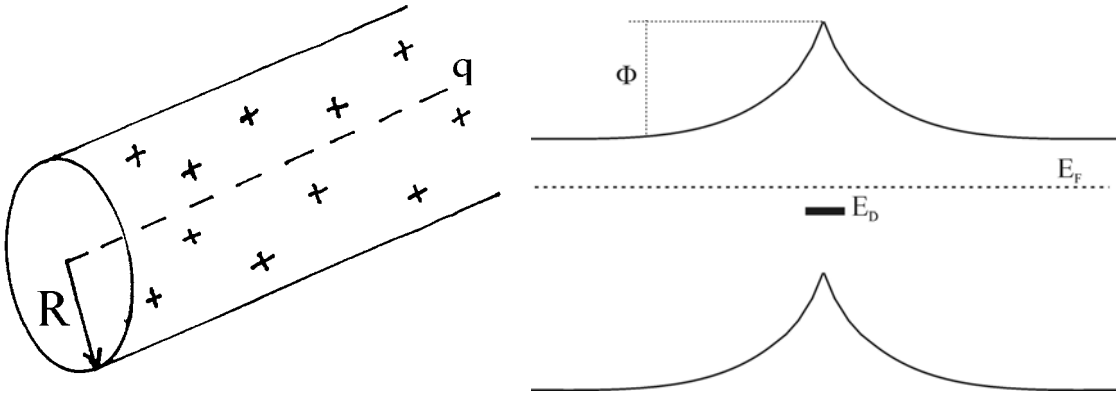

(a) (b)

Figure 33. The Read [hol96] model of charge dislocations. (a) cylinder of space charge with radius R. (b) energy band structure scheme (E_D-dislocation state, E_F-Fermi level, Φ-band bending).

The line charge q is due to majority capture and appears to be screened by a region of space charge originating from the donor ions in the vicinity.

The electrostatic configuration results in a band bending as sketched in Figure 33 (b), it is described by the potential [ale91]:

$$\phi(r) = \frac{q}{\varepsilon_0 \varepsilon_r \pi R}\left[\frac{R^2 - r^2}{4} + \frac{R^2}{2}\ln\left(\frac{R}{r}\right)\right] \tag{54}$$

(here ε_0-, ε_r - absolute and relative dielectric constants respectively, r-radial distance)

The scheme in Figure 33 (b) may be regarded as generalized dangling bond model as applied by many authors to discuss experimental findings on the electrical activity of dislocations.

Besides studies of other authors, Ossipyan and Petrenko have performed experiments on the movement of charged dislocations during plastic deformation of $A^{II}B^{VI}$ crystals [osip79]. The electrical current density produced by moving dislocations was measured and analysed with respect to the plastic flow. The line charge q has been determined in wurtzite CdS for different dislocation types. The authors could show that the screw dislocations were uncharged, whereas the edge-type dislocations exhibited distinct line charge densities. In [hol62, osip68] it was shown that the charge of all the dislocations is likely to correspond with dangling bond configurations related to the core structures.

However other authors [bul97] based on theoretical calculations state that the bonds in dislocation cores have to be reconstructed in order to minimize energy. Furthermore, the results of advanced theoretical works yield dislocation-bound electronic states related to perturbation of the periodic lattice potential, in particular, in the region of the defect-caused strain field [far99].

Thus, the dangling-bond concept is expected to fail at many cases of distinct electrical dislocation properties revealed experimentally. On the other hand, albeit sophisticated quantum mechanical calculations of electronic structure for dislocations have been done, there is no convincing correspondence between theoretical predictions and experimental data gained from electrical and spectroscopic data. In spite of the new theoretical concepts, the dangling-bond model is often used so far as a first approximation to explain experimentally recognised dislocation behaviour.

In this work the dangling-bond concept is utilized to distinguish dislocations of different type in ZnO in respect of their recombination active properties.

3.6.2 Dislocation recombination activity

Dislocations in semiconductors are known to be very efficient recombination centers. This causes a pronounced impact on luminescence.

A very detailed theoretical descriptions of the formation of CL signal at the defects in semiconductors have been presented in [her84, her87a, her87b].

In the SEM-CL mode a defect-related contrast exists in panchromatic (c_{CL}) and monochromatic form. Distinguishing matrix luminescence contrast (c_0) from contrast part (c_{DL}) due to dislocation-bound luminescence (DL) leads to

$$c_{CL} = c_0 + c_{DL} \tag{55}$$

c_{CL}, c_0, c_{DL} can be analysed separately in the experiments.

In the framework of the excess carrier processes under e-beam excitation the generation rate and recombination flux are balanced. Summarising radiative and non-radiative recombination determines the total recombination rate. The minority carrier lifetime is locally reduced by dislocation-induced recombination, thus:

$$\frac{1}{\tau}=\frac{1}{\tau_{nr}}+\frac{1}{\tau_r}+\frac{1}{\tau_D}, \tag{56}$$

where τ_{nr}, τ_r relate to matrix recombination and τ_D is the dislocation related carrier lifetime. Any dislocation bound carrier recombination results in a reduced amplitude of matrix emission.

Description of CL contrast by the Volume-Recombination-Model (VRM) [schr89b] supposes that the recombination activity of the dislocation is characterized by total defect strength:

$$\bar{\lambda} = \pi \cdot r_D^2 \,/\, \tau_D \tag{57}$$

which comprises both the radius r_D of defect cylinder and τ_D the carrier lifetime related to defect-induced recombination.

Figure 34 represents a recombination kinetic model in the defect area for an n-type semiconductor as proposed by [hil98]. This model is based on Self-consistent barrier-controlled Shockley-Read-Hall (SBCSRH) model of recombination process to describe the nonradiative electron-hole recombination at a dislocation [kus95].

g(r) = local inhomogene generation funktion
G = total generation rate
E_T, Q_T = defect state, charge of defect
J_n, J_p = defect induced recombination flux

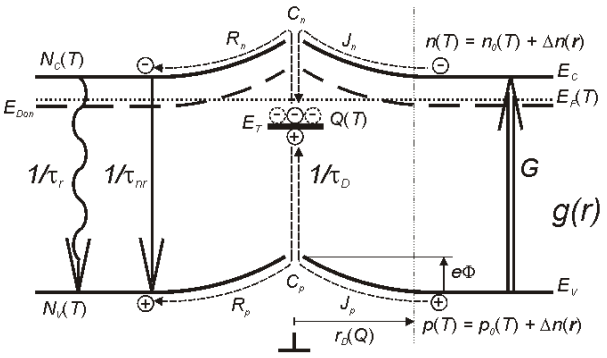

Figure 34. Schematic of recombination in the defect area for in n-type semiconductor [hoer01].

Shockley-Read-Hall kinetics is used taking into account the charge state Q of the defect due to majority capture. Q creates the barrier Φ potential within r_D and varies self-consistently with altered local majority density and capture of minorities. The recombination via the defect state E_T is governed by Φ due to attracting minorities and controlling the majority flux into the defect states.

As recombination-kinetic defect parameters emerge: E_T-electronic defect state, N_L-line density of states, c_n,c_p-electron and hole capture coefficients, Φ-space charge barrier, f_T-dynamical occupation factor.

The total defect strength $\bar{\lambda}$ represents the factor of proportionality between the recombination fluxes J_n or J_p and the local excess carrier density [wil85], thus

$$\bar{\lambda} = \frac{J_n}{\Delta n_D} = \frac{J_p}{\Delta p_D} \tag{58}$$

For the recombination flux:

$$J_p = N_L \cdot c_p \cdot \left[f_T \cdot p \cdot \exp\left(\frac{e\cdot\Phi}{kT}\right) - (1-f_T)\cdot N_V \cdot \exp\left(-\frac{e\cdot(E_V - E_T)}{kT}\right)\right] \tag{59}$$

or

$$J_n = N_L \cdot c_n \cdot \left[(1 - f_T) \cdot n \cdot \exp\left(-\frac{e \cdot \Phi}{kT} \right) - f_T \cdot N_C \cdot \exp\left(-\frac{e \cdot (E_C - E_T)}{kT} \right) \right] \tag{60}$$

holds, where N_C, N_V, E_C, E_V are the conventional quantities in semiconductor physics and n, p correspond to the carrier densities under focussed electron beam excitation.

The defect strength $\bar{\lambda}$ is the only physically relevant parameter to characterise the electrical activity of the dislocations, it is direct proportional to N_L. The temperature dependence of the recombination flux directly relates to $\bar{\lambda}(T)$ which allows to extract the recombination-kinetic defect parameters. Values for $\bar{\lambda}$ can be gained from experimental CL contrast studies by analysing of measured CL defect contrast employing the theoretical contrast profile function

$$c_{CL}(\xi) = \bar{\lambda}(r_D, \tau_D) \cdot c_0^*(\xi, \xi_D, U_b, \alpha_0, L, \tau) \tag{61}$$

in order to get $\bar{\lambda}$ as the fitting parameter. The theoretical defect contrast profile with regard to SEM-regime is given [hil98] as a distinct profile functions depending on ξ, ξ_D as probe beam and defect position, respectively, U_b – beam voltage, α_0 and α_D – optical absorption coefficients of matrix- or defect-related luminescence, L – diffusion length, and τ total lifetime of minority carriers in matrix.

4 Experimental methods

4.1 Sample materials and preparation

For investigation dynamics and electrical activity of glide dislocations in typical compound semiconductor with zincblende and wurtzite lattice structure GaAs and ZnO bulk samples with low-index surface were chosen.

The GaAs bulk crystals were Si-doped n-type with carrier concentration about $5x10^{17}$ cm^{-3} and had $(\bar{1}\bar{1}\bar{1})$ B surface orientations.

The ZnO samples have been prepared from (0001) substrate wafer or from bulk crystal in form of hexagonal prisms that provide $(10\bar{1}0)$ and $(11\bar{2}0)$ planes as samples surfaces to be studied. The material was colourless and transparent by sight.

The ZnO materials were not doped, n-type with carrier concentration in the range of 10^{16} cm^{-3}. Both the GaAs and ZnO crystals showed low grown-in dislocation density less then $10^4 cm^{-2}$.

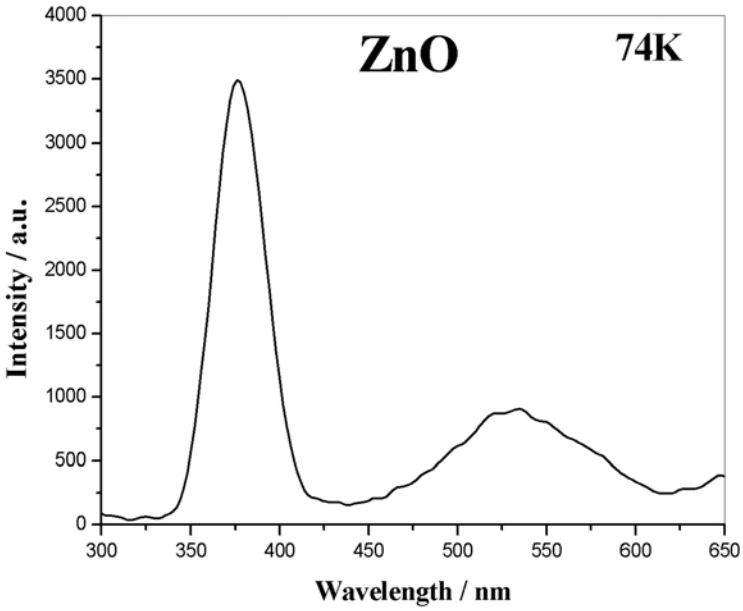

Figure 35. Low temperature cathodoluminescence spectra of undoped ZnO monocrystalline hexagonal prism.

Figure 35 shows representative CL spectra for the ZnO monocrystalline hexagonal prism used in experiments. As indicated, the two bands had peaks at 375nm and 530nm that were related to excitonic states and oxygen vacancies [stud98, van96] respectively.

On properties of ZnO

Zinc oxide has attracted a significant amount of attention in the past several years since it is wide band gap the semiconductor finds a number of applications in catalysis, gas sensing, and the fabrication of varistors and other microelectronic devices. ZnO is appropriate for use as a transparent electrode in electronic and electric devices because of its transparency in the visible light region. Recently, ZnO-based optoelectronic devices, e.g. light-emitting diodes [ohn98] and lasers [oht00], have been developed. For the fabrication of such devices, high quality crystalline material with low defect density is necessary to achieve light emission with high efficiency.

ZnO single crystals are being grown in bulk by means of hydrothermal, melt, and seeded vapor phase (SVP) methods. Grown technique yields ZnO wafers having dislocation densities in the 10^4-10^5 cm^{-2} range and impurity level (causing n-type) in the 10^{16} cm^{-3} range.

Regarding the ZnO WZ lattice structure the four low-index surfaces are of interest: non-polar $(10\bar{1}0)$ and $(11\bar{2}0)$ surfaces, and the polar (0001)-Zn and $(000\bar{1})$-O surfaces.

The enormous potential for use of ZnO in optoelectronic applications can be explained with reference to in Table 4-1 below which contains key properties of ZnO

Table 4-1.: General zinc oxide physical properties.

Type of lattice	WZ
Lattice constants a and c / Å	a=3,2495, c=5,2066
Ratio (c/a)	6,137
Energy gap E_g / eV	3.37 (RT)
Exciton binding energy / meV	60
Dielectric constant ε	8.75-10.8
Melting temperature T_m / ^oC	2250
Vicker's hardness / GPa	1.75
Young's modulus / GPa	161-230
Shear Modulus / GPa	45.5
Poisson ratio	0.36

4.2 Fundamentals of cathodoluminescence mode in SEM

Cathodoluminescence (CL) is one of the interaction products originating from high-energy electron excitation of a non-metallic target (Figure 36) like semiconductor or insulating materials. CL represents the light emission associated with the materials excitation by the electron beam. CL radiation comes from the radiative recombination of non-equilibrium charge carriers such as electron–hole pairs excited in semiconductors by the impinging electrons. There are several luminescence channels in semiconductors. The recombination can be attained by various radiative transitions between the conduction band (E_c) and valence band (E_v) by excitons (E_e) or from donor (E_d) and acceptor (E_a) levels induced by dopants, impurities and point defects. Thereby, the energy of an emitted photon equals the difference between the initial and final energy levels of the captured excess electron.

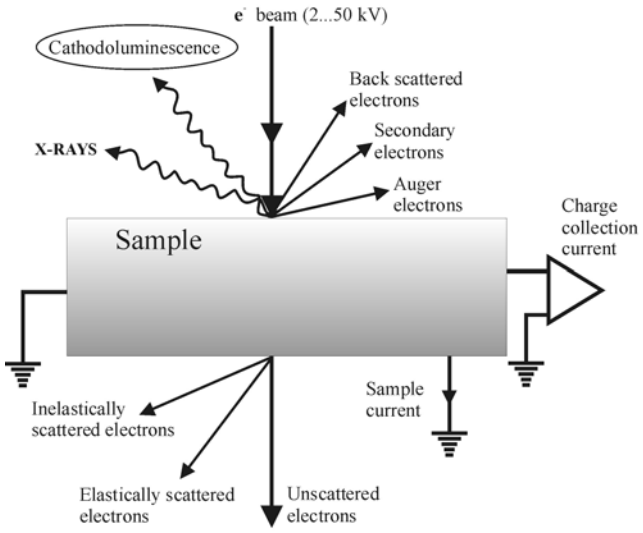

Figure 36. Signals available from electron-target interaction in case of a semiconductor sample in scanning electron microscope (SEM).

Electron-hole pair recombination is also realised by nonradiative processes such as Auger effect or multiple-phonon generation. In many cases lattice defects can serve as non-radiative recombination centres. Particularly, dislocations may act as local non-radiative centres of carrier recombination.

The scanning electron microscope (SEM) is a very powerful tool to perform CL measurements. The SEM electron optics is utilized to produce a focused e-beam for exciting small region of a sample. The e-beam diameter in the SEM is of the order of nanometers. The excited volume depends on the acceleration voltage of the electron beam. Electron energies ranging from 200 V to 50 keV (0.05-10nA) can be used in the SEM. The resulting probe volumes range from tens of nanometers to a few microns in diameter.

The light emitted from such region is captured by a light collecting optics, and an optical spectrum is obtained using a monochromator equipped with a high-efficiency light detector. By changing the energy of the electron beam it is possible to perform a depth profiling of the optical properties of the specimen. Scanning of the e-beam probe in frame mode produces images of the panchromatic light emission intensities or with specific wavelengths emitted. The lateral resolution of the technique depends mainly on the diffusion length of the excited carriers. It can be as small as the electron probe diameter in the case of very small diffusion lengths and low beam voltages.

There are several requirements concerning the specimens used. Electrically conducting samples are required in order to achieve high spatial and spectroscopic resolutions. The specimen should be stable under electron beam irradiation.

However, there are some limitations, because high magnification imaging requires high electron dose, so specimens need to be relatively beam insensitive. Specimens that degrade under the electron beam should be avoided, i.e. there should not occur any degradation or damage phenomena.

Suitable microscopes to performing SEM-CL are to be used, because the radius of the volume sampled by CL is much larger than the probe diameter. The CL sensitivity in the SEM for CL is primarily determined by the high electron brightness of its electron source. LaB_6 guns are preferred to field-emission guns. Cold stages (liquid N or He) are necessary in order to observe optical transitions without thermal broadening.

4.3 Experimental setup for SEM-CL

Two conventional scanning electron microscope apparatus (Jeol JSM6400, Tesla BS300) equipped with particular attachment have been used to conduct the SEM-CL experiments for studying the defects behaviour in the semiconductor crystals samples. To perform measurements at low temperature in the range 4.5K-300K for getting temperature dependences, both instruments are combined with the cooling stages (CF302) from Oxford Instruments Ltd. Controlled cooling down of the samples could be done by means of liquid helium or liquid nitrogen, respectively, flowing through a mini-cryostat integrated in the sample stage. The SEM-CL investigations were made utilising panchromatic and monochromatic mode.

The SEM-CL setup used is sketched in Figure 37.

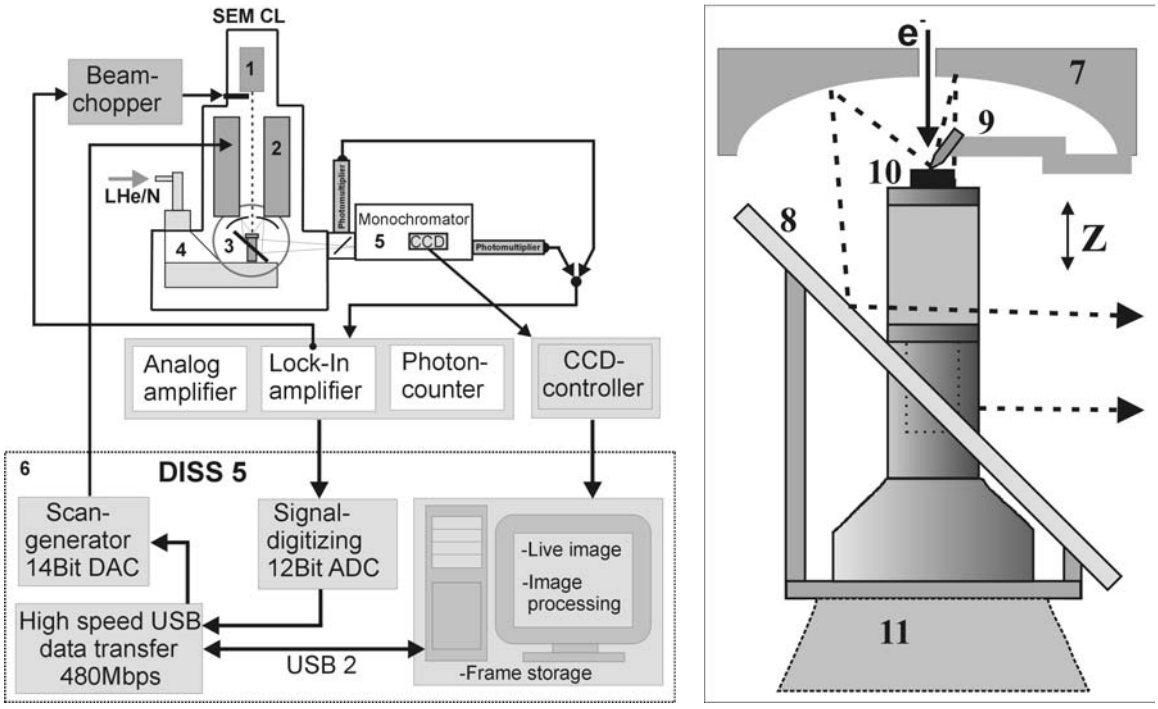

(a) (b)

Figure 37. Scheme of SEM-CL setup with cooling stage (a). The device for the in-situ deformation (b).

The operation principles of the setup are follow: electrons emitted from cathode (1) are focused by an electron optics (2) on the sample surface (3). The sample can be cooled from 300K down to 4.5K by means of the cooling stage (4). The CL radiation collected by light optics (see Figure 37 (b) for details) passes through a special monochromator (5) to different detectors to be measured in pan- and monochromatic mode. The digital image scanning system DISS 5 operates the electron beam during measurements and acquires the CL signal data quantitatively. It provides special capability of kinematical SEM operation.

For the first time the special micro-indentation setup was developed and installed for the purpose of local plastic deformation under in-situ conditions.

The tool attached for the in-situ deformation is shown in Figure 37 (b). It consists of indenting needle (9) integrated into the optical collection system made up by the spherical mirror segment and a flat 45^{o}-mirror (7, 8). Indenting and scratching can be carried out with the needle (9) by mechanically touching the sample (10) during vertical movement of sample stage.

Plastic micro-deformation by means of in-situ scratching and indentation was used at temperature between 295K and 72K to introduce fresh glide dislocations in the crystalline samples examined. Sample treatment and correlated CL observation could be carried out simultaneously.

The thermal contact with the cryosystem (CF302, Oxford Instruments, UK) is achieved through the “dovetail”-holder (11).

The working parameters of the SEM-CL apparatus are:

1) resolution: 100 nm
2) image size: 512x512pixels
3) contrast gradation: 8-bit grey scale resolution (255 levels)
4) spectral resolution: 1 nm
5) wavelengths range: form 200 to 1800nm

4.3.1 Kinematical SEM-CL

Technique of kinematical SEM-CL has been developed as a special tool to reveal dislocations as extended mobile recombination centers in semi-conducting crystals [hoe01]. It may be applied to in-situ plastic deformation [hoe01a] resulting in generation and thermally activated propagation of glide dislocations, and is also applicable under specific conditions of the REDG effect [mae81]. Kinematical SEM-CL studies comprise the observation of dislocation dynamics on microscopic scale as well as an analysis of the CL contrast behaviour at both moving and resting dislocations. Such kind of experiments aims at disclosure of any correlation between dynamics and recombination behaviour at identical defect segments.

Kinematical mode of SEM-CL is realised by means of generating and storing image sequences with frame rates up to real-time imaging condition. The kinematical CL technique can document a complete history of dislocation movement and corresponding CL defect contrast behaviour over a long period. The kinematical SEM-CL is based on an advanced digital scanning and signal acquisition system available for the real-time imaging and fast data processing. Optimum frame rates being available depend on the pixel acquisition times which are limited by a given signal-to-noise ratio, and thus, result from frame sizes chosen as well. In order to save quantitative CL information over dynamic range of 8 bits, uncompressed AVI format must be exploited for movie storage. Sequential CL imaging based on panchromatic signal acquisition with frame rates up to 10 fps according to a minimum pixel acquisition time of 0.4 μs for frame size 500x500 is performed by utilizing the digital acquisition and processing system DISS 5 (point electronic GmbH).

4.4 Description of SEM-CL signal

Figure 38 contains schematically carrier and photonic processes occurring in the SEM-CL experiments. The carrier behavior is primarily represented by the electron-hole pair generation distribution g(r), the minority carrier diffusion length $L = \sqrt{D\tau}$, and the radiative and non-radiative bulk lifetimes τ_r and τ_{nr} which determine corresponding recombination rates R_r and R_{nr}.

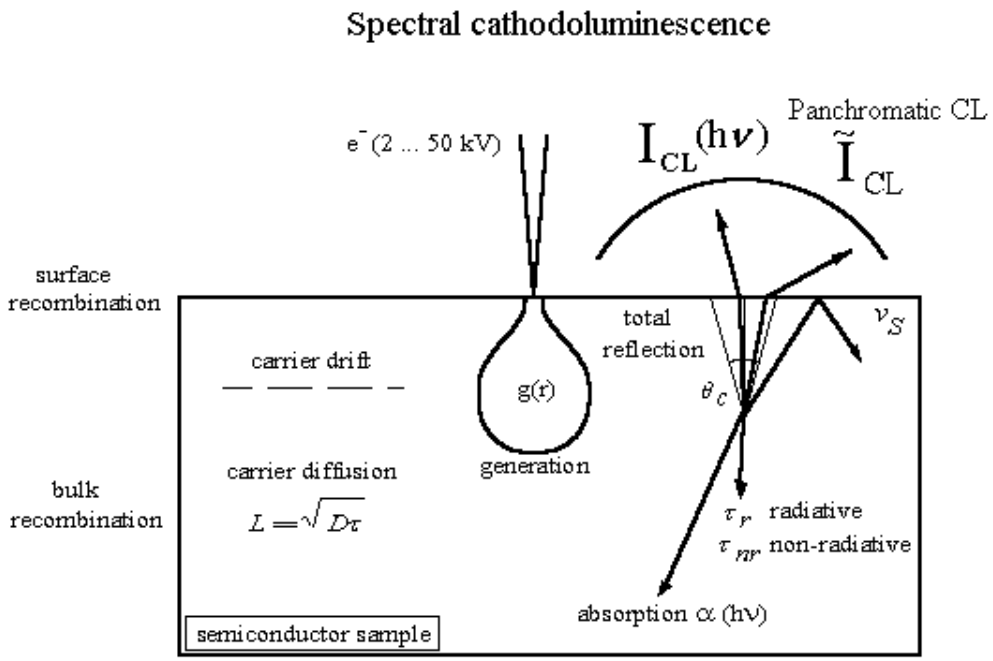

Figure 38. Scheme of SEM-CL experiments.

The continuity equation for the time-dependent excess minority carrier density q(r,t) is established as the balance of diffusion and drift currents, total recombination, and beam induced generation rates at each point r of the sample:

$$-\frac{\partial}{\partial t}q(\mathbf{r},t)+\left[D\nabla^2 q(\mathbf{r},t)-\mu\nabla\left(\mathbf{F}(\mathbf{r},t)q(\mathbf{r},t)\right)\right]-\frac{1}{\tau(\mathbf{r})}q(\mathbf{r},t)=-g(\mathbf{r},t) \qquad (62)$$

Here the total minority carrier lifetime $\tau(r) = (\tau_r^{-1} + \tau_{nr}^{-1})^{-1}$ is a defect-related function of the position r and D- the diffusion coefficient, μ- the minority carrier mobility. The validity of zero requires a linear recombination model such as band-to-band recombination in the low-injection regime so that the majority carriers do not need to be considered. If electric fields **F**(r,t) zero, the stationary balance $dF/dt = 0$ is expressed by the steady-state continuity equation for diffusion:

$$D\nabla^2 q(\mathbf{r})-\frac{1}{\tau(\mathbf{r})}q(\mathbf{r})=-g(\mathbf{r}) \qquad (63)$$

Taking into account the actual sample geometry, boundary conditions are to be fulfilled as

$$D\left.\frac{\partial q}{\partial n}\right|_{\mathbf{r}=\mathbf{r}_S}=v_S q(\mathbf{r}_S) \qquad (64)$$

for any surface or interface at r_S where a normal diffusion current is related to a non-radiative surface/interface recombination velocity v_s. The carrier density must vanish ($q(r)\to 0$ for $r\to\infty$) in directions with practically infinite sample extensions

Different models have been used in the literature [hil98] for the generation rate. To perform a correct quantitative analysis of experimental data, one has to use a realistic generation distribution $g(\mathbf{r};U_b) = G_0\, g_r(r,z)\, g_z(z)$ (G_0 is the total carrier generation rate). The basis for the CL contrast calculation are the equations (62) and (63), respectively.

The spectral CL signal defined as photon flux leaving the sample surface and collected by an ideal spectrometer [her84] is given by the integral of the radiative recombination rate over the

sample volume Ω_s corrected by losses due to spectral optical absorption $\alpha(h\nu)$ and total reflection at the sample surface for escape angles larger than the critical angle Θ_c:

$$I^{CL}\left(U_B, h\nu\right) = Q\left(h\nu, \mathbf{r}\right) \int_0^{\Theta_c} \sin\Theta \cdot d\Theta \cdot \int_{\Omega_s} d^3\mathbf{r} \cdot \frac{q(\mathbf{r})}{\tau_r} \cdot e^{\left(-\alpha(h\nu)\cdot z/\cos\Theta\right)} \tag{65}$$

where $Q(h)$ denotes the relative internal spectral distribution of the recombination radiation. In the case of panchromatic, spectrally integrated CL experiments, eq. (65) remains correct if "effective" parameters for quantum efficiency $\bar{Q}$ and $\bar{\alpha}$ absorption are introduced. $I^{CL}(U_B,h\nu)$ is governed by the local carrier density q(r) which can be deduced from eq. (62). It should be noticed that q(r) directly depends on $\tau(r)$ that is affect by the presence of any recombination active defects.

4.4.1 CL contrast of extended defects

For comprehensive studies on the formation of the CL contrast from dislocations it is necessary to take into account the intrinsic nature of dislocation related recombination, as well as effects due to dislocation interaction with surrounding point defects. Moreover, there are additional geometrical contrast factors too. Generally, extended defects are supposed to change the local recombination properties of the sample. Dislocations in semiconductor crystals are known to be very efficient recombination centres. Hence, their electric activity resulting in a recombination contrast has to be considered with respect to bulk recombination rates. The knowledge of matrix signals and corresponding parameters is therefore a general requirement for quantitative analysis of the defect contrasts. The model case of a surface-parallel dislocation as applicable for many both misfit and glide dislocation geometries considered in [hil98] is shown in Figure 39. In Figure 39 (a) the situation for the carrier generation and recombination processes in the vicinity of a dislocation line is outlined. The Volume-Recombination-Model for the dislocation is utilized.

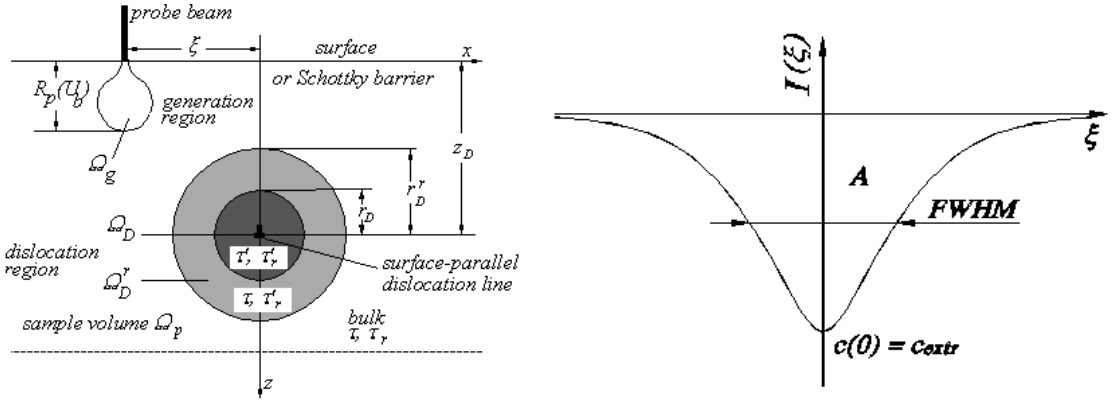

(a) (b)

Figure 39. (a) Configuration of SEM-CL contrast measurement at a surface-parallel dislocation [hil98]. (b) Scheme for the carrier generation and recombination processes.

In the volume recombination model, the dislocation is characterized by a cylindrical region r_D where the total lifetime τ' differs from the bulk value. A defect-induced recombination strength [don78] is defined as:

$$\gamma = \frac{\tau}{\tau'} - 1 = \frac{\tau}{\tau_D} \tag{66}$$

The radius r_D of the dislocation cylinder may be preliminarily interpreted as a "capture cross section" but one can also try to infer this region from physical dislocation properties such the extension of the core region, strain field or the space charge region of a charged dislocation.

However, it can be shown that for $r_D << L$, where L is minority carrier diffusion length, the shape of the contrast profile of the surface-parallel dislocation line is independent of r_D. In this case, γ and r_D cannot be determined separately but form together a so-called defect strength λ . On the other hand, impurity decoration or a gettering-induced denuded zone may cause a larger extension of the defect-related region as shown e. g. for GaAs in [bal76]. In such a situation or if specific defect bound emission occurs, the radiative recombination can be also affected. This is considered by introduction of a second defect cylinder Ω_D^r of radius r_D^r with modified τ_r' and radiative recombination strength $\gamma_r = \tau_r/\tau_r' - 1$. In principle, this model is able to describe the complex structure of the well-known "dot-and-halo" contrasts.

As the e-beam probe approaches the dislocation site, the SEM-CL signal responds by decreasing as sketched in Figure 39 (b). A single line scan generates a CL intensity profile showing a local minimum at the defect position. The profile dip defines the defect-related CL contrast value *c* as part of the CL contrast profile:

$$c(\xi) = \frac{I^{CL}(\xi) - I_o^{CL}}{I_o^{CL}} \tag{67}$$

where $I_0^{CL} = I_0^{CL}(\xi \to \infty)$ is the matrix signal.

This relationship may be directly applied to SEM-CL experiment. On the other hand, the CL contrast profile may be described by:

$$c_{CL}(\xi) = \overline{\lambda}(r_D, \tau_D) \cdot c_0^*(\xi, \xi_D, U_b, \alpha_0, L, \tau) \tag{68}$$

This gives a rewritten form the CL defect contrast value as:

$$c = \overline{\lambda} \cdot c^* \tag{69}$$

where the defect strength $\overline{\lambda}$ appears as a parameter characterising the defect recombination activity. There is an access to simulation calculations for the profile function c^*, thus, from quantitative CL contrast measurements the parameter $\overline{\lambda}$ may be determined. The $\overline{\lambda}$ value represents a “linear recombination velocity” specific for the extended line defect.

5 Results and discussions

5.1 Investigation of dislocation structures in ZnO

5.1.1 As grown dislocation structures

Dislocation structures in ZnO are expected to be formed according to the wurtzite type lattice of the mono crystalline material. Until now, no systematic investigation of grown-in dislocation configurations or dislocation structures produced by plastic deformation can be found in the literature. For the first time, more detailed studies on the dislocation behaviour in ZnO bulk crystals has been performed here by means of the method SEM-CL to reveal microscopic dislocation distributions including imaging of single dislocation arrangements allowing recognition of different types of dislocations. Only electrical active dislocations will be recorded.

The ZnO bulk materials both (0001) substrate wafers and hexagonal prisms exhibited a low average dislocation content. However, locally enhanced dislocation densities have been observed in particular areas of the prismatic crystals. Figure 40 is a CL picture of the pyramidal termination of a ZnO prism.

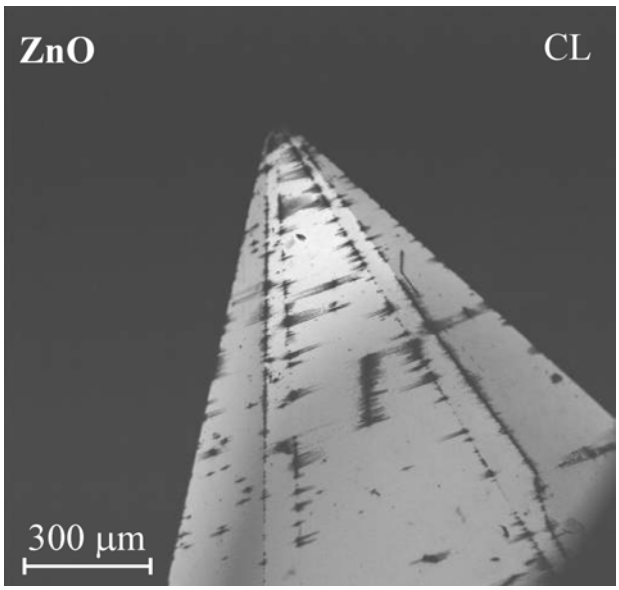

Figure 40. CL image taken from the pyramidal termination of a hexagonal prismatic ZnO crystal.

The CL dark patterns display defected regions existing in vicinity of the edges of the hexagonal pyramid. Similar defected regions were found along edges of the $(10\bar{1}0)$ faces.

Figure 41 (a) and (b) are the CL images zoomed from the same ZnO prism sample. The edge between two neighbouring faces $(10\bar{1}0)$ is accompanied by a very strong dark contrast due to the dislocations density increased. Extended arrangements of single dislocations are seen. Furthermore, propagation of the dislocations in distinct crystallographic direction of different glide planes may be deduced.

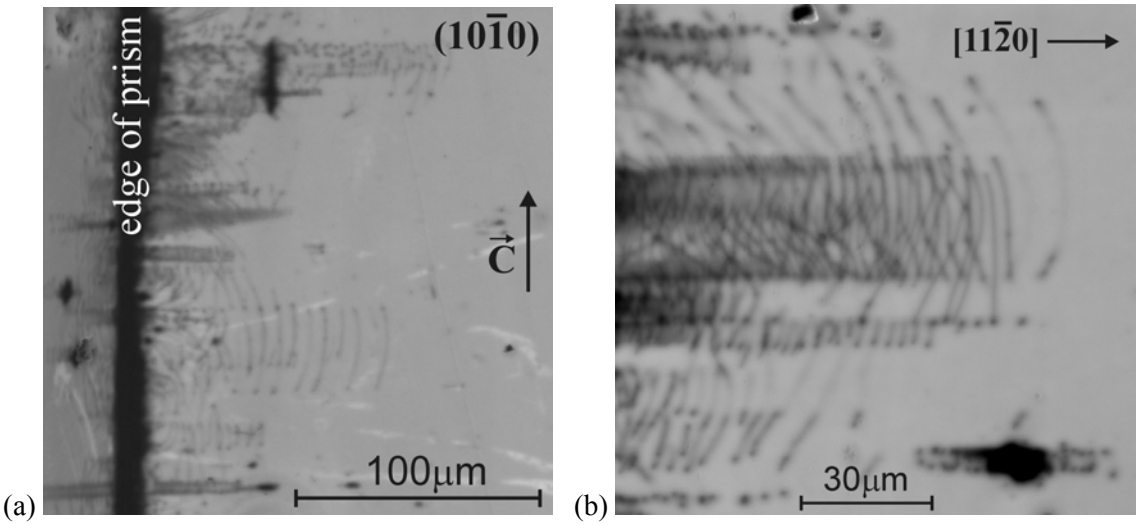

Figure 41. CL images of as grown dislocations in ZnO (10-10) sample surface.

The grown-in glide dislocations are immobile and form prismatic half loops. Rounded and random dislocation line shapes point to increased temperature at which the crystal was grown.

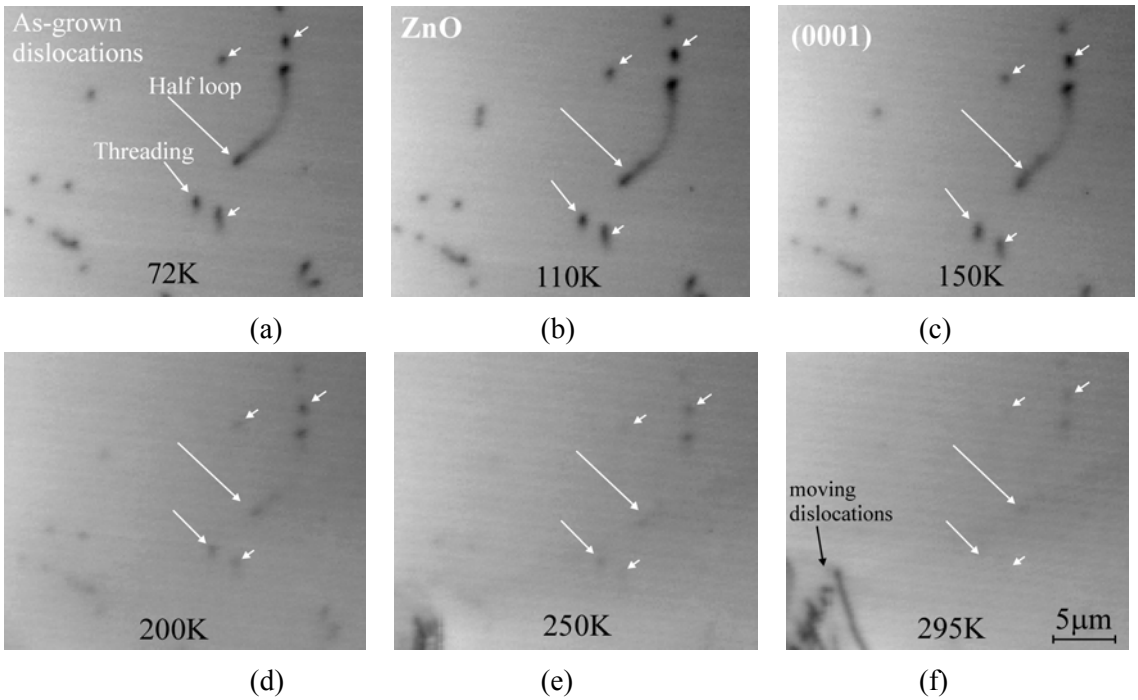

Figure 42. Sequence of CL images taken at distinct temperatures, showing changes (vanishing) of CL contrast upon heating of the as-grown dislocations observed at (0001) ZnO (a)-(f).

Figure 42 shows CL patterns of individual dislocations as observed on (0001) ZnO sample, threading segments and a half-loop like defect configurations are indicated. In this particular case

of as-grown dislocations, the CL contrast vanishes at higher temperature. The CL contrasts of glide dislocations, which moved into the area of image, are seen in Figure 42 (e, f).

5.1.2 Glide dislocations

To obtain a more general insight into the dislocation structure being realized in ZnO, appearance of glide dislocations has been analyzed. The glide dislocations were introduced by means of local plastic deformation utilizing micro-indentation and scratching on the low-index (0001), $(10\bar{1}0)$ and $(11\bar{2}0)$ sample surfaces. The generated dislocation configurations comprise a set of the main slip dislocation types.

Figure 43 represents the results of ex-situ scratching experiments on (0001) ZnO. Scratches approximately parallel to $[10\bar{1}0]$ have been made with different loads between 5p to 15p. The CL picture images the near-surface dislocation arrangements produced. Even at the scratches for lowest load the dislocations are distributed over a range of about 150 μm in extension. Defect density varies with distance from scratch center.

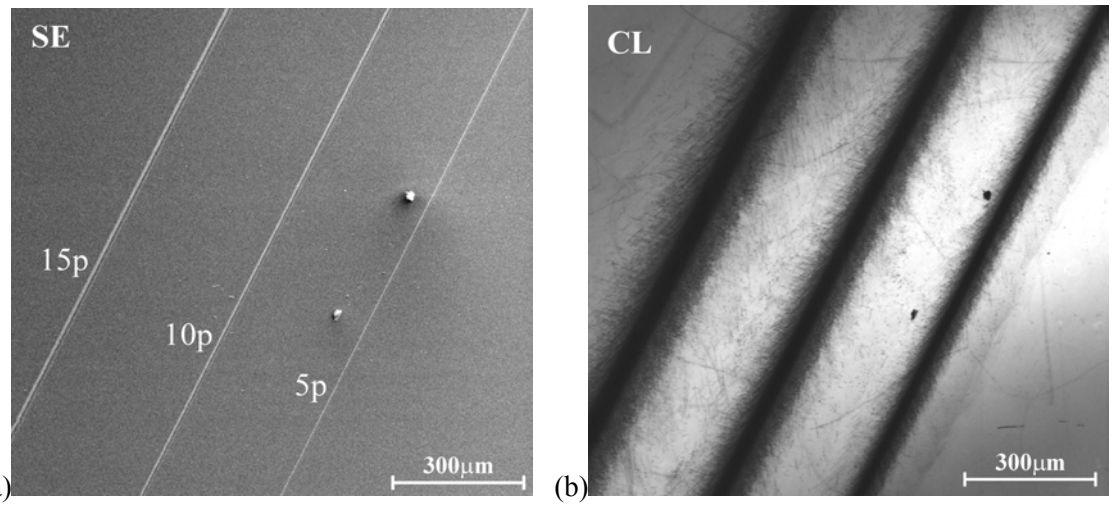

(a) (b)

Figure 43. Micrographs of ex-situ scratching of (0001) ZnO at 300K. (a) SEM SE mode. (b) SEM-CL mode.

As seen in Figure 44, there are characteristic differences in the dislocation arrangements. The scratches have generated a number of threading dislocations spreading along the $[\bar{1}2\bar{1}0]$ directions. Higher density of threading defects is observed near the scratch produced at higher loading. Surface-parallel dislocation lines travelling over distances of 100μm can be seen near the scratch with lower loading. The line segments do not rest primarily along the corresponding Peierls valley directions.

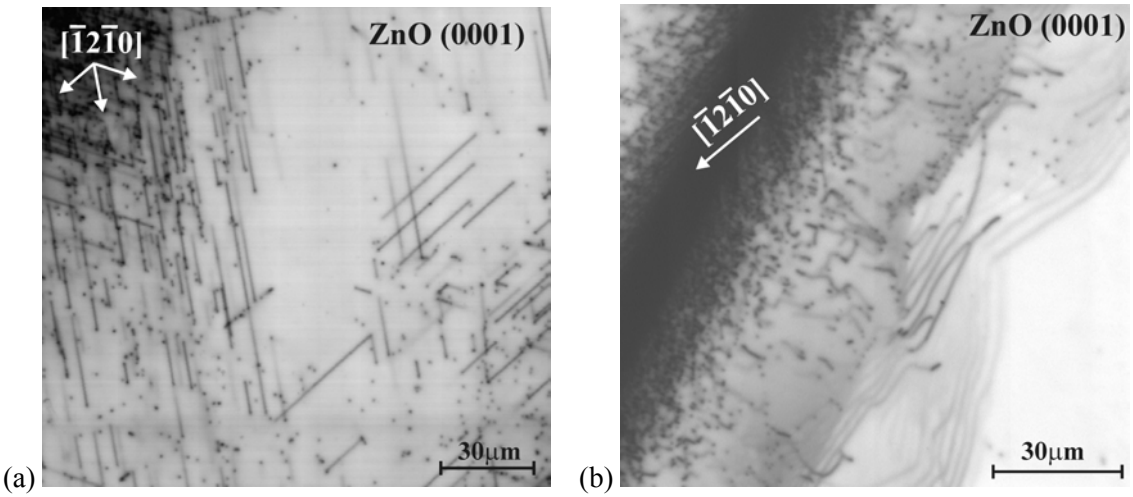

(a) (b)

Figure 44. Magnified dislocation structures: (a) near the highly stressed scratch (15p); (b) near low-stress scratch (5p).

The dislocation configurations shown in Figure 44 (a, b) may be ascribed to four particular slip systems activated. Operating slip systems could directly be identified by means of in-situ scratching experiments. In-situ scratching was performed on a (0001) plane surface of the ZnO substrate at low temperatures. Kinematical SEM-CL documented the entire procedure of scratching. Loading stress was changed in order to observe propagation of dislocations under different stress conditions.

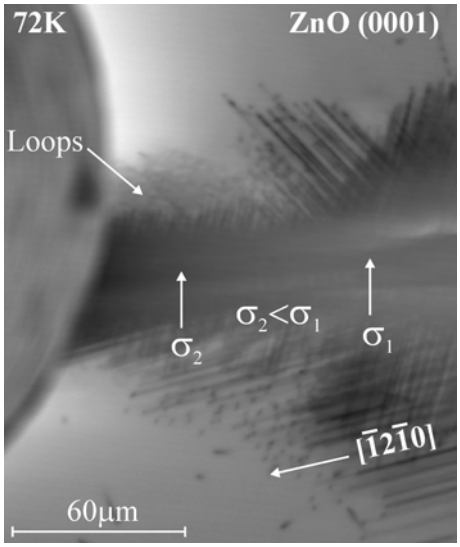

Figure 45. In-situ scratching being performed on (0001) ZnO plane with high σ_1 and low σ_2 loading.

Figure 45 is a selected frame of entire SEM-CL movie. Threading types of dislocations are found to appear at the higher stress σ_1 on the upper and lower sides of the scratch, while loop structures were formed at the lower stress σ_2 only at the upper side. The appearance of loops at lower stresses completely corresponds with results on ex-situ experiments obtained earlier.

Micro-indentation yields better-resolved dislocation configurations because of realising more symmetric geometry for the glide systems activated. Indenting on (0001) sample surface results in 6-fold symmetry of the dislocation arrangement as proved in Figure 46.

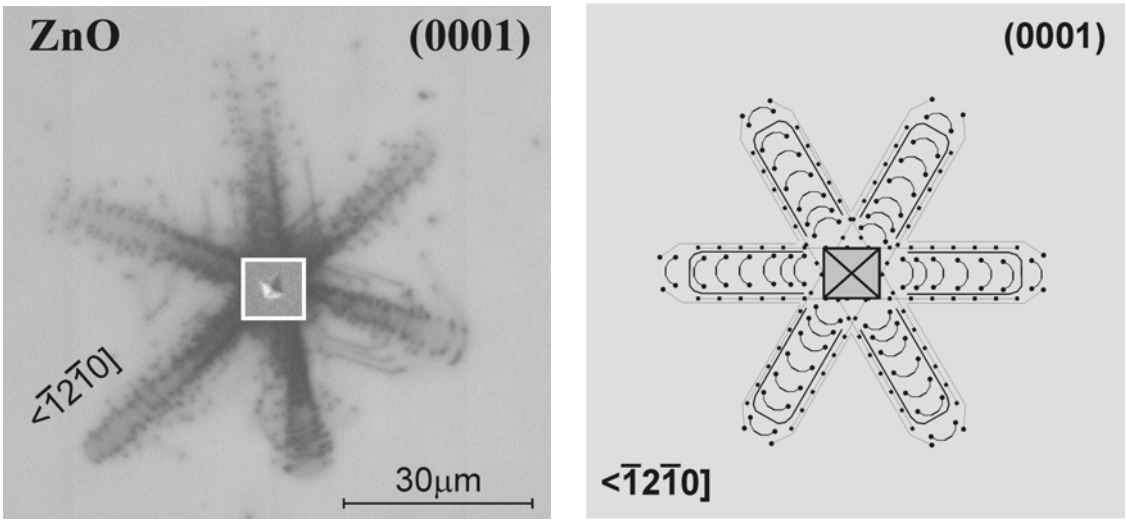

(a) (b)

Figure 46. Micro-indentation on (0001) ZnO. (a) SEM-CL micrograph. The SE image of indent is shown in the center. (b) Scheme of dislocation structures expected to be formed.

From the SEM-CL micrograph in Figure 46 (a), the six-arm dislocation rosette around the indentation center is concluded. Dislocations spread along double arms in $[\bar{1}2\bar{1}0]$ for distances of about 40 μm. The defect rosette constitutes of threading segments, surface parallel lines, surface parallel half- and quarter-loops as well as of lines and half-loops inclined to the surface.

A detailed inspection of the CL image in Figure 47 (a) revealed that surface-parallel half-loops break and transform into quarter-loops. Such a reaction is sketched and can be explained by the model shown in (b).

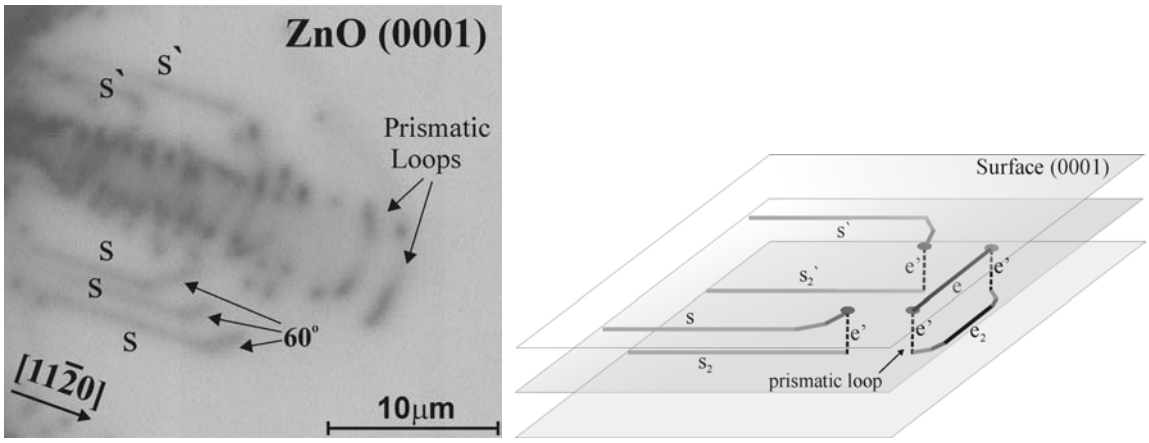

(a) (b)

Figure 47. (a) Reactions in basal half-loops involving a cross-slip events. (b) The model of possible reaction resulting in prismatic loop parts.

Local plastic deformation by means of micro-indentation on $(10\bar{1}0)$ sample surfaces of hexagonal prismatic crystal could be used to verify dislocation configurations containing, in particular, dislocations with polar core structure.

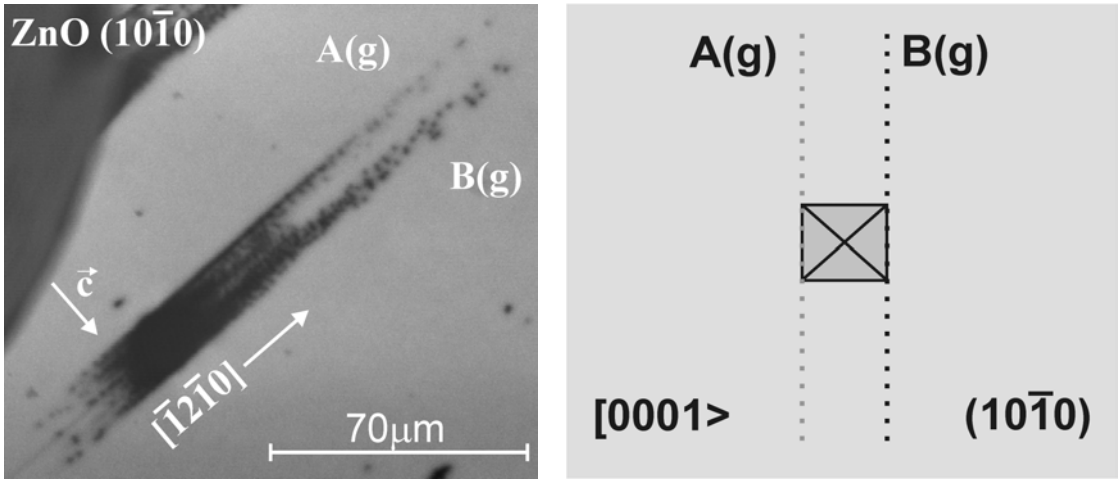

(a) (b)

Figure 48. (a) Typical double rosette arms in (10-10) plane. (b) Scheme of dislocation structures in (10-10) ZnO.

This $(10\bar{1}0)$ indentation produces two-fold dislocation rosettes pointing along the $[1\bar{2}10]$ directions. The CL picture of such dislocation arrangement is shown in Figure 48 (a). As sketched in Figure 48 (b) both rosette arms consist of two dislocation branches lying on opposite sides in respect to *c*-axis direction. No surface parallel dislocation arrangements are found. Thus, activation of basal plane slip systems must be concluded. Such kind of slip systems contains polar edge-type dislocations. Length of a rosette arm characterises dislocation mobility which should be different for the opposite polar edge-type dislocations.

Taking advantage of the special setup attached for in-situ plastic deformation, the formation of the dislocation-rosette could be followed up and documented by kinematical SEM-CL.

Figure 49 shows the CL picture chosen from the CL movie demonstrating building up of a rosette arm in the six-fold dislocation rosette around a indentation on (0001) ZnO.

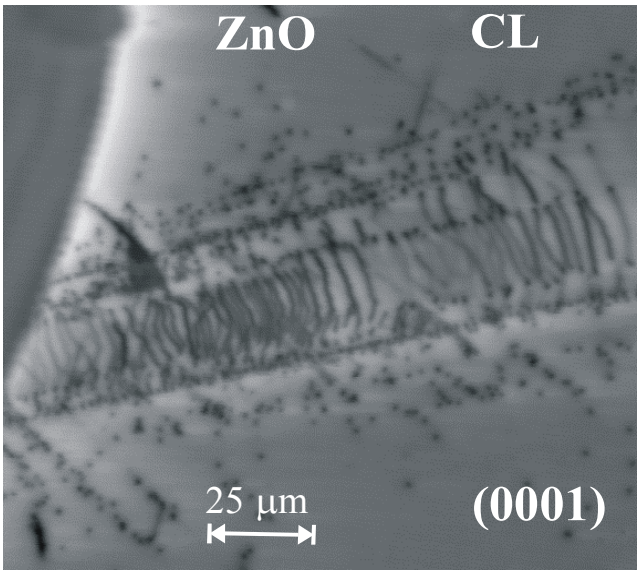

Figure 49. CL image of the defect configuration formed in <11-20> arm of six-fold dislocation rosette around an indent on (0001) ZnO sample. Basal and prismatic slip systems can be recognized from the defect arrangement utilizing the model for glide prism configurations proposed [see section 3.2.1].

The introduced dislocations exhibited high mobility and were propagated predominantly in surface-parallel basal and inclined or surface-perpendicular prismatic slip planes.

A closer look at the distribution of CL dark contrasts gives evidence for expansion of prismatic dislocation loops in a surface-parallel (0001) slip plane as part of the $<11\bar{2}0>$ glide prism proposed in section 3.2.1.

5.1.3 Identification of glide dislocation types

The dislocation configurations revealed by the results of the CL microscopy studies reflect major fundamental glide dislocation structures as predicted for the wurtzite lattice of ZnO crystals. The dislocation arrangements observed might be related to the basic slip systems expected. A clear evidence is given by the experimental findings for the operation of following glide systems:

- basal plane slip systems $\{0001\}<11\bar{2}0>$,
- prismatic plane slip systems $\{10\bar{1}0\}<11\bar{2}0>$.

There is no hint at any dislocations propagating in the other possible kinds of slip systems such as $\{10\bar{1}0\}<0001>, <\bar{1}100>$.

An example for the identification of dislocation type is given in Figure 50. The loop structure found in this CL image constituted from 58°, 90° and screw-type line segments. This kind of dislocation half-loop corresponds quite well to the group of glide dislocations shown in Figure 41 (b).

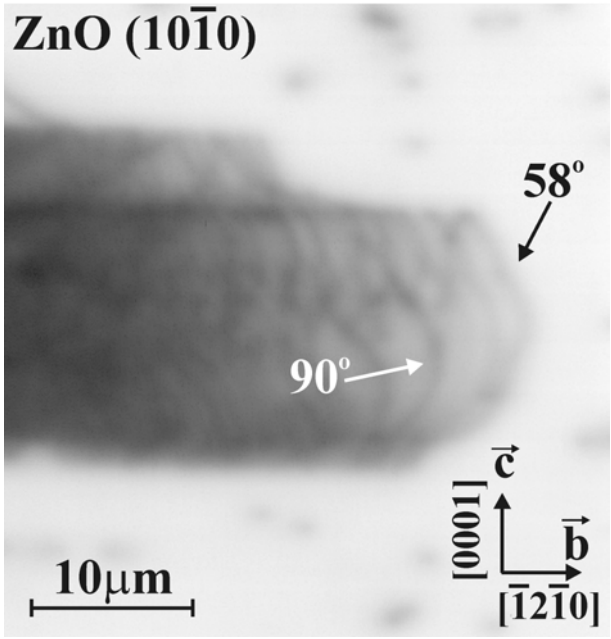

Figure 50. Grown-in glide dislocation loops parallel to (10-10) ZnO plane.

All observed glide dislocations should have an ***a***-type Burgers vector and differ in their particular core structures. Thus, from dislocation line directions determined in the microscopic defect arrangements as revealed in the CL images, the specific types of individual dislocation segments are obtained. Emergence of following dislocations is proposed:

Table 5-1.: List of types of glide dislocations identified.

Example in:	Slip system	Line direction ξ	Burgers vector $\boldsymbol{b}$	Description
Figure 49	$\{0001\}<\bar{1}2\bar{1}0>$	$<\bar{1}2\bar{1}\bar{3}>$,<0001> $<\bar{1}2\bar{1}0>$	$1/3<\bar{1}2\bar{1}0>$	QUARTER-LOOPS Edge-type: threading Screw: ξ‖surface
Figure 50	$\{10\bar{1}0\}<\bar{1}2\bar{1}0>$	$<\bar{1}2\bar{1}\bar{3}>$,<0001>,$<\bar{1}2\bar{1}0>$	$1/3<\bar{1}2\bar{1}0>$	HALF-LOOPS Edge-type, screw: ξ‖surface
Figure 49, 45	$\{0001\}<11\bar{2}0>$ $\{10\bar{1}0\}<11\bar{2}0>$	$<\bar{1}100>,<\bar{2}110>,<\bar{1}010>$ $<\bar{1}2\bar{1}\bar{3}>$,<0001>	$1/3<11\bar{2}0>$	PRISMATIC LOOPS Edge type: A(g)/B(g) loops Edge type: threading
Figure 41	$\{10\bar{1}0\}<11\bar{2}0>$ $\{0001\}<11\bar{2}0>$	$<\bar{1}2\bar{1}\bar{3}>$,<0001> $<\bar{1}100>,<\bar{2}110>,<\bar{1}010>$	$1/3<11\bar{2}0>$	PRISMATIC LOOPS Edge type: loops Edge type: A(g)/B(g) threading
Figure 55	$\{0001\}<\bar{1}2\bar{1}0>$	$<\bar{1}100>,<\bar{2}110>,<\bar{1}010>$, $<\bar{1}2\bar{1}0>$	$1/3<\bar{1}2\bar{1}0>$	HALF-LOOPS Edge-type: A(g)/B(g) ξ‖surface, Screw: ξ‖surface
Figure 48	$\{0001\}<\bar{1}2\bar{1}0>$	$<\bar{1}100>,<\bar{2}110>,<\bar{1}010>$, $<\bar{1}2\bar{1}0>$	$1/3<\bar{1}2\bar{1}0>$	QUARTER-LOOPS Edge-type: A(g)/B(g) threading Screw: ξ‖surface

5.2 Dislocation dynamics

Dislocation configurations developing during micro-deformation provide a straightforward access to study microscopic dislocation dynamics. Utilizing in-situ scratching and micro-indentation technique, progress of dislocation propagation can be recorded by means of kinematical SEM-CL. For the first time, it was possible to document motion and recombination activity of single dislocations in ZnO.

The results of in-situ scratching and micro-indentation experiments give clear evidence of high mobility and long-distance movement of the glide dislocations in basal as well as prismatic slip systems. Even at low temperatures down to 65K considerable dislocation slip up to some 100 μm per sec. is documented by SEM-CL movie. From this point of view, the crystalline ZnO appears to be a relatively soft material. Values of Vickers microhardness could be determined in range of $1.75 \cdot 10^9$Pa [mukh01].

5.2.1 Dislocation movement

Glide of dislocations is mobilized due to thermal activation. However, there is a remarkable response for the REDG effect, too. Figure 51 demonstrates thermally induced expansion of the dislocation rosette around an indent produced on the (0001) surface at low temperature.

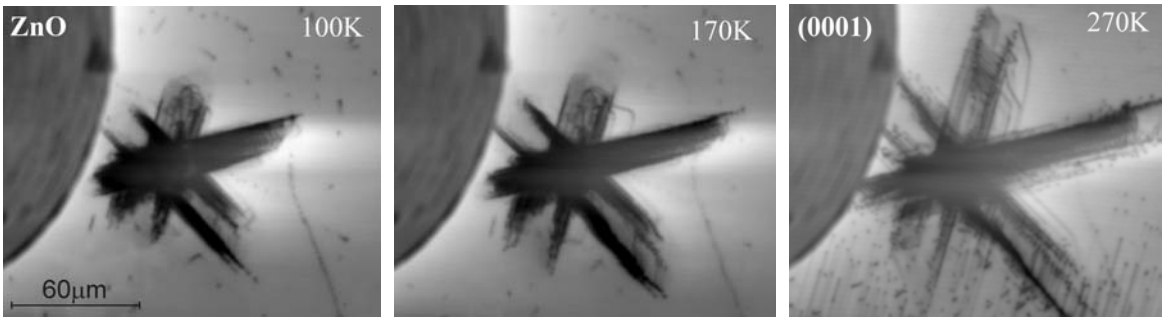

(a) (b) (c)

Figure 51. Expansion of a dislocation rosette in the stress field gradient of indent on (0001) ZnO upon heating. (a) 100K, (b) 170K, (c) 270K.

Heating up the sample caused dislocation propagation in the stress gradient occurring because of the indent in the rosette center. Lengths of the rosettes arms increased while raising the temperature. Expansion of single dislocation loop structures as well as motion of threading dislocations can be recognised.

Individual threading dislocations emerging from basal slip systems on a $(10\bar{1}0)$ sample surface are shown in Figure 52 as moving due to REDG effect. These dislocations were introduced by scratching on $(10\bar{1}0)$. Anti-parallel slip occurs in the almost identical strain field area close to a scratch. This anti-parallel slip motion originates probably in different sign of the Burgers vectors belonging to the dislocations under consideration. Such a difference in the Burgers vectors might also explain some processes of simultaneous occurrence of dislocation formation and backformation in same sample area [schr04].

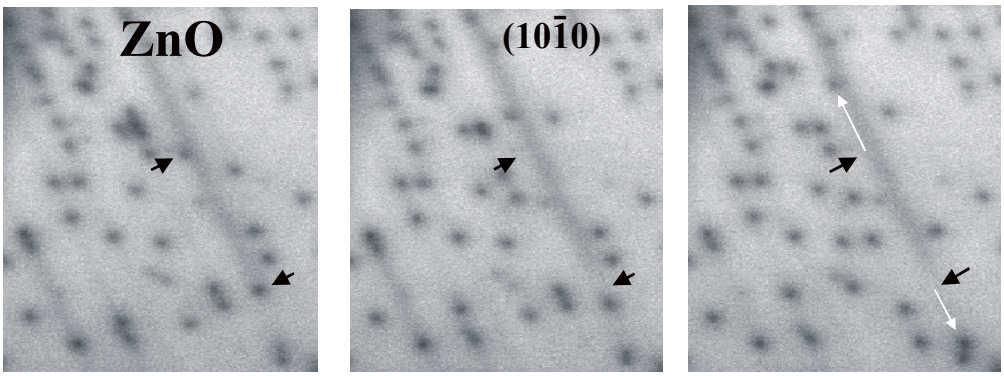

t_0 t_n t_x

Figure 52. Series of CL images illustrates anti-parallel slip motion of threading dislocation segments observed on (10-10) ZnO sample and gliding in (0001) slip plane at 259K. Order on time scale: $t_0 < t_n < t_x$.

Grown-in dislocations (see Figure 42) are found to be immobile; they showed no tendency to move neither for thermal activation nor under REDG conditions.

The further studies performed have disclosed interesting particularities of the microscopic dislocation dynamics in ZnO. In Figure 53 beside events of anti-parallel slip and formation or backformation of dislocation parts in same strain field are displayed, respectively.

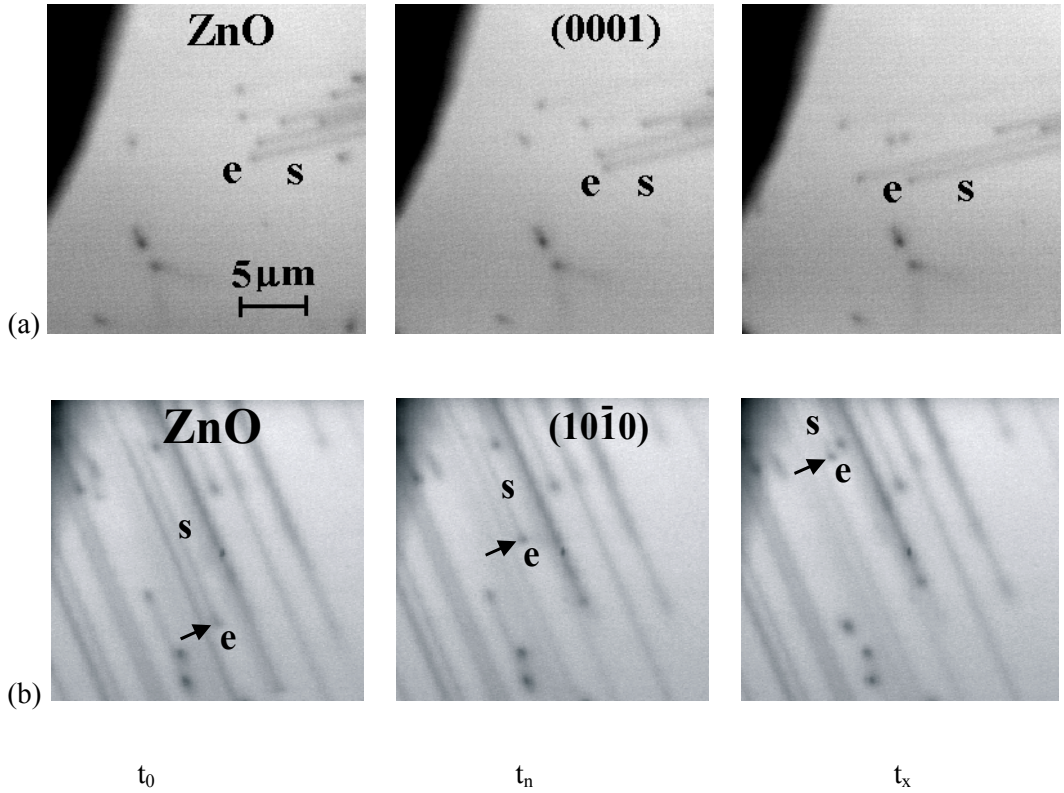

Figure 53. Microscopical dynamic behaviour of single dislocations as revealed by kinematical SEM-CL at 72K. In CL series the formation (a) and backformation (b) of surface-parallel screw-type defect line parts (s) accompanied with mobile threading dislocation segments (e) are documented. Lengths of line segments pulled out or removed are in the order of some µm. Order on time scale: $t_0 < t_n < t_x$

Figure 53 (a) and (b) are about the formation and backformation of surface-parallel line segments (s) accompanying threading dislocation segments (e) moving near a scratch placed on a (0001) (Figure 53 (a)) or (10$\bar{1}$0) (Figure 53 (b)) surface, respectively. In case of Figure 53 (a) the threading segment is pulling out a surface-parallel defect line, which has seemingly screw-type character. In series of Figure 53 (b) the local dislocation configuration marked by (s) and (e) shrinks mainly due to disappearance of the surface-parallel screw line part (s). This defect reaction may be regarded as an elementary step of the recovery process if local stress is removed.

In Figure 54 (a) the arrangement of surface-parallel dislocation loop parts is shown. The screw-type segment (s) disappears by assumed cross slip event and subsequent backformation of the remaining defect line portion (Figure 54 (b)). The sketched models (Figure 54 (c-d)) illustrate this reaction. The threading segments (e`,e`) formed more apart, and backformation takes place for screw segment (s).

Revealing the mobile dislocations as recombination centres by means of kinematical SEM-CL microscopy proves their intrinsic electronic properties.

Distinct type-dependent dynamic behaviour may be expected to be recognisable at separate dislocation segments exhibiting screw- and edge-type structures. The CL micrograph in Figure 55 contains several CL contrasts of dislocation half-loops (s-e-s) expanding preferably in the $<11\bar{2}0>$ crystallographic direction of the arm of a dislocation rosette investigated on the (0001) surface of a ZnO sample.

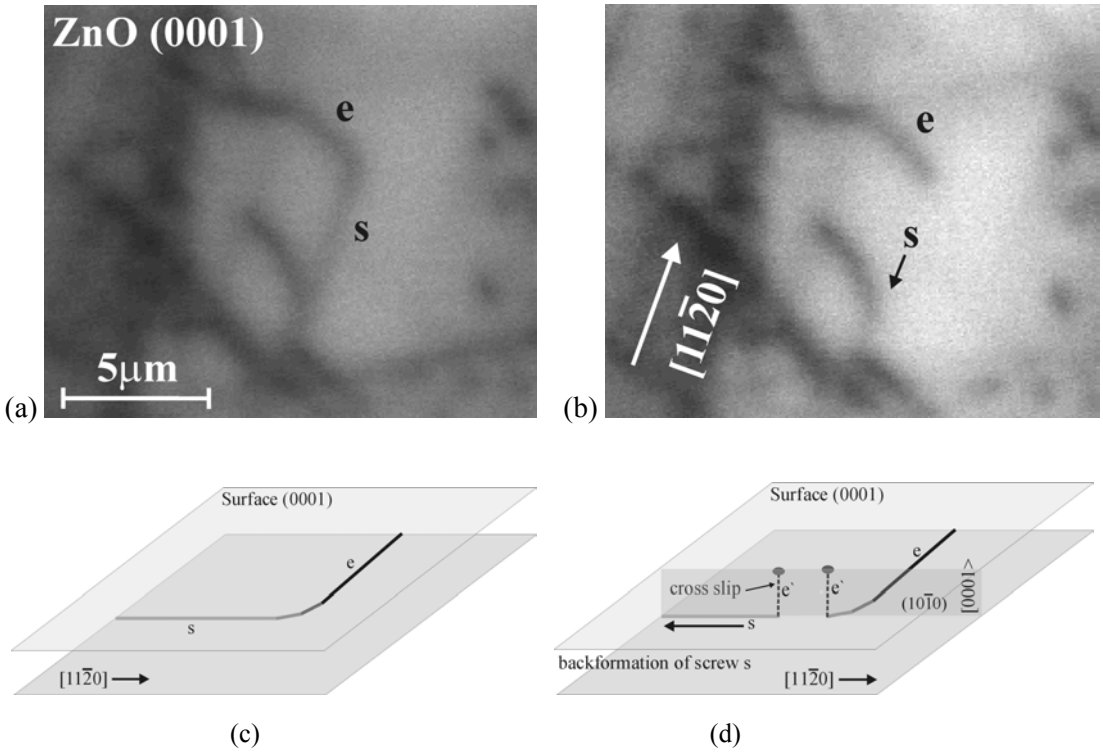

Figure 54. Selected frames of entire SEM-CL movie containing backformation of a screw dislocation segment by means of the cross-slip (a, b) in ZnO (0001) and corresponding possible models (c, d).

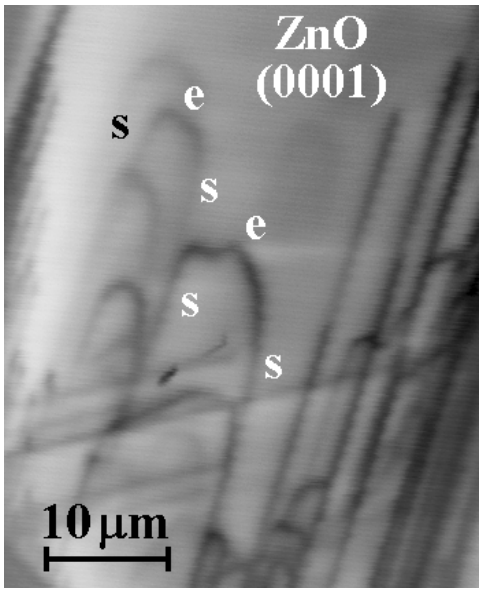

Figure 55. CL micrograph showing propagation of dislocation half-loops (s-e-s) expanding preferably in <11-20> direction by basal plane slip. (e) and (s) label edge- and screw-type segments, respectively. Stronger CL contrast for edge-type parts is clearly seen.

The asymmetric expansion of the loop structures hints at different mobilities for the edge- and screw-type dislocation segments. The faster loop parts may be identified as the edge-type segments having B(g) character as can be deduced from the polar termination of the (0001) sample surface. The edge-type segments obviously show stronger CL contrasts if compared to the contrast values observed at the screw line segments.

5.3 Quantitative analysis of dynamics and CL contrast of dislocations

5.3.1 Dislocations as recombination centers in ZnO

SEM-CL imaging of dislocations gives direct evidence of dislocations electrical activity by proving defect-induced carrier recombination reflected by the CL defect contrast. All dislocations dealt with so far, may be regarded as non-radiative recombination centres. It is worth mentioning, that kinematical SEM-CL technique employed to carry out studies on dislocation dynamics allowed at the same time in the same way to establish the dislocations as extended mobile recombination centres having electronic properties of intrinsic nature. Studying the CL contrast behaviour at the dislocations yields essential information about the dislocation-bound carrier recombination processes. In case of the non-radiative carrier processes a detailed analysis of the acquired CL contrast data may be used to gain specific recombination kinetic defect parameters as described in the framework of the SCBSRH model mentioned above [see 3.6.2].

Present investigations were intended to disclose a distinct type-dependent electrical activity of the glide dislocations verified in the ZnO samples.

5.3.1.1 Quantitative analysis of CL contrasts of individual single dislocations

In order to quantify CL defect contrasts as displayed in the CL micrographs following convention is commonly used to define a value of CL contrast [schr89b]:

$$C_{CL} = \frac{(I_D - I_0)}{I_0} . \qquad (70)$$

Here, I_D and I_0 mean CL intensity as measured at the dislocation and in undisturbed matrix, respectively. CL contrast values are usually gained by means of one-dimensional CL intensity profile measurements.

Improvement in CL contrast determination is achieved by recording quantitative CL maps containing the defect contrast pattern.

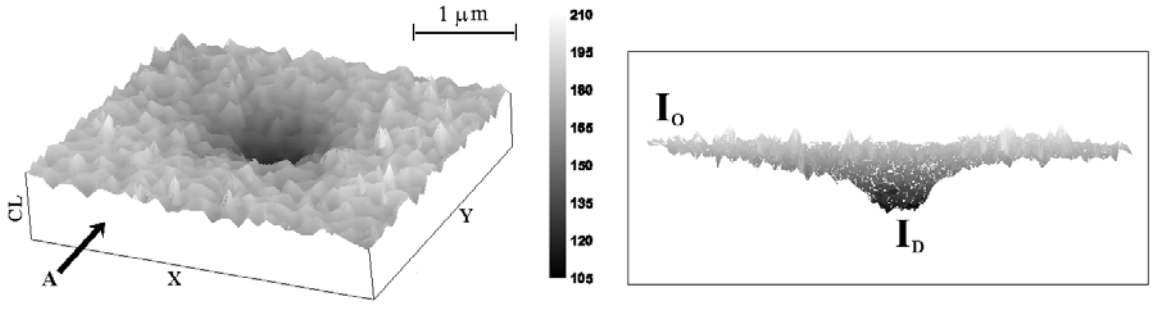

(a) (b)

Figure 56. 3D presentation of map of CL intensity at threading dislocation segment in ZnO sample by top view (a) and A-side view (b) showing local defect-related and matrix intensity levels.

Figure 56 (a) is a 3D plot of a quantitative CL map showing the CL defect contrast spot of a threading dislocation segment. A lateral decrease of the CL signal in the vicinity of the defect is clearly displayed. In Figure 56 (b), the same local reduction of CL intensity is revealed in a side view appropriate for extracting the matrix (I_0) and defect related (I_D) CL intensity values.

In case of surface-parallel dislocation configurations, the defects are imaged as line-like CL patterns such as demonstrated in Figure 57 (a). Local CL contrast behaviour as well as the change of the contrast value along the defect line under consideration can be revealed.

A new procedure for the CL contrast analysis along dislocation lines has been developed [vas04]. This procedure is explained in Figure 57 (b) as applied to the CL contrast pattern of a part of a dislocation half-loop expanding in the surface-parallel slip plane.

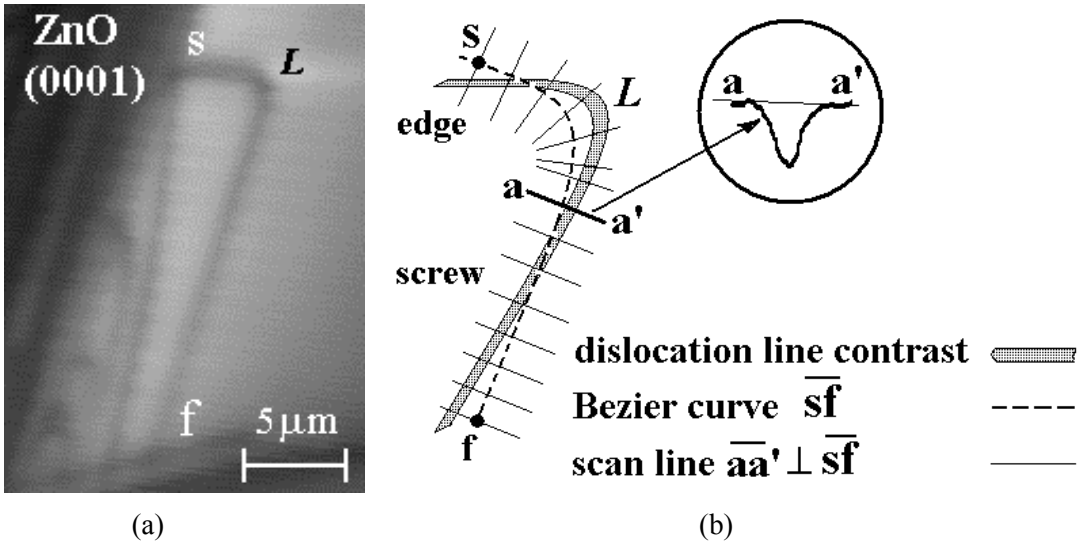

(a) (b)

Figure 57. Procedure of Bezier curve guided analysis of CL contrast along dislocation loop structure (**sf)** shown in the CL image (a). Procedure of local CL contrast profile measurement is sketched in (b).

Change of CL contrast strength is recognized over this loop structure between s and f. The advanced CL profile analysis for a dislocation line includes following steps. First, a set of CL intensity profiles aa' crossing perpendicularly the dislocation loop line is taken between the start point "s" and the finish point "f". The local CL profiles are generated by means of Bezier curve [far83] guidance as illustrated by the scheme given in Figure 57 (b). Such guided measuring procedure provides a number of CL intensity profiles, which are to be analysed in a second step in order to evaluate the local CL contrast values. The result obtained is the CL contrast value in dependence on distinct site along the dislocation line. The advantage of this multiple contrast analysis procedure is a reliable comparison of the CL contrast behaviour over neighboured dislocation segments that may differ in type. Figure 57 illustrates a typical case of edge and screw part arrangement in a dislocation loop.

5.3.1.2 CL contrast behaviour depending on dislocation type

Quantitative CL contrast studies have been carried out based on the verification of dislocation configurations containing individual glide dislocations varying in structural type. The chosen dislocation arrangements must be accessible for SEM-CL mapping under conditions fulfilling the requirements of quantitative CL contrast analysis.

The glide dislocations considered so far, were identified as screw- and edge-type dislocations with the same kind of Burgers vector parallel to $<11\bar{2}0>$, but differing in the core structure. As shown in Table 3-6, there is a clear distinction between edge-type dislocations having polar or non-polar core structures in relation to the type of slip system they belong to. The polar core structures

are found in the basal plane slip system, and the non-polar core structures occur in prismatic slip systems.

A quantitative inspection of the CL contrast values at dislocations has been made by comparing the contrast behaviour at individual dislocation segments which exhibit similar defect geometry, i.e. threading position or situation in identical surface-parallel glide plane. The latter case is realised for a surface-parallel loop structure. In these cases, measured contrast ratios may be equated with the ratios of the defect recombination activities.

All types of dislocations formed in both the basal and prismatic plane slip systems are found to show non-radiative recombination activity. However, no dislocation arrangement suitable for a reliable comparison of the recombination activity between single dislocations in basal and prismatic slip systems could be realised.

Restricting to basal plane slip systems, the main attention in the experiments was focussed on quantitative examinations of the CL contrast behaviour of screw and various edge-type dislocation segments built in an identical slip plane. Furthermore, special emphasize was on the disclosure of expected differences in the recombination activity of the polar A(g)- and B(g)-type dislocation structures that appear in threading geometry on $(10\bar{1}0)$ sample surfaces.

Figure 58 shows the result of the Bezier-curve-assisted contrast analysis along the dislocation loop structure found in the CL image of Figure 57 (a). The analysis procedure includes the well-developed edge- and screw-type parts forming the defect configuration.

A distinct recombination activity is likely indicated by the different contrast strengths observed at the screw- and edge-type dislocation segments situated in the same surface-parallel glide plane.

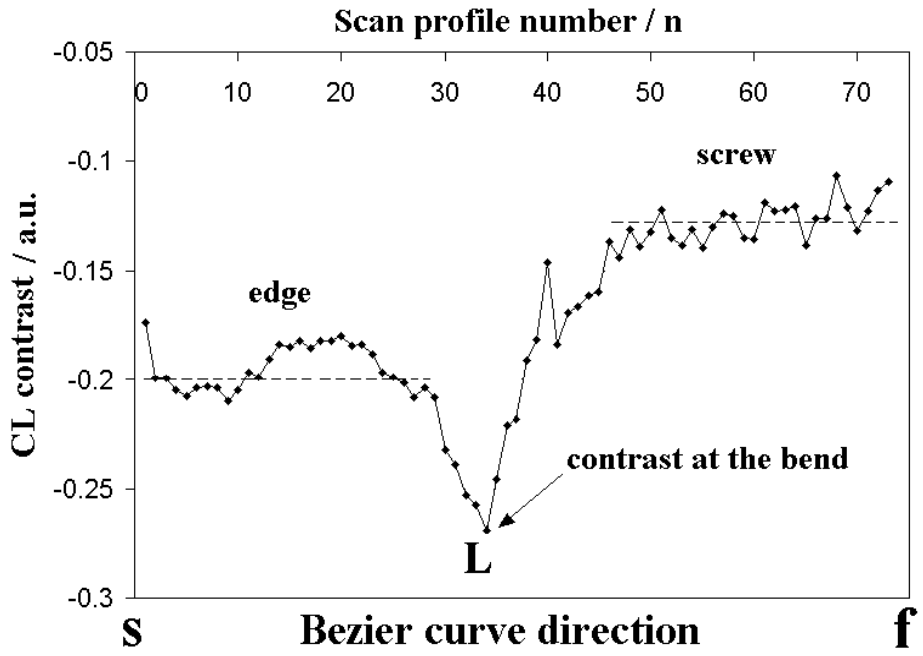

Figure 58. Behaviour of CL contrast at a dislocation half-loop propagating in a surface-parallel basal slip plane. Variation of CL contrast along the dislocation **sf** is revealed. Edge- and screw- type segments are found to exhibit different contrast strengths. Additional enhancement of CL contrast in the bend region L is seen.

The CL contrast values measured on the edge-type dislocation segment are found to be clearly increased in comparison with those ones of the screw part. Thus, enhanced recombination activity for the edge-type segment can be concluded. A characteristic contrast ratio C_e / C_s of about 1.4 is found. At the sharply bent part of the loop line, an additional rise of contrast is observed. This phenomenon might be explained by regarding kinks as effective carrier recombination centres. Their density could be increased in the corner region for geometrical reasons [see section 3.4.1].

Figure 59 presents a second example of CL contrast analysis at a dislocation loop structure. The result obtained clearly confirms different recombination strength for the edge- and screw-type dislocation segments in the basal plane slip systems.

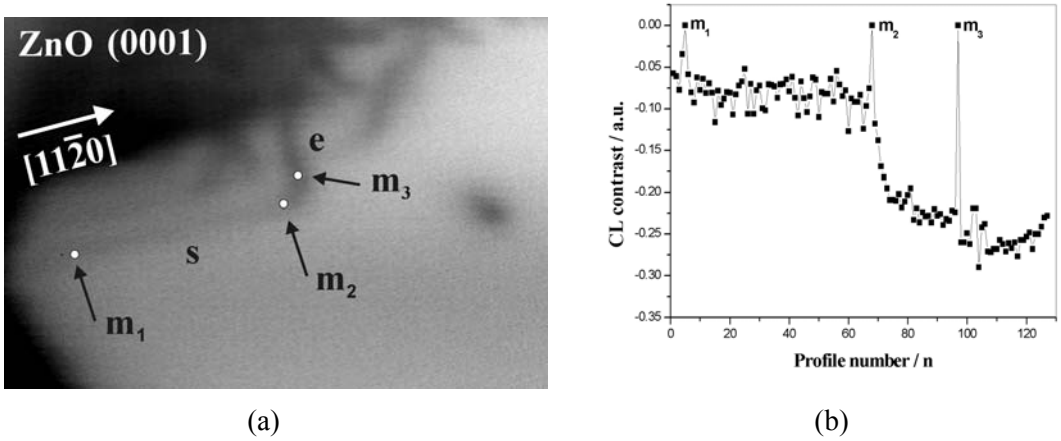

(a) (b)

Figure 59. Result of advanced analysis of CL profile measurement at basal dislocation half-loop containing screw and edge-type segments. (a) CL micrograph of expanding dislocation loop structure in ZnO (0001). (b) CL contrast for the different dislocation segments. Markers m_1, m_2, m_3 have been given for clear localization of profile measurements.

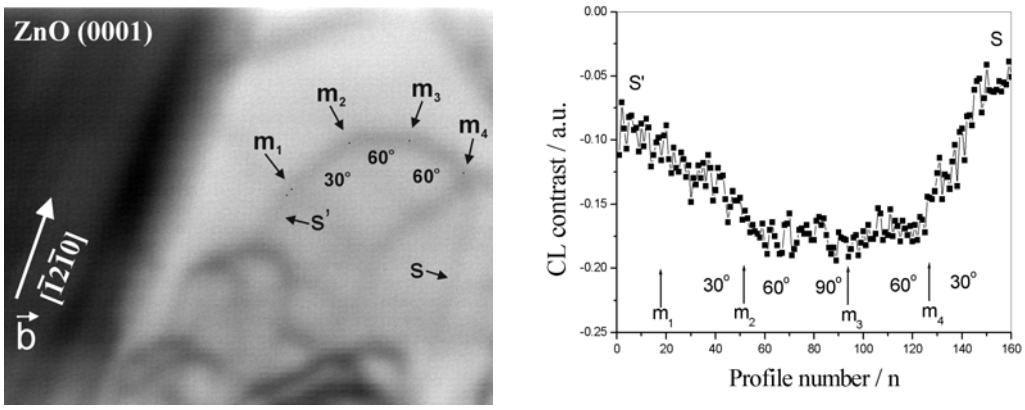

(a) (b)

Figure 60. Utilize of CL profile analysis to a propagation dislocation half loop (a). Advanced profile analysis (b).

Figure 60 (a) is the CL picture of dislocation half loops as propagated in a basal glide plane along the $[\bar{1}2\bar{1}0]$ direction. The remarkable feature of the CL micrograph is that the half-loop contains among others a well discernible 60°-type segment. The 30°- and screw-type segments may easily be recognised. The set of arrow markers (m_1… m_4) was putted in order to establish correspondence between the measured contrast profiles and real positions in the image. The angle

measurements performed for the line segments have shown that there occurs only a very short 90° segment. The maximum CL contrast is found to be located in between two 60°-segments. This could point at the fact that the 90°-type segment present possesses considerable strong recombination activity. Thus, a relationship of the contrast behaviour can be concluded as follows:

$$c_{90^\circ} \geq c_{60^\circ} \geq c_{30^\circ} \geq c_{screw} .$$

The smoothly curved shape of the dislocation line might indicate existence of geometrical kinks that might affect the contrast behaviour along the dislocation bent.

The behaviour of CL contrast found for its dependence on type of the dislocation segments in the loop structure of Figure 60 qualitatively agrees with the tendency predicted by the consideration in section 3.2.2, in respect to the electrical activity of a glide dislocation loop as expected in the framework of the dangling bond model.

5.3.1.3 Revealing of dislocation reactions and CL contrast behaviour

Particular CL contrast behaviour characterising complex recombination activity must be taken into account for defect reactions such as dislocation- dislocation interaction.

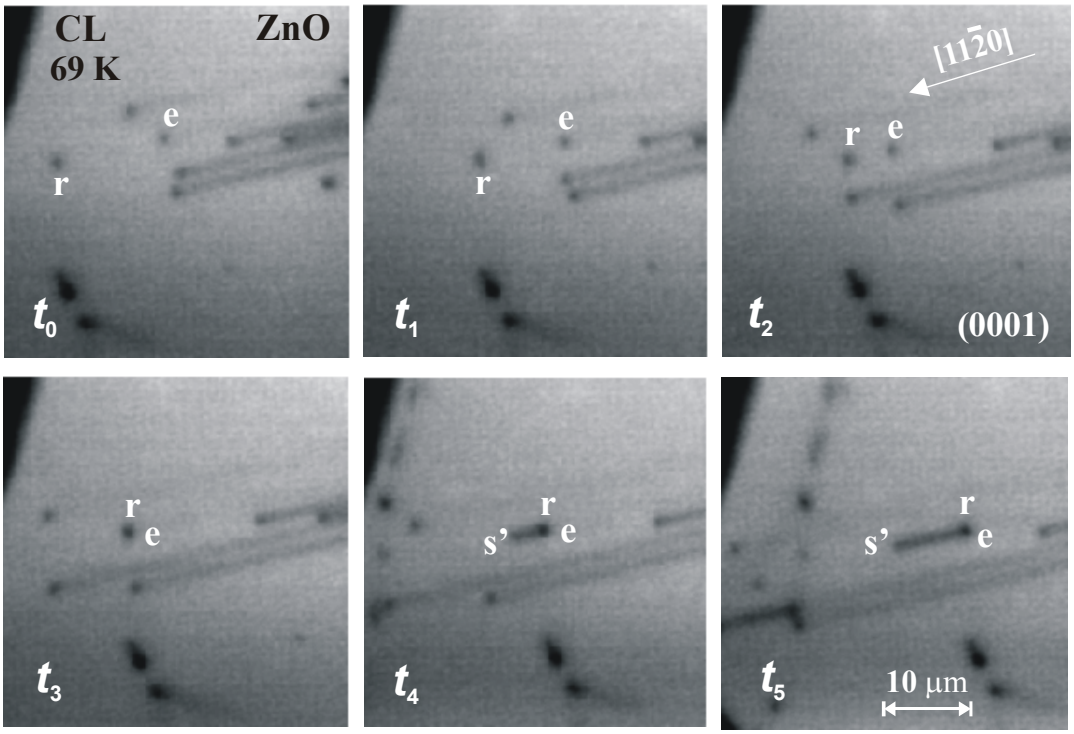

Figure 61. Motion (REDG) of edge-type threading dislocations with or without corresponding surface-parallel screw parts in prismatic slip planes. Running time between t_0 and t_5 is about 10 sec. Reaction can be seen between sessile defect (r) and moving dislocation (e) resulting in expansion of defect line (s´).

Figure 61 presents a sequence of images chosen from the CL movie, which was taken to record travelling threading dislocations. Most of them have been found dragging a screw part along. The latter is pictured by a straight contrast line, whereas the related threading segment, appears as a spot of stronger dark contrast. There is defect reaction between a sessile and a slipping threading dislocation resulting in a new screw part growing along the direction of glide.

As the mobile dislocation segment (e) approaches the sessile defect (r), hence it becomes pinned, and as a consequence of this dislocation-dislocation interaction, a surface-parallel line defect configuration (s') is formed and pulled out.

5.3.2 Correlated analysis of dynamics and CL contrast properties by means of DCD method

5.3.2.1 Introduction to DCD method

Utilization of kinematical CL microscopy renders it possible to consider single dislocation dynamics on microscopic scale. For this purpose, velocity measurements at individual dislocation segment have to be realised. A unique method for quantitative analysis of the dynamic dislocation properties has been developed, which may be applied to reveal the CL contrast behaviour of moving dislocation as well. Using the procedure described in the following, the behaviour of gliding dislocations i.e. the momentary speed and dynamic CL contrast value can be deduced from the CL video movies.

Analysis of single dislocation dynamics has been used very successful in case of GaAs studies, and shall be presented again to demonstrate the methodological steps [vas04]. Starting with splitting of the CL movie into single frames provides a series of subsequent CL images that display changes of the dislocation configurations as a function of time. Example is given in Figure 62 (a).

The shown sequence nicely illustrates expansion of several surface-parallel dislocation loop structures. For registering the movement of a line segment belonging to dislocation D_1, CL intensity profiles are created along the arbitrarily chosen line **AB** that is fixed in the identical image area for all frames of the entire image sequence forming the given movie.

Distinct positioning of the recording line allows to record the motion of any particular dislocation segment (Figure 63).

To analyse the dislocation slip path as a function of time, the CL intensity profiles over the recording line **AB** must be measured in all subsequent frames of the given movie. The resulting CL profiles are finally arranged in a special kind of diagram, the so-called Dynamic Contrast Diagram (DCD) [vas04]. The DCD plots (Figure 62 (c,d)) present slip path and momentary value of CL contrast at the dislocation site crossed by the recording line **AB** versus the frame numbers that correspond to time scale. On the other hand, the DCD displays the progress of a CL intensity profile measured between points A and B in each frame against the time. The local dislocation velocity can be derived from slope of the DCD pattern formed by the CL contrast peak of moving defect.

Generation of the DCD plots is a very useful way to discover the dynamics of slip dislocations. The DCD plot in Figure 62 (d) contains information on the glide motion for up to 5 different dislocation segments ($D_1 \ldots D_5$). Anti-parallel slip and change of velocities are clearly revealed.

The dynamic CL contrast behaviour of edge- and screw-type dislocation segments in GaAs is demonstrated in Figure 62(a-d). Both edge- and screw-type parts appear as dark CL contrasts. Movement of fresh glide dislocations in various $\{111\}<1\bar{1}0>$-type slip systems as observed on the (111) oriented sample is illustrated by the sequence of CL images shown in Figure 62 (a). The dislocations introduced by ex-situ scratching propagate in strain gradient and move under electron beam excitation due to REDG effect at room temperature [mae00].

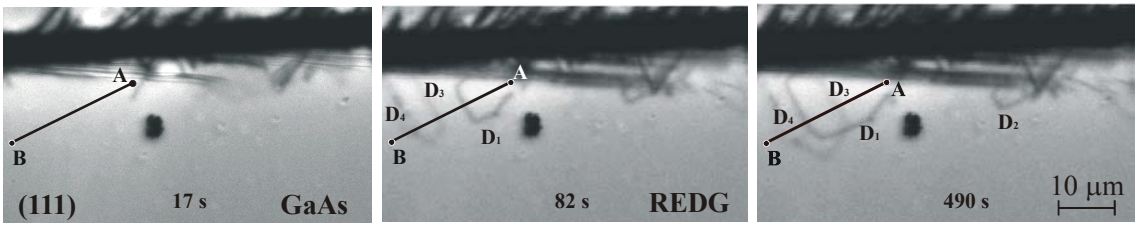

(a)

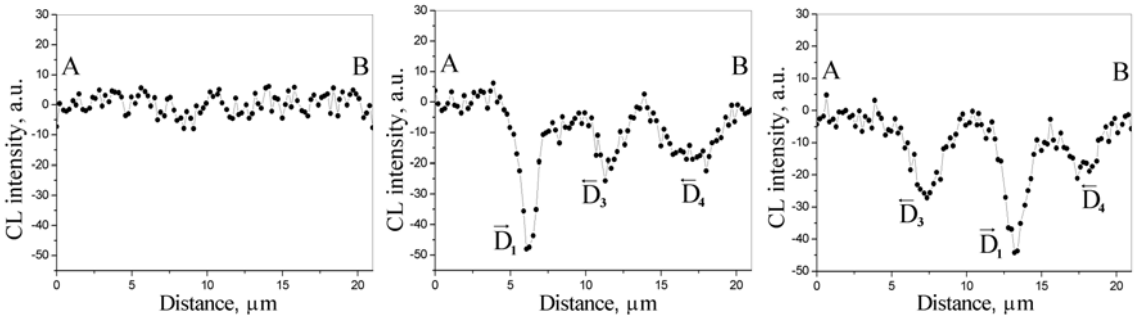

(b)

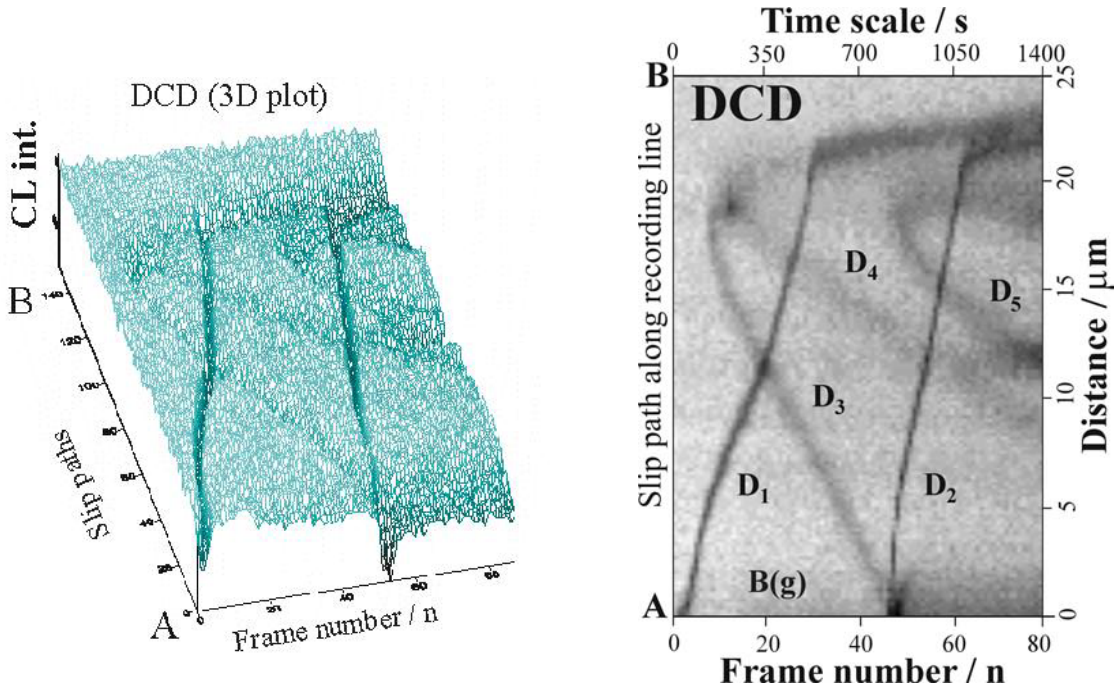

(c) (d)

Figure 62. Analysis of dynamics and correlated CL contrast properties as observed by means of kinematical SEM-CL at individual glide dislocations. Sequence of CL images (a) selected from CL movie displays propagation of dislocation segments (D_1,D_2,…) constituting an expanding half-loop structure. Examples of CL intensity profiles along **AB** crossing particular mobile parts of half loops are given in (b). Corresponding DCD plots (c, d) represent complete set of the CL intensity profiles transformed into 3D or gray scale presentation, and put together over the frame number axis which relates to time scale. The DCD plots provide data on slip motion and momentary CL contrast behaviour for up to 5 different dislocation segments. The DCD plots given for dynamics of surface-parallel line segments moving by REDG in strain field of scratch on (111) GaAs.

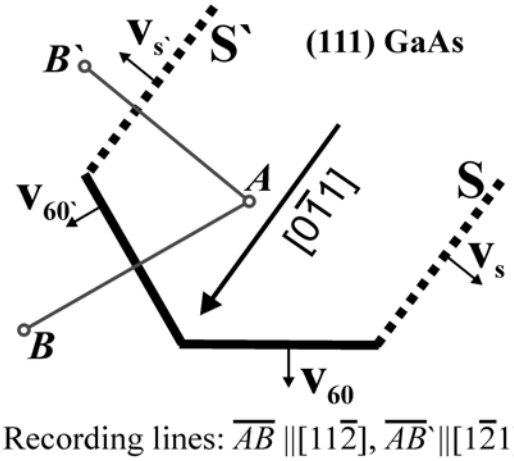

Figure 63. Particular 60° or screw segment of a dislocation half-loop is chosen for DCD analysis by positioning the recording lines **AB** and **AB`**.

Studying the (111) sample configuration allows for recognition of isolated individual dislocation half loops expanding in surface-parallel glide planes, so that occurring edge-type (30°, 60°, 90°) and screw line parts belonging to same dislocation loop structure can be investigated in detail. In Figure 62, complete CL contrast analysis is performed for a 60°-line segment D_1. Examples of extracted CL intensity profiles according to the recording line **AB** fixed are shown in Figure 62 (b).

The qualitative interpretation of a DCD is easy to perform only in the case if the scan line chosen runs perpendicular to the dislocation segment under consideration. Otherwise, the interpretation is more difficult and, thus, simultaneous consideration of the original CL movie is necessary. Quantitative treatment of CL intensity profiles includes preliminary noise filtering and local background correction followed by a computation of the values of CL defect contrasts. In particular, specific DCD plots can be created from the same CL movie for analysing several distinct segments along an individual dislocation line structure. In order to perform analyse of as derived DCD the original algorithm has been developed which includes following steps:

1) Manual choosing (through the mouse click) of the pattern related to a distinct dislocation segment and its subsequent automatic tracking.
2) Automotive extraction of frame number, position of a CL defect contrast peak and its magnitude directly from the given DCD.
3) Storage of as extracted data in an ASCII file.

The new DCD technique was successfully applied to examine the dynamic CL contrast behaviour of edge- and screw-type dislocation segments in GaAs as demonstrated in Figure 62 (a-d).

The DCD plot gives basic information about the fundamental dynamics of single dislocations. Figure 64 is about the dynamic behaviour of two threading dislocations spots travelling in closely spaced glide planes of same $\{111\}<1\bar{1}0>$ slip systems. The DCD patterns show different modes of motion, namely, acceleration for D^* and deceleration of D, respectively. This different behaviour is rather surprising since both defects are situated in a common stress field related to the scratch as can be seen in Figure 64. Thus, additional local driving forces must be taken into consideration.

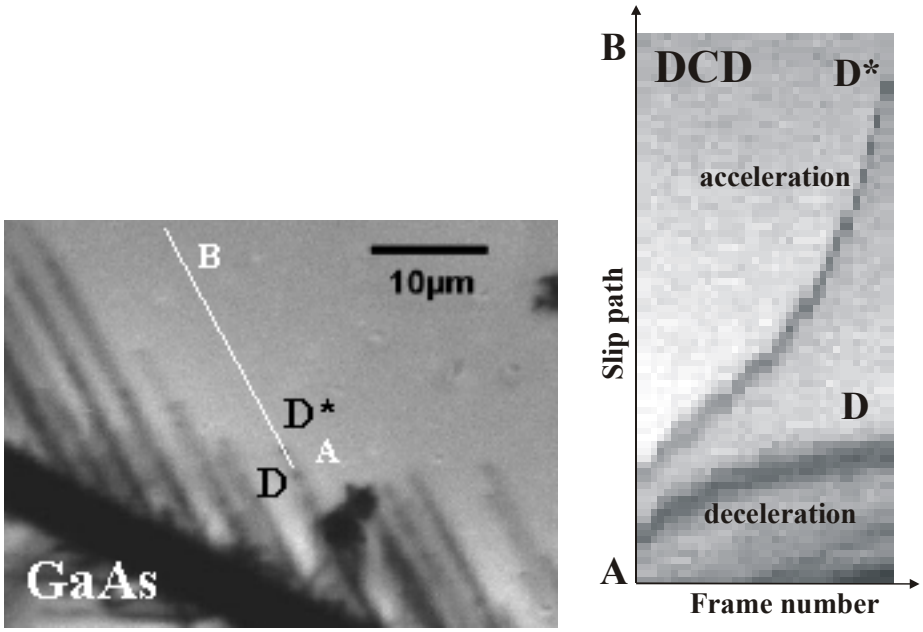

(a) (b)

Figure 64. Dynamics of neighbored single threading dislocations moving in a similar slip system of GaAs as illustrated in CL micrograph (a). DCD plot (b) proves acceleration for defect D* and deceleration for dislocation D. Entire time scale: 8s.

A similar dynamic behaviour can be evidenced for the dislocations in ZnO. Accelerated movement of a single dislocation in the glide plane of a prismatic slip system is documented in Figure 65 (a-c). Figure 65 (c) is the velocity diagram showing variation of slip speed.

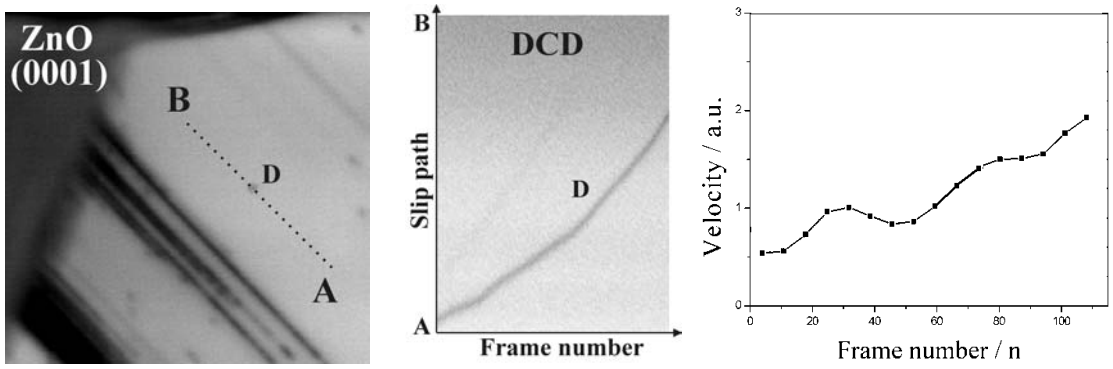

(a) (b) (c)

Figure 65. Dynamics and CL contrast behaviour of threading dislocation segment in ZnO. (a, b) show CL micrograph and derived DCD plot, respectively, for a mobile threading dislocation D. Analysis of the DCD yields local velocity as plotted in (c).

To get a better understanding of a possible relationship between defect dynamics and intrinsic recombination activity, more detailed considerations of the REDG effect at individual dislocation appears to be rather useful. Such an experiment employing kinematical SEM-CL to observe the REDG properties of a single dislocation is dealt with in Figure 66 (a-c).

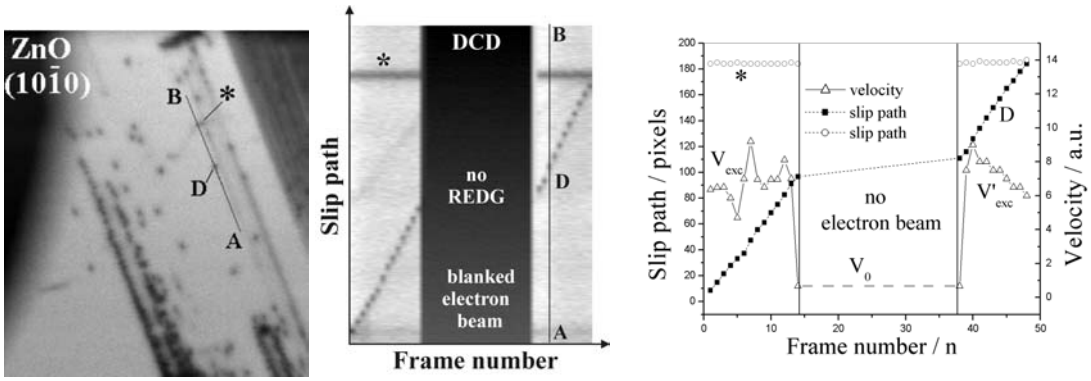

(a) (b) (c)

Figure 66. Recognition of REDG effect for dislocation slip by a {10-10}<11-20> glide system in ZnO. Movement of a threading dislocation segment under condition with and without electron beam excitation is followed by observing the CL contrast spot D shown in CL image (a). Corresponding DCD plot is given in (b). Slip velocities determined for REDG phases and the period of pure thermally activated glide are displayed in (c), enhancement factor of ~12 is derived.

Figure 66 (a) is a frame taken from the entire movie documenting the REDG-related movement of threading dislocation spot marked D. The DCD plot in Figure 66 (b) contains the pattern of the mobile defect D and of a resting defect marked as "*". Dark area in the DCD corresponds to beam-off state.

Under electron beam excitation, the threading dislocation D has comparable velocity before and after the beam-off period. During the time, when the electron beam was blanked, slow dislocation glide remains. Under this condition, dislocation motion is only due to thermal activation and local stress. For the threading dislocation observed here the velocity ratio is found to be:

$$V_{exc}/V_0 \approx 12$$

Motion of the dislocation under electron beam irradiation and its essential decrease in excitation pause prove clear REDG effect in the ZnO sample [mae00] and hint at stimulation of kink processes by the dislocation induced carrier recombination [mae83].

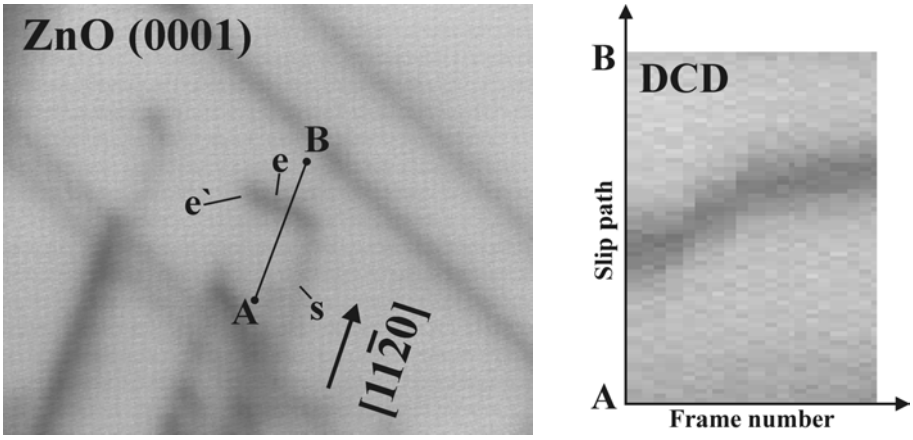

(a) (b)

Figure 67. (a) A frame from an entire movie with gliding edge-type dislocation segment in basal slip plane. Scan line **AB** was positioned as shown in the picture. (b) Corresponding DCD plot as acquired for segment (e) shows deceleration.

REDG-induced movement of dislocation loop configurations have been recognised, too. In Figure 67, a loop-like dislocation structure (e'-e-s) can be found, where the edge parts (e, e') slipped along **AB** in surface-parallel glide plane of a basal slip system (e) and in a surface-perpendicular plane of prismatic slip system (e'). The screw part (s) appears to be immobile possibly due to confinement by a prismatic slip plane that may give rise to cross slip events.

Figure 67 (b) is the slip path diagram derived for the dislocation line segment (e) possessing two distinct velocity ranges.

5.4 Evaluation of dynamic CL contrast behaviour of moving dislocations

The technique of kinematical SEM-CL which reveals glide dislocations as extended mobile recombination centres was exploited to evaluate CL contrast behaviour at the moving defects. The dynamic CL contrast properties directly relate to dislocation-bound carrier recombination during the glide process. Evaluation of the dynamic CL contrast behaviour appears to be appropriate for proving differences of electrical activity resulting from alteration of internal dislocation structure if the defect turns from resting state to slip motion. Obviously, variation of kink density may play a distinct role.

Creation of the DCD graph followed by extraction of local contrast values and corresponding velocity for a single dislocation segment under consideration have been used to realize any relationship between dislocation dynamic and recombination activity.

Before presenting detailed results concerning expected contrast-velocity correlation an example of clear impact of dynamics-related structural changes of dislocation configuration on the CL contrast behaviour shall be considered.

Figure 68 shows the DCD plot generated for the dislocation-dislocation interaction described above in Figure 61.

The insets image the dislocation arrangement before and after collision of the slipping dislocation segment (e) with the resting defect (r). This defect reaction can be followed up in the DCD plot given. The patterns of the mobile and sessile defects before and after interaction are figured. The formed defect complex (r+e) shows enhanced CL contrast resulting obviously from a superposition of contrast contributions of the individual defects (r) and (e). The pulled-out defect structure (s') constitutes of two parallel screw-type line segments making up a dipole structure. Its contrast behaviour is reflected by the slightly darker area in between the patterns (r+e) and (s').

The results given in Figure 69 are about the dynamic CL contrast behaviour of a threading dislocation segment moving in ZnO (0001). The dislocation slips on prismatic glide plane under interrupted REDG condition. During beam-off period the dislocation may possibly getter impurities from the matrix, causing a change of CL contrast. In this experiment here the dislocation did not succeed to attract a remarkable amount of impurities to affect the contrast value.

The dynamic CL contrast values determined show slight decrease with slip path that contradicts any formation of dislocation decoration at the moving defect.

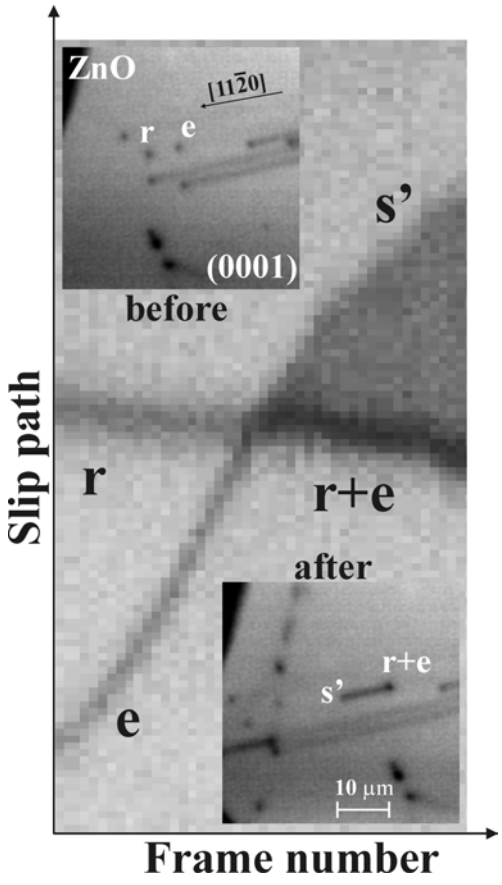

Figure 68. DCD analysis of interaction between resting defect (r) and slipping threading dislocation segment (e) approaching. Defect reaction observed is figured by the insets given. Dynamics and contrast behaviour of individual defects (r, e, s') and defect complex (r+e) are reflected by the DCD plot. (s') labels a screw-type line defect structure generated.

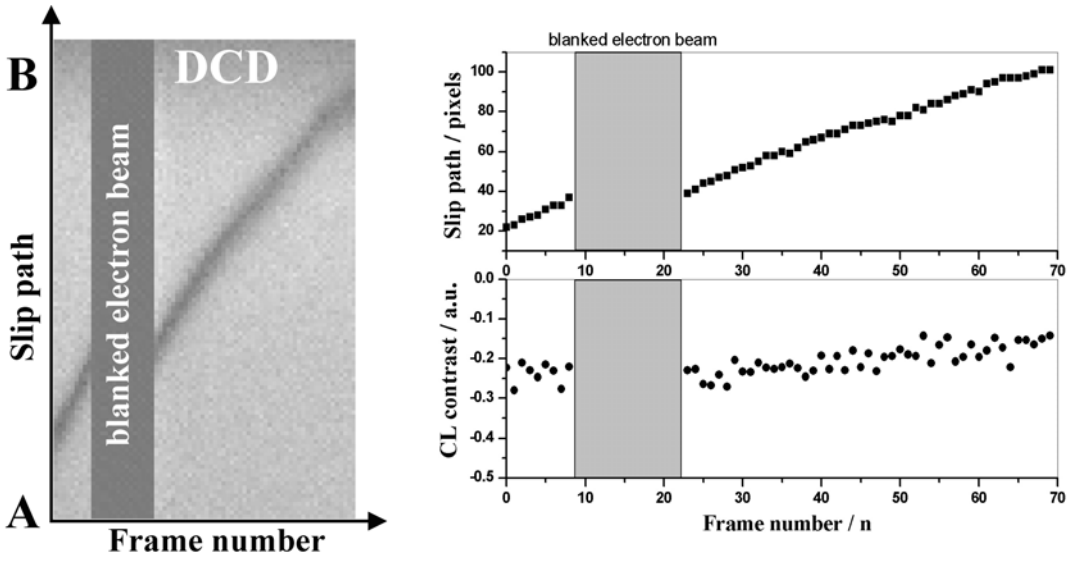

(a) (b)

Figure 69. (a) The DCD plot of a threading dislocation moving in ZnO (0001). The dislocation glide by REDG was interrupted by blanking the electron beam. (b) Slip path and CL contrast as extracted from the DCD pattern.

In Figure 70, for a second case of threading dislocation in ZnO (0001) the velocity and related CL contrast behaviour are pictured in common diagram. The velocity and contrast curves seem to be related to each other over a large range, hinting at possible correlation.

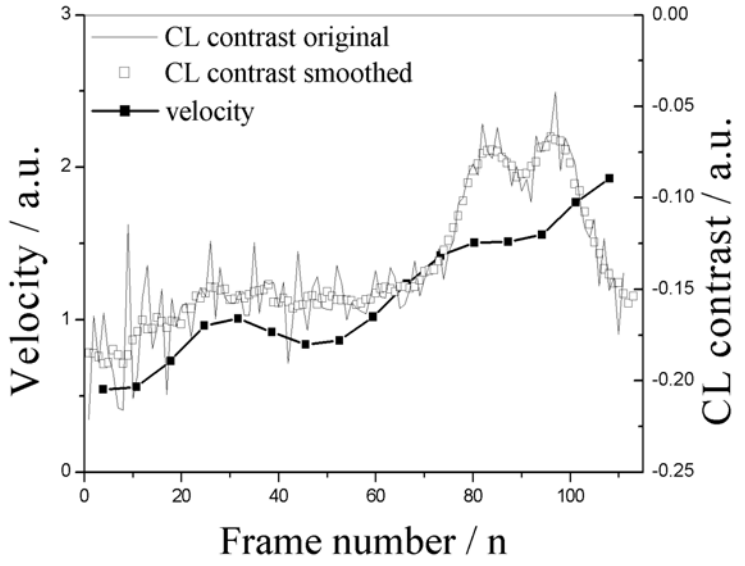

Figure 70. Correlated behaviour of velocity and CL contrast of a threading dislocation moving on prismatic slip plane in ZnO.

Figure 71 (a) deals with the evaluation of the dynamic CL contrast at a surface-parallel dislocation segment on basal slip plane in ZnO (0001) shown in Figure 67.

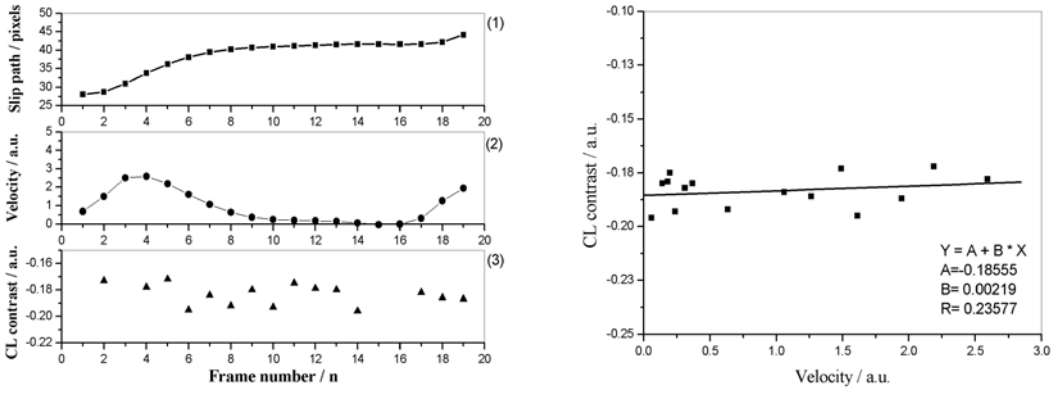

(a) (b)

Figure 71. (a) Slip path (1), dislocation velocity (2) and CL contrast (3) as derived from the DCD shown in Figure 67 (b) and plotted versus frame number. (b) The graph shows correlation of CL contrast to slip velocity of the edge dislocation presented in Figure 67 (a).

The edge-type line part has slipped over a relative short distance partially in accelerated and decelerated mode. Analyzing the DCD plot data, a so-called “contrast-velocity correlation graph” as presented in Figure 71 (b) could be developed. The plot yields a very small decrease of the CL contrast values with growing defect glide speed. This rather weak effect has been confirmed by additional similar experimental findings. In particular, there are clearer results obtained for glide

dislocations in GaAs. The pictures in Figure 72 illustrate the measurement procedure at an expanding dislocation half-loop in GaAs (111).

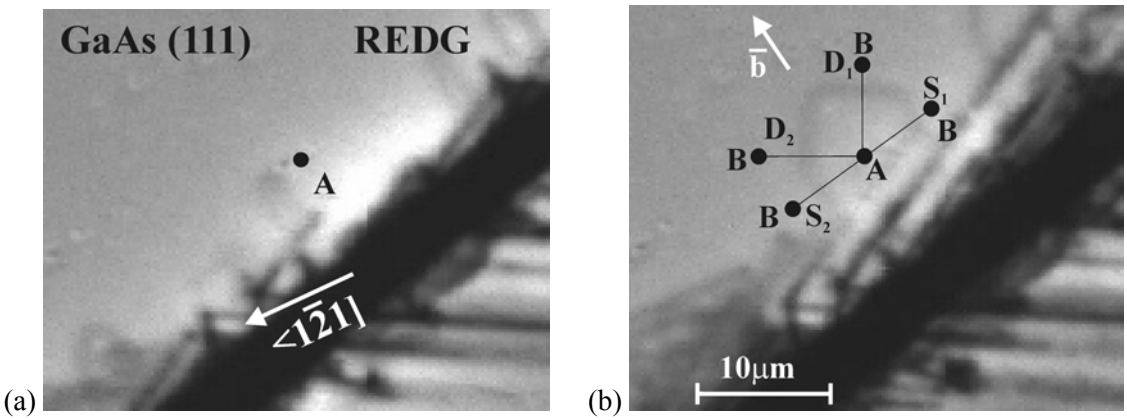

Figure 72. The first and last frame of entire movie for a dislocation loop structure (a, b). Different orientations of recording lines **AB** for generation of DCD of dislocation segments D_1, D_2, S_1, S_2.

The screw- (S_1) and the two 60°-type segments (D_1, D_2) in the loop structure could be recorded and analyzed. The corresponding data regarding slip path, velocity and CL contrast value are collected in Figure 73 (a, c) and Figure 74 (a).

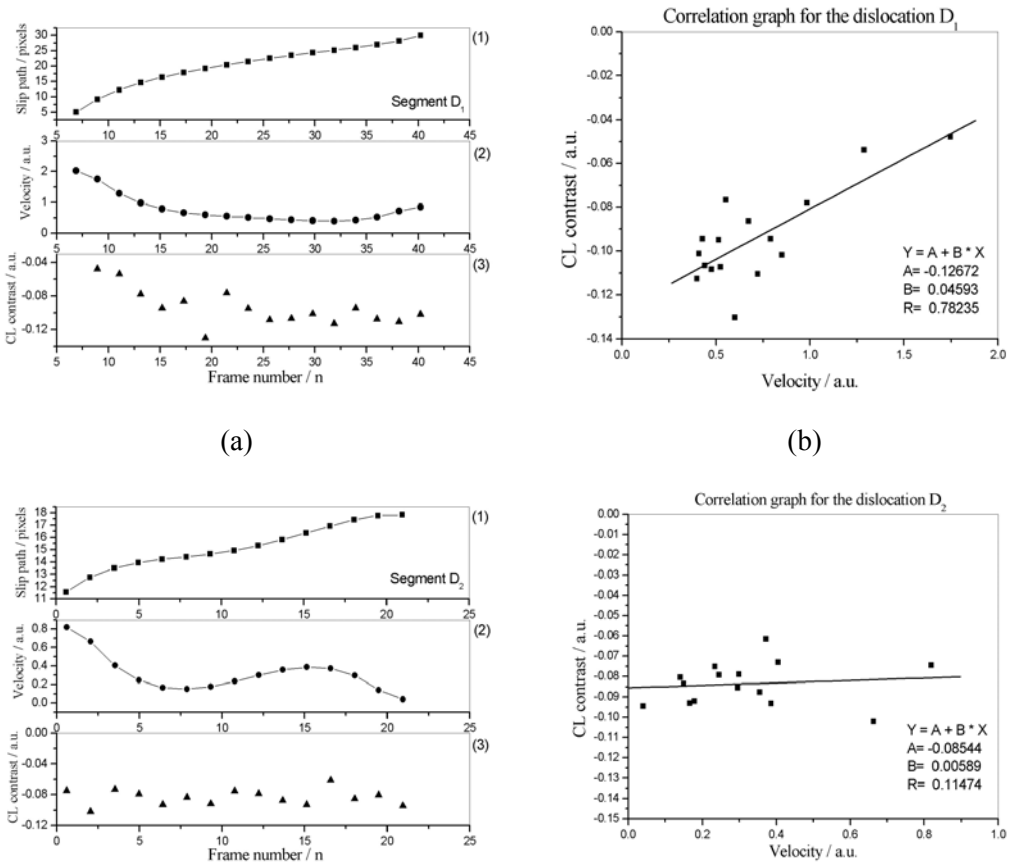

Figure 73. The correlation graphs for two 60°-dislocation segments of the same half-loop structure in GaAs (111).

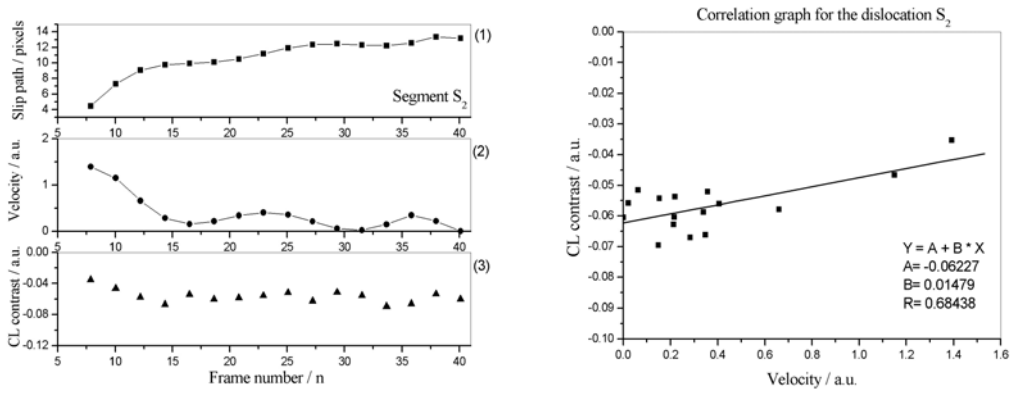

(a) (b)

Figure 74. The correlation graphs for mobile screw dislocation segment of the same half-loop structure as shown in Figure 73.

Conclusions concern the contrast-velocity correlation graph given in Figure 73 (b, d) and Figure 74 (b). In all cases presented, a decrease of the contrast value with velocity is indicated. Thus, the effect of contrast reduction versus defect velocity seems to be supported by these findings. Furthermore, this effect is found to be more pronounced for the fast edge- and screw components in the half-loop configuration. There is no distinct dependence on the structure type.

Figure 75 contains results that again confirm the tendency of a decrease of dislocation contrast if slip velocity rises.

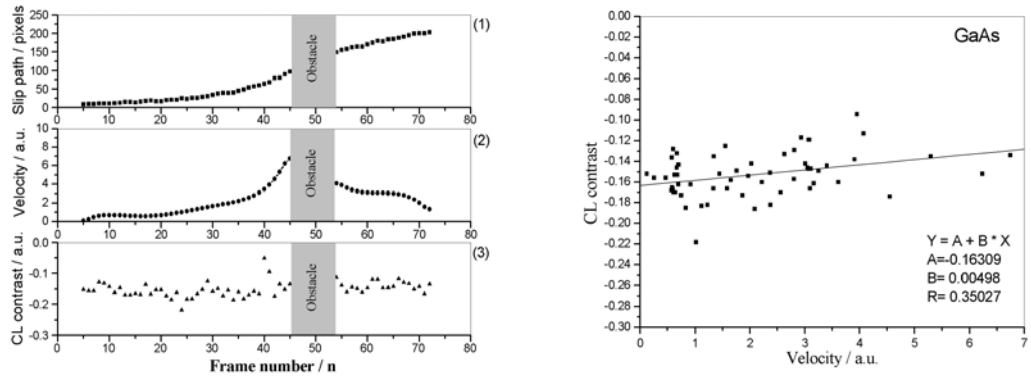

(a) (b)

Figure 75. (a) The slip path and velocity of 90° dislocation segment as derived from the corresponding DCD. (b) Plot of dislocation CL contrast correlation with its velocity. The data point fitted by linear equation.

The measurements have been conducted at a surface-parallel 90° line segment of a dislocation loop structure in GaAs (111). This segment showed non-monotonic dynamics including weak interaction with an obstacle. Also under such conditions an apparent linear contrast-velocity correlation holds up.

The contrast-velocity relationship established above as a reduction of dislocation-bound CL contrast for increasing slip velocity has to be explained by the recombination activity of the dislocations in dynamic state. According to the Peierls mechanism a change of the kink density is believed to be responsible for this effect. If kinks are assumed to be involved as recombination

active site, that is suggested by the REDG operation observed, lowered density of kinks should exist at the dislocation line for higher glide velocity.

Recombination activity of a dislocation as a whole is caused by the recombination at all kink sites of both positive and negative double kinks. Therefore, the concentration of the double kinks has to be considered (see equation (7)). Upon the stress applied the negative double kinks shrink up [hir82] lowering second term in the equation, therefore sum of these terms decreases.

The remaining first term needs more detailed consideration.

It may be understood in the framework of a simplified kink dynamics model. The experimental conditions employed have realized a constant temperature, but the dislocation was driven by stress gradients resulting in accelerated or decelerated defect motion. The change of slip velocity is believed to originate in stress-related effect on the kink migration speed. Assuming the kink nucleation rate to be constant, than decrease of the kink lifetime due to enhanced kink migration velocity should cause a lower line density of kinks for increased dislocation glide speed.

However, it must be stated, that the effect of dynamic contrast reduction is not sufficiently pronounced for establishing the kinks sites as basic recombination centers.

6 Evidence of different CL contrast and dynamical properties of A(g) and B(g) dislocations

6.1 Recombination activity and dynamics of polar A(g) and B(g) dislocations in basal plane slip system

For the first time, the CL contrast properties of polar edge-type dislocation structures in ZnO could be studied in detail. Recognizable A(g) and B(g) dislocations were verified in the defect arrangements around indents on $(10\bar{1}0)$ surfaces of ZnO samples. The edge-type dislocations with the polar A(g) or B(g) core structures as determined by A- or B-atom termination of the extra half planes occur side by side in the arms of two-fold dislocation rosettes. Figure 76 is the CL picture of a corresponding rosette arm pointing in $<11\bar{2}0>$ direction.

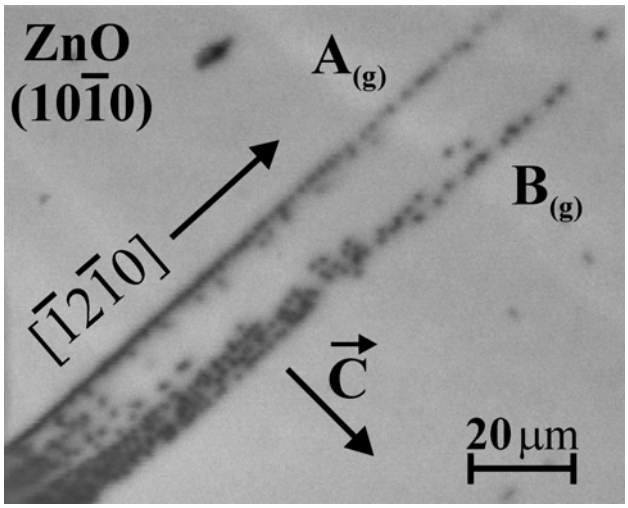

Figure 76. CL picture of threading edge-type dislocation segments with polar A(g) and B(g) core structure, respectively, which occur in the same arm of a dislocation rosette generated by indentation on (10-10) ZnO sample surface.

According to the orientation of the *c*-axis, threading segments of the A(g) and B(g) dislocations are collocated in two branches formed in the rosette arm. The given dislocation arrangement allows a detailed investigation of the CL contrast strengths appearing at the A(g) and B(g) dislocation segments. The detailed findings are presented in Figure 77 (a-d).

Figure 77 (a) shows the CL map displaying a different CL contrast strengths at single defects belonging to the A(g) and B(g) group, respectively. The intensity profile in Figure 77 (d) as extracted along **AB** yields a ratio of the CL contrast values for the A(g) and B(g) dislocations:

$$C_{A(g)}/C_{B(g)} = 0.7.$$

This contrast ratio has been found to be different for low and higher temperature as given in Table 6-1.

Table 6-1.: Results of CL contrast profile measurement on polar dislocations at low and room temperatures.

72 K	295 K
$C_{B(g)}$= 0.24÷0.30	$C_{B(g)}$= 0.31÷0.38
$C_{A(g)}$= 0.22÷0.26	$C_{A(g)}$= 0.17÷0.27
$C_{A(g)}/C_{B(g)}$=0.87	$C_{A(g)}/C_{B(g)}$=0.71÷0.55

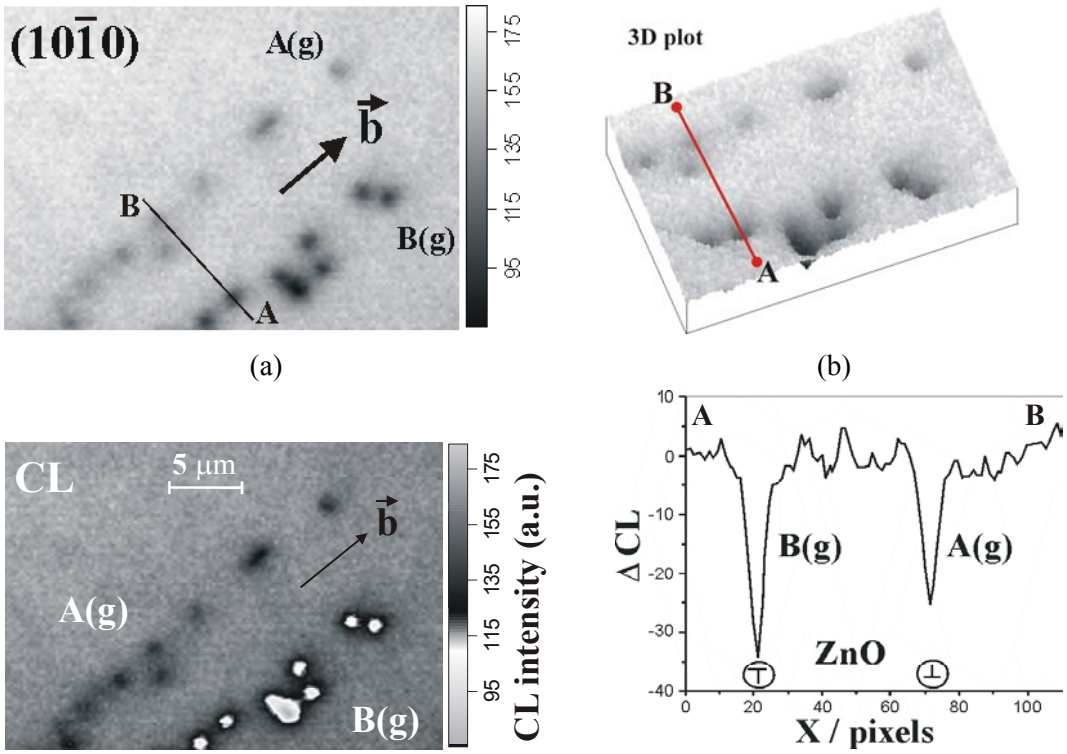

Figure 77. Difference in CL contrasts at A(g)- and B(g)-type glide dislocations in ZnO revealed by CL micrograph (a) and profile measurement (d), respectively, at single threading dislocation segments in A(g)- and B(g)-branches, respectively. (b) and (c) are the 3-D plot and so-called modified gray scale representation of (a).

The tendency of the CL contrast at B(g)-dislocations to increasing with temperature raise is seen from the table, while the CL contrast of the A(g)-type dislocations remains almost constant. At low temperature, the contrast ratio is closer to one, i.e. the contrast values are comparable. However, at room temperature, the CL contrast difference is more pronounced.

The contrast ratio corresponds immediately with the difference in recombination activity [hil98] of the A(g)- and B(g)-type dislocations:

$$C_{A(g)}/C_{B(g)} = \lambda_{A(g)}/\lambda_{B(g)}.$$

The evidenced dependence of the CL contrast on dislocation type may be ascribed to the opposite polar core structures in the A(g) and B(g) dislocations.

6.2 Inversion of glide velocity ratio for A(g) and B(g) dislocations

A special run of experiments has discovered a very interesting dynamic behaviour of the polar glide dislocations in ZnO. A measurement of dislocation velocity was performed under in-situ indentation at different temperatures. The surface $(10\bar{1}0)$ was being indented at temperatures in the range from 72 K up to 295 K.

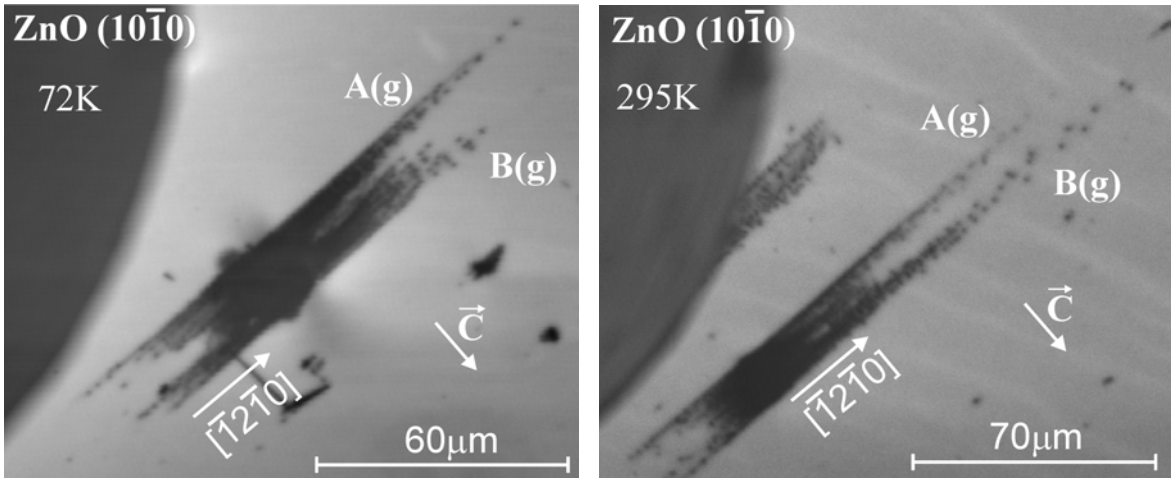

(a) (b)

Figure 78. Inversion of dislocation glide velocity upon in-situ indentation at different temperatures. Indented at 72 K (a) and 295 K (b) respectively, during the short dwell time.

Two extreme cases are illustrated in Figure 78. A single frame of SEM-CL movie obtained during indentation at 72 K (Figure 78 (a)) contains rosette arms with the branches of polar dislocations. The B(g)-type polar dislocations being usually of higher mobility at room temperature (as deduced from Figure 78 (b)) show shorter slip path as compared to the length of the A(g) arm. Contrary to this, absolutely new finding the B(g)- and A(g)-dislocations possess a mobility ratio >1 at higher temperatures (Figure 78 (b)). The polar dislocations moved in the same strain field gradient that permits to apply the concept of dislocation mobility to the comparison. Thus, an inversion of the mobility ratio of the A(g)- and B(g) dislocations can be established.

During the heating up of the sample indented at low temperature, the dislocations moved due to residual stresses and the rosette arms expanded, finally the lengths of the A(g)- and B(g)-branches were equalised at room temperature. The change of slip path for the A(g) and B(g) dislocations with temperature is shown in Figure 79.

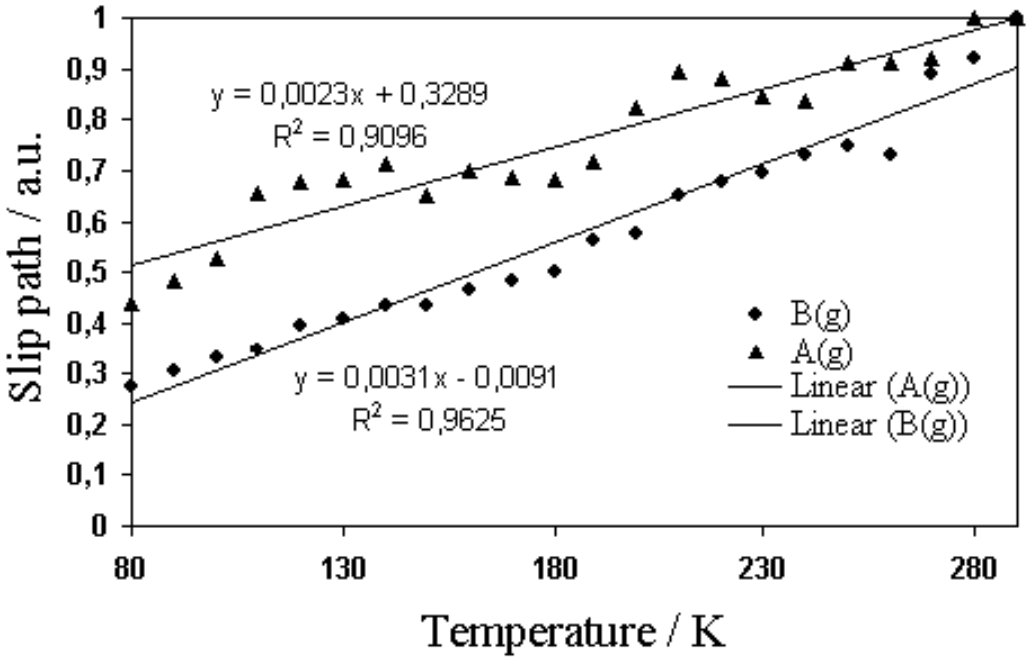

Figure 79. Expansion of A(g) and B(g) dislocation branches in rosette arm during heating up of ZnO sample formerly indented on (10-10).

The distinct temperature dependences of slip path in the A(g) and B(g) branches hint at a lower activation energy for A(g) dislocation movement as compared to that one for the B(g) dislocations, as given in Table 6-2. The magnitudes of velocities as measured for the B(g) and A(g)-type dislocations at low and high temperature are given in this table.

Table 6-2.: Glide velocities and calculated activation energies for polar dislocations moving in (0001) slip planes at low and high temperature, respectively.

Polar dislocation type	72 K	295 K	Activation energy
B(g)	$V_{B(g)} \geq$ 80 μm/s	$V_{B(g)} \geq$ 4200 μm/s	≈32,5 meV
A(g)	$V_{A(g)} \geq$ 170 μm/s	$V_{A(g)} \geq$ 350 μm/s	≈5,9 meV

Utilizing Arrhenius plot diagrams, the activation energies are obtained to be approximately 32,5 meV for B(g) and 5,9 meV for A(g), respectively (Table 6-2).

Despite comparable A(g) and B(g) dislocation slip paths in the rosette arms under equilibrium condition, that indicates similar critical shear stresses, a clear difference in the absolute mobility values for both dislocation types is expected.

The true dislocation mobility of A(g) and B(g) dislocations can be observed only at really moving defects under dynamic conditions. Applying in-situ micro-indentation, a development of the rosette arms has been revealed. In particular, the formation of the A(g) and B(g) branches could be distinguished by a tricky experimental procedure. In Figure 80, the expansion of the A(g) and B(g) branches in a rosette arm as proceeding for stepwise loading ($\sigma_1<\sigma_2<\sigma_3$) is analyzed by employing the DCD plots generated from corresponding movie.

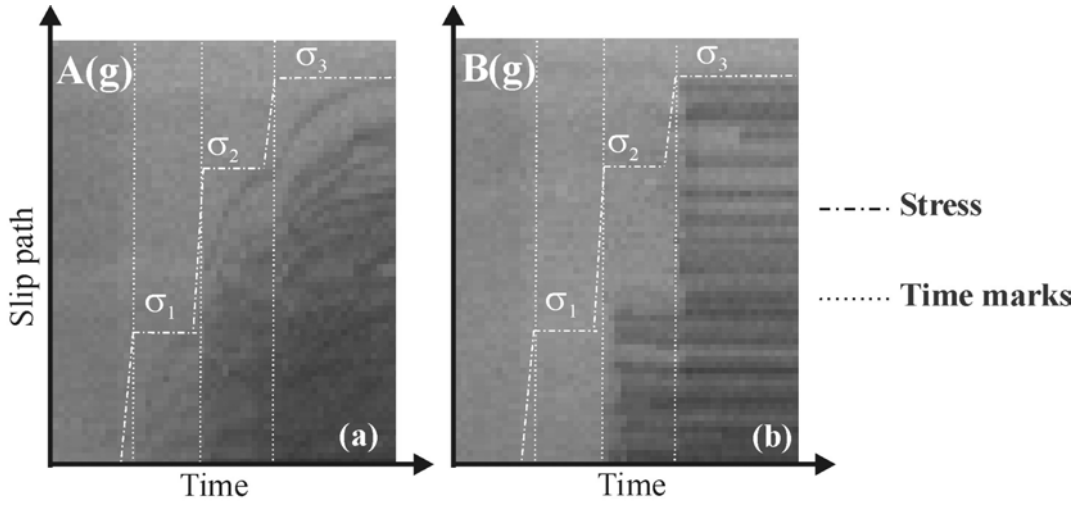

Figure 80. Stepwise motion of dislocations upon in-situ indentation on (10-10) at room temperature. (a) Dynamics of single A(g)-type dislocations moving with gradual deceleration. (b) High velocity B(g)-type dislocations motion is displayed.

The B(g) branch exhibits a step-like expansion, whereas the A(g) branch expands more continuously. The DCD diagrams prove fast motion in case of the B(g) dislocations and clear slower motion of the A(g) dislocations under temporarily constant load. A velocity ratio of

$$V_{B(g)} / V_{A(g)} \approx 12$$

is obtained.

In the DCD plot of Figure 81 is seen the slip-path vs. time curve for the isolated threading segment slipping in front of the A(g) branch of a rosette arm. Its shape is fitted by

$$l \sim \sqrt{t}$$

pointing at 1/r-decay of the local stress field.

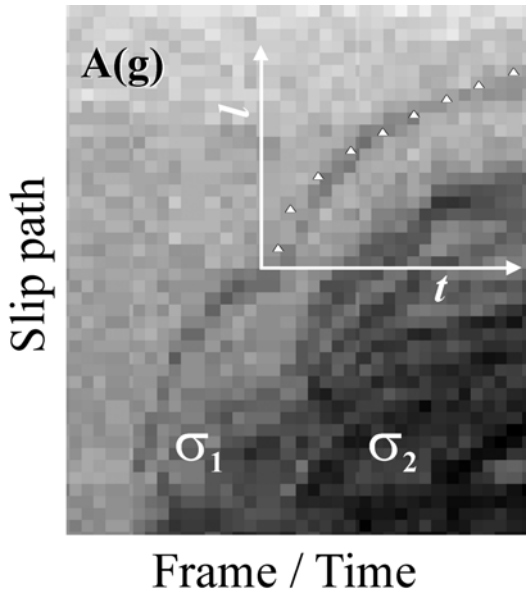

Figure 81. Analysis of dislocation dynamics by means of DCD plot. The DCD pattern considered represents the local dynamics of an individual A(g) threading dislocations propagating in the polar branch of the rosette arm under stationary load σ. Indentation load which was in-situ changed from σ_1 to higher σ_2 after distinct dwell time.

The defect segment shows decelerated movement related to

$$V \sim \sigma_0/r.$$

The fast movement of single threading dislocation segments in the B(g) branch could not be resolved.

The results presented in this chapter discover a striking relationship between the dynamic behaviour and the electrical activity of the polar A(g) and B(g) dislocations. In case of the B(g) dislocations, strong recombination activity correlates with higher dynamic mobility, whereas for the A(g) dislocations a weaker recombination behaviour corresponds with lower mobility during glide motion. This tendency is supported by the low temperature properties observed at the A(g) and B(g) dislocations.

7 Summary and conclusions

The presented work dealt with systematic studies on the dynamic and electrical dislocation properties in ZnO bulk crystals. Based on conventional CL microscopy in the scanning electron microscope and a new kinematical SEM-CL technique the appearance of plastic deformation at low temperature, operation of various slip systems and generation and propagation of glide dislocations have been investigated in context with the localised luminescence behaviour.

In the theoretical part the fundamental dislocation structures occurring in wurtzite type crystal lattices were reviewed. Dislocation loop structures have been designed using basic types of dislocation segments, which allow to describe the propagation of glide dislocations. Furthermore, the probability of possible slip systems could be estimated, and the resulting glide prism models for local plastic micro-deformation have been developed.

A detailed consideration of the hypothetical core structures of the different dislocation types in respect of distinct dangling bond configurations yielded a loop structure model reflecting expected electrical activities of the individual dislocation segments forming a loop structure.

Fundamentals of the Peierls mechanism taking into account both thermal activation and recombination stimulated kink processes were employed to treat the dynamics of dislocations.

Verification of recognizable dislocation arrangements as an essential precondition for the systematic experiments performed were realised by applying micro-indentation and scratching on the low-indexed basal and prismatic sample surfaces under in-situ conditions.

Plastic deformation in the ZnO bulk samples could be proved at temperatures between 70K and 300k. Simultaneous activation of basal plane and prismatic plane slip systems identified as $\{0001\}<11\bar{2}0>$ and $\{10\bar{1}0\}<11\bar{2}0>$, respectively, that have small relative Peierls stresses, was observed. These slip systems formed the typical glide geometry occurring in the micro-deformation processes. Dislocation propagation in both slip systems was revealed by means of kinematical SEM-CL during in-situ micro-indentation and scratching.

Overall characteristics of the dislocation propagation were found to be determined by high defect mobility and long-distance movement in the whole temperature range between room temperature down to the lowest temperature applied. Single dislocation slip was observed in basal plane as well as in prismatic plane slip systems for the case of thermal activation and REDG effect, too.

High resolution CL microscopy enabled the identification of the glide dislocation types generated. All introduced defect, so far recorded by CL imaging, were a-type dislocations (Burgers vector: $1/3<11\bar{2}0>$) with polar core structure if belonging to the basal plane slip system or showing non-polar core structure if appearing in the prismatic plane slip system. The identified dislocations exhibited very similar, but not identical electrical activity.

The principal topic of this work was focussed on the disclosure of an expected type dependence of dislocation dynamics and electrical activity, and/or of an impact of dynamics-related structural particularities on the dislocation properties.

Single dislocation dynamics have been studied in basal plane and prismatic plane slip systems at defects moved in the strain field gradients caused by indentation or scratching. The kinematical SEM-CL investigations proved rather different dynamic behaviour for dislocations affected by the same local stress field. Accelerated and decelerated as well as antiparallel dislocation motion have been found. Particular defect reactions such as formation and back formation of dislocation parts, dislocation-dislocation interaction and pinning by obstacles could be recognised.

The dynamic behaviour studied at threading dislocation segments and surface-parallel dislocation loop structures in $(10\bar{1}0)$ and (0001), respectively, established type-dependent mobility of edge and screw dislocations and, in particular, gave clear evidence of different dynamic properties of the polar A(g) and B(g) dislocation structures. Motion of prismatic loops observed were regarded as correlated movement of dislocation segments belonging to different neighboured slip systems. The edge dislocations have been found to move faster than the screws, and the B(g) type dislocation exhibited a considerably higher mobility as compared to an A(g) type dislocation. The mobility ratio $V_{A(g)}/V_{B(g)}$ appeared to be temperature dependent. This finding hints at a larger activation energy for the dynamics of B(g) dislocations. Asymmetric expansion of the loop structures was observed, it indicated following order of type-dependent dislocation mobility:

$$\mu_{90} > \mu_{60} > \mu_{30} > \mu_0.$$

Imaging of moving dislocations by kinematical SEM-CL revealed glide dislocations as extended mobile recombination centers. All types of dislocations recognised by CL dark contrasts could be regarded as non-radiative centers. Differences in the CL contrast strength recorded at edge- and screw-type dislocation segments could directly be related to distinct recombination activity. Quantitative analysis provided the contrast ratio

$$C_{edge}/C_{screw} = 1.4$$

A similar different contrast behaviour could be discovered for the A(g) and B(g) dislocations, where contrast ratio amounted to

$$C_{A(g)}/C_{B(g)} = 0.7$$

and showed a dependence on temperature.

It is worth mentioning, that the correlation between dynamic and CL contrast behaviour observed was observed. The higher the relative slip velocity, the higher the CL contrast. In case of the polar dislocations it may be concluded that the higher recombination strength correlates with the larger activation energy derived for the dynamic behaviour.

The non-polar ***a***-type dislocations possessed similar dynamic and electrical properties as described above, however, a direct quantitative comparison with the polar dislocations was not possible.

Quantitative CL contrast analyses have been performed by using a special procedure of Bezier-curve guided contrast profile measurements over surface-parallel dislocation line structures in order to register the contrast properties of neighboured dislocation segments differing in structural type. Measurements taken on a half-loop structure documented quantitative CL contrast variation between the screw- and edge-type part in the half-loop, thus

$$C_{90} > C_{60} > C_{30} > C_0$$

as expected in the framework of the dangling bond model designed.

The important issue of this work was to find out a certain correlation between the dynamic and electrically active properties of the glide dislocations. For this purpose, it was necessary to realise direct access to the recombination behaviour of the dislocations during moving state. The kinematical SEM-CL is a unique tool especially designed and developed to acquire at the same time data of dislocation-bound CL contrast and dynamics for individual single dislocations. This new technique supplied the substantial information needed by means of the SEM-CL movies, which documented whole history of dislocation movement and momentary CL contrast behaviour. For the first time, the DCD method could be utilised to analyse a complete CL movie. Creation of the DCD plots allowed detailed consideration and extraction of the quantitative characteristics of dynamics and correlated CL contrast behaviour for selected dislocation segments. These data resulted in contrast-velocity-correlation graphs. This way, it rendered possible to discover a very weak phenomenon of reduced CL contrast values versus increasing slip velocity. The effect could be reproduced by analysing several dislocation structures, it is also supported by analogue findings from similar experiments with glide dislocations in GaAs.

This behaviour of the CL contrast under influence of the dislocation dynamics was unexpected. The impact of the dislocation dynamics should be understood in the framework of the kink processes in the Peierls mechanism. The preliminary explanation is based on the assumption of lowering the line density of kinks due to enhanced kink migration velocity related to stress. That is the first attempt to involve kinks as recombination centers.

In order to extend current knowledge about possible relationship between the dynamic and electrical dislocation properties several additional issues remain to be solved.

Preferably further experimental work is expected to provide essential contribution, particularly, to enlighten the electronic dislocation structure. Next studies to perform should comprise a comprehensive investigation of the dynamic and electrical properties on dislocations showing Y-luminescence, thereby very valuable spectroscopic information on the dislocation-induced electronic states will be available. Such experiments require the choice of materials having Y-luminescence and sufficiently high dislocation mobility at low temperature (see section 9.4 in Appendix), otherwise dislocation dynamics and electrical activity of the dislocations can not be studied simultaneously.

8 References

ale86 H. Alexander. In: Dislocation in Solids. Vol. 7. ed. F.R.N. Nabarro (North-Holland, Amsterdam. (1986) p. 113.

ale89 H. Alexander, H. Gottschalk, *Inst. Phys. Conf. Ser.* **104**(3) 281 (1989)

ale91 H. Alexander, H. Teichler. *Dislocations*. In *Materials science and technology*, Hg. R. W. Cahn, P. Haasen, E. J. Kramer, Bd. 4, Weinheim: VCH S 249 (1991).

ari94 T. A. Arias and J. D. Joannopolous, *Phys. Rev. Lett*. **73** 680 (1994).

bal76 L.J.Balk, E. Kubalek, E.Menzel. Scanning Electron Microsc. **I** (1976)

bec00 T. Becker, M. Kunat, C. Boas, U. Burghaus, C. Wöll, *J.Chem. Phys*. **113** 6334 (2000)

ben97 J. Bennetto, R. W. Nunes, D. Vanderbilt. *Phys. Rev. Lett*. **79** 245 (1997).

big92 J. R. K. Bigger *et al., Phys. Rev. Lett*. **69**, 2224 (1992).

bond73 I.E. Bondarenko, V.N. Erofeev and V.I. Nikitenko. *Sov. Phys*. JETP 37, 1109 (1973)

bre65 J.E. Bresenham, *IBM Systems Journal*, **4**(1), 25 (1965)

bul95 V. V. Bulatov, S. Yip, and A. S. Argon, *Phil. Mag*. **A72**, 453 (1995).

bul97 V.V. Bulatov, João F. Justo, Wei Cai, and Sidney Yip, *Phys. Rev. Lett.* **79**(25) 5042 (1997)

cha62 J.R. Chaudhuri, J.R. Patel, L.G. Rubin, *J. Appl. Phys.* **33** 2736 (1962)

cho77 S. K. Choi, M. Mihara and T. Ninomiya *Jap. J. Appl. Phys*. **16** 737 (1977)

chu 60 Churchman E. T. *Trans. Met. Soc. AIME*. **218** 262 (1960)

chu54 Churchman E. T. *Proc. Roy. Soc*. **226A**, 216 (1954)

cim64 A. Cimino, G. Mazzone, P. Parta.: *Z. Phys. Chem*. N.F. **41** 3 (1964)

cot53 A.H. Cottrell, F.R.N. Nabarro, In: Cottrell A.H. Dislocations and plastic flow in crystals .N.Y., 98 (1953)

dea79 P.J. Dean, *Inst. Phys. Conf. Ser.* **46** 100 (1979)

dea84a P.J. Dean, *phys. stat. sol. (a)* **81** 625 (1984)

dea84b P.J. Dean, G.M. Williams, G. Blackmore, *J. Phys. D: Appl. Phys.* **17** 2291 (1984)

don78 C. Donolato, *Optik* **52** 19 (1978/79)

don97 Don L. DeVoe and A.Pisano, *J. Microelectromechanical Sys*. **6(**3) (1997)

due95 M. S. Duesbery, B. Joos: Dislocation motion in silicon: the shuffle–glide controversy. Phil. Mag. Lett. **74** 253 (1995)

far83 G. Farin: Algorithms for Rational Bezier Curves. *Comput. Aided. Des.* **15** 73 (1983)

far99 J.L. Farvacque and P. François, *Physica B*, **273-274**, 995 (1999)

fra49 F.C. Frank, *Physika*, **15** 131 (1949)

geo79 A. Georg and G. Champier, *Phys. Stat. Sol*. **A53** 529 (1979)

geo87 A. George, J. Rabier, *Rev. Phys. Appl.* **22** 941 (1987)

got83 H. Gottschalk, *J. Phys. C4* **44** 475 (1983)

got93 H. Gottschalk *et al., Phys. Stat. Sol.* **A138**, 547 (1993).

han95 L. B. Hansen *et al., Phys. Rev. Lett*. **75**, 4444 (1995).

heg82 M. Heggie and R. Jones, *J. Phys. (Paris)* **43**, 45 (1982)

heg83 M. Heggie and R. Jones, *Phil. Mag. B* **48**, 365 (1983)

heg83a M. Heggie and R. Jones, *Phil. Mag. B* **43**, 379 (1983)

hel98 E. S. Hellman, MRS Internet *J. Nitride Semicond. Res*. **3**, 11 (1998)

her84 W. Hergert, L. Pasemann, *phys. stat. sol. (a)* **85** 641 (1984)

her87a W. Hergert, P. Reck, L. Pasemann, J. Schreiber, *phys. stat. sol. (a)* **101** 611 (1987)

her87b W. Hergert, S. Hildebrandt, L. Pasemann, *phys. stat. sol. (a)* **102** 819 (1987)

hil97 S. Hildebrandt, H. Uniewski, J. Schreiber, H.S. Leipner, *J. Phys. III France.* **7** 1505 (1997)

hil98 S. Hildebrandt, J. Schreiber, W. Hergert, H. Uniewski, H.S. Leipner, *Scan. Microsc. Int.* **12**(4) 535 (1998)

hir79 P.B. Hirsch, *J. de Phys*. **40** 117 (1979)

hir82 J. P. Hirth, J. Lothe, „Theory of Dislocations“, 2nd ed. Wiley, New York (1982)

hirs81 P.B. Hirsch, A. Ourmazd and P.Pirouz, *Inst. Phys. Conf. Ser* **60** 29 (1981)

hoe01 L. Hoering. Thesis Univ. Halle 2001

hoe01a L. Höring, J. Schreiber, U. Hilpert, *Sol. State Phen.* **178/179** 139 (2001)

hol62 D.B. Holt, *J.Chem. Phys. Sol.* **23** 1353 (1962)

hol96 D.B. Holt, *Scan.Microsc.***10**(4) 1047(1996)

hor58 J. Hornstra, *J. Chem.Phys. Sol.* **5** 129 (1958)

hu75 S. M. Hu, *J. Appl. Phys*. **46**, 1470 (1975)

huan95 Y. M. Huang, J. C. Spence, and O. F. Sankey, *Phys. Rev.Lett*. **74** 3392 (1995).

iun99 Y. L. Iunin, V.I. Nikitenko, *Phys. Stat. Sol. (a)* **171**, 17 (1999)

jac93 K. Jacobi*, Springer Ser. Surf. Sci*. **33,** 103 (1993)

jahn98 B. Jahnen, et all. *MRS Internet J. Nitride Semicond. Res*. **3**, 39 (1998)

jon79 R. Jones, *J. de Phys*. **40** 33 (1979)

jon80 R. Jones, *Phil. Mag. B* **42**, 365 (1980).

jon81 R. Jones, S. Öberg, *Phil. Mag. B* **43**(5) 839 (1981)

jon93 R. Jones, 0A. Umerski, P. Sitch, M.I. Heggie and S. Öberg. *Phys. Stat. Sol. (a)***138** 369 (1993)

joo97 B. Joós, M.S. Duesbery, *Phys. Rev. B* **55**(17) 11161 (1997)

kir78 L.G.Kirichenko, V.F.Petrenko and G.V. Uimin, JETP, **74** (1978)

kol96 H.R. Kolar, J.C. Spence, H. Alexander, *Phys. Rev. Lett.* **77**(19) 4031 (1996)

kus95 S. Kusanagi, T. Sekiguchi, K. Sumino, *Mater. Sci. Forum* **196-201** 1195 (1995)

lab75 R.Labusch and W. Schröter, *Inst. Phys. Conf. Ser.* **23** 56 (1975)

lei00 H.S. Leipner, Habilitation MLU Halle (2000)

lou 87 F. Louchet, J. Thibault-Desseaux. Rev. Phys. Appl. **22** 207 (1987)

lou81 F. Louchet, *Inst. Phys. Conf. Ser.* **60** 29 (1981)

mae00 K. Maeda, K. Suzuki, Y. Yamashita and Y. Mera, J. Phys. Condens. Matter **12** 10079-10091(2000)

mae81 K. Maeda, S. Takeuchi, *Jap. J. Appl. Phys.* **20**(3) L165 (1981)

mae83a K. Maeda, S. Takeuchi, *J. Phys. C4* **44** 375 (1983)

mae83b K. Maeda, S. Takeuchi, *J. Appl. Phys.* **54** 161 (1983)

mae85 K. Maeda, S. Takeuchi, *Yamada Sci Found. conf. IX*, Ed.: H. Suzuki et al. 433 (1985)

mae96 K. Maeda, S. Takeuchi, (eds. F.R.N. Nabarro, M.S. Duesbery), Dislocations in Solids 10. Elsevier, Amsterdam (1996), p.445

mak99 H. Maki, N. Ichinose, S. Sekiguchi, N. Ohashi, H. Haneda, J. Tanaka, *Key Eng. Ma*t. **169-170**, Trans. Tech. Publications, Switzerland, 109 (1999)

mar63 A.N. Marino, R. E. Hanneman, *J. Appl. Phys*. **34** 384 (1963)

mark79 S. Marklund, *Phys. Stat. Sol. (b)* **92** 83 (1979)

mukh01 A.K. Mukhopadhyay et al., *Bull. Mater. Sci.* **24**(2) 125 (2001)

nin79 T. Ninomiya, *J.Physique suppl.* C6 **40** 143 (1979)

no91 S. Nosé, Prog. Theor. *Phys. Suppl*. **103** 1 (1991).

ohn98 T. Ohnishi, A. Ohtomo, M. Kawasaki, K. Takahahi, M. Yoshimoto, H. Koinuma, *Appl. Phys. Lett* **72** 824 (1998)

oht00 H. Ohta, K. Kawamura, M. Orita, N. Sarukura, M. Hirano, H. Hosono, *Electron. Lett*. **36** 984 (2000)

osip68 Yu. A. Osipiyan and I. S. Smirnova*, Phys. Stat. Sol*. **30** 19 (1968)

osip68a Yu. A. Osipiyan, Yu.I.Fedyaev, and S.A.Shevchenko, *Zh. Eksper. Teor. Fiz*. **54** 1706 (1968)

osip70 Yu. A. Osipiyan and I. S. Smirnova. *J. Phys. Chem.Solid*. **32** 1521 (1970)

osip79 Yu. A. Osipiyan and V.F.Petrenko. , *J. Phys. C6* **40** 161 (1983)

pat66 J.R. Patel and A.R. Chaudhuri, *Phys. Rev* **143** 601 (1966)

pea50 M.O. Peach, J.S. Köhler, *Phys. Rev.* **80** 436 (1950)

pei40 R. Peierls, *Proc. Phys. Soc. London* **52** 34 (1940)

pon96 F. A. Ponce, D. P. Bour, W. Gotz and P. J. Wright, Appl. Phys. Lett. **68**, 57 (1996)

proc79 Proc. Int. Symp. Dislocations in Tetrahedrally Coordinated Semiconductors; *J. Physique Coll*. **40** C6, in the foreword (1979)

read54 W.T. Read, *Phil. Mag*. **45**, 775 (1954)

read54a W.T. Read*, Phil. Mag*. **45**, 1119 (1954)

reb91 T.Yu. Rebane, G.Yu. Shreter, *Springer Proc. Phys.* **54**, (eds. J.H. Werner, H.D. Strunk) Springer Verlag Berlin 28 (1991)

ros56 Rosi F.D., Perkins F.C, Seigle L.L. *Trans. AIME*, **206** 115 (1956)

sal99 G. Salviati, M. Albrecht, C. Zanotti-Fregonara, N. Armani, M. Mayer, Y. Shreter, M. Guzzi, Yu. V. Melnik, K. Vassilevski, V.A. Dimitriev, H.P. Strunk, *phys. stat. sol. (a)* **171** 325 (1999)

schr04 J.Schreiber, S. Vasnyov. J. Phys.: Condens. Matter **16** 75-84 (2004)

schr77 J. Schreiber, Dissertation, MLU Halle

schr89a J. Schreiber, H.S. Leeipner, H.-R. Höche, *Wiss. Z. Univ. Halle* 31 (1989)

schr89b J. Schreiber, W. Hergert, *Inst. Phys. Conf. Ser.* **104** 97 (1989)

schr96 J. Schreiber, S. Hildebrandt, H. Uniewski, V. Bechstein, *Mat. Sci. Eng.* **B42** 24 (1996)

schr99 J. Schreiber et al., *Phys. Stat. Sol. (a)* **171** 89 (1999)

schro79 W. Schröter, *Inst. Phys. Conf. Ser.* **43** 114 (1979)

schu79 H. Schulz, K.H.Thiemann: *Solid State Commun.* **32** 783 (1979)

sek96 T. Sekiguchi, K. Sumino, *Mat. Sci. Eng.* **B42** 141 (1996)

stil82 F. H. Stillinger and T. A. Weber, *Phys. Rev.* A **25**, 978 (1982)

stri92 S. Strite, H. Morkoç, *J. Vac. Sci. Technol.* **B 10,** 1237-1266 (1992)

stud98 S.A. Studenkin et al., *J. Appl. Phys*. **84**(4) 2287 (1998)

van96 K. Vanheusden et al., *J. Appl. Phys*. **79** 7983 (1996)

vas04 S. Vasnyov, J.Schreiber, L.Hoering. J. Phys.: Condens. Matter **16** 269-277 (2004)

wil85 P.R. Wilshaw, G.R. Booker, *Inst. Phys. Conf. Ser.* **76** 329 (1985)

yac90 B. G. Yacobi and D. B. Holt, Cathodoluminescence Microscopy of Inorganic Solids. Plenum, (1990).

yon00 I. Yonenaga, T. Suzuki, *Phil. Mag. Lett.* **80**(8) 511 (2000)

9 Appendix

9.1 Refinement of dangling bond densities calculations

However, a situation when the combined case takes place may be also theoretically possible. For the instance, when condition of core at the 30° remains without changes while the 60°-dislocation losses atoms in result of diffusion and its dangling bond density goes down (see Table 3-9 and Figure 21), the highest dangling bond density will have the 30°.

On the one hand the model presented describes only possible values of dangling bonds for basal partial dislocations in wurtzite lattice, but doesn't answer a question which exactly combined case could take place. On the other hand, if to deal with mobile dislocations, gliding at low temperatures when diffusion of atoms from the dislocation core could be neglected, we could suppose that the case with maximal dangling bond densities for all types of dislocations is more probable. But taking into consideration the split reaction #8 for 60°-perfect (see Table 3-9) with a possible bond reconstruction, the 30° remains a single candidate to possess maximal dangling bonds.

Supposing that the dangling bonds (formed by solitons or kinks) in the dislocation core are centres of recombination, based on the model proposed, if the dislocations are split, the highest recombination activity should possess either a 60°- or 30°-dislocation, but not 90° as for case of perfect dislocations. Therefore, the loop structure earlier introduced in Figure 16 (b) was modified as shown in Figure 22.

Table 9-1. Results of refined calculation of dangling bond densities for basal partials dislocations in ZnO.

B(g) α					
Angle ξ^**b**	n_{DBmin}	n_{DBmax}	***l***, a	$\gamma_{min}= n_{DBmin} / \boldsymbol{l}$	$\gamma_{max}= n_{DBmax} / \boldsymbol{l}$
0°	1.7	1.7	1	1.7/a	1.7/a
30°	0.5	6.05	1.732	0.29/a	3.49/a
60°	2.4	4.4	1	2.4/a	4.4/a
90°	3.75	4.9	1.732	2.165/a	2.83/a
A(g) β					
Angle ξ^**b**	n_{DBmin}	n_{DBmax}	***l***, a	$\gamma_{min}= n_{DBmin} / \boldsymbol{l}$	$\gamma_{max}= n_{DBmax} / \boldsymbol{l}$
0°	1.7	1.7	1	1.7/a	1.7/a
30°	0.35	5	1.732	0.2/a	2.89/a
60°	2.4	4.1	1	2.4/a	4.1/a
90°	3.9	4.45	1.732	2.25/a	2.57/a

As it was shown by experiments on SEM-CL in section 5.3.1.2, the A(g)- and B(g)-types dislocations are found to possess different CL contrast i.e. recombination activity, possibly, due to difference in types of terminating atoms. The $C_{A(g)}/C_{B(g)}$ contrast ratio has been revealed to be about 0.7. Therefore, besides the values of dangling bond densities, the type of elements (atoms) has to be involved to make a refinement of the model proposed. The effective dangling bonds number is reduced for A-type atoms by a factor 0.7. This way, all as calculated numbers of dangling bonds (Table 3-9) of A-type atoms has to be multiplied by 0.7.

Thus, in order to construct the refined model of loop structure, we have to distinguish between: A- and B-types of atoms by means of factor 0.7 for the number dangling bonds of A-type, as well as A(g)- and B(g)-core structures by changing the indexes A to B and reverse.

The results of refined dangling bond densities calculations are presented in Table 9-1. The corresponding graph based on the data from the Table 9-1 is shown in Figure 82. From this plot one can deduce relationship between as calculated dangling bond densities and dislocation types.

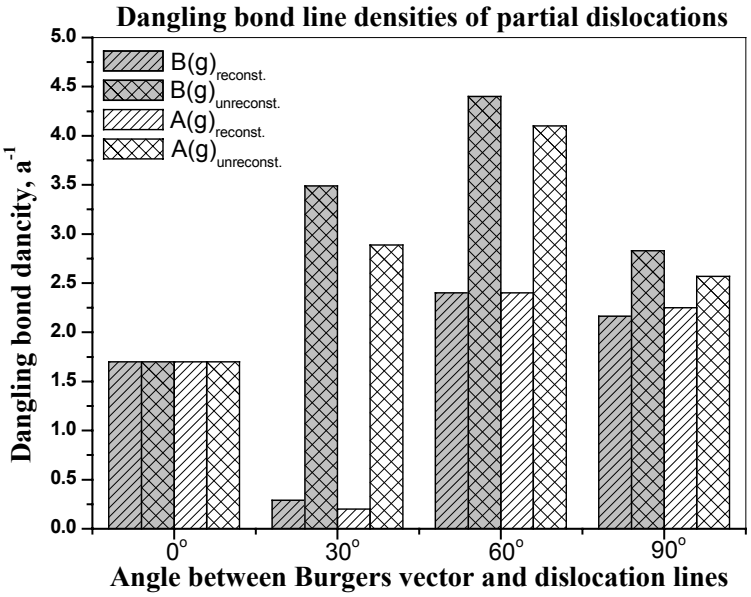

Figure 82. Diagram of the relation of line dangling bond density per lattice constant length to dislocation type for partial dislocations in wurtzite structure. Blue bars correspond to A(g), red bars to B(g).

It should be noted, that split screws don't change those dangling bond density neither under atom type rearrangement, nor under transition from one polar type of dislocations to another.

Despite the essential refinement of the calculations performed the dependences remains to be qualitatively nearly the same (compare Figure 21 and Figure 82). The possible electrical activities for the A(g)-types dislocations are seen to be lower as that for the B(g)-types. But nevertheless, according to the dangling bond density counting, the 60°-split dislocation should possess the highest electrical activity among others split defects, as it was derived without distinction between A- and B-types of atoms.

In conclusion, comparing results of dangling bond densities calculations for the basal perfect and split dislocations, it could be seen, that for the perfect dislocations the most electrical activity is expected for 90°-dislocation segment, whereas, among split defects the 60° dislocation is believed to be the most efficient recombination centre.

9.2 Peculiarities of CL intensity profile measurement

Utilizing CL SEM, it is possible to obtain information on CL contrast in whole range of signal. Science recombination activity of dislocations is represented by CL contrast stored in the CL images obtained the CL contrast should be quantitatively analysed.

The procedure of quantitative CL profile analysis proposed is based on grey scale level measurement along a straight line (scan line) selected between two points in a given CL image. To calculate coordinates of each subsequent point of the scan line the Bresenham [bre65] algorithm has been used. This algorithm allows calculation of coordinates of all points along the line selected so that to miss none of them. Grey scales values from each point placed at such imaginative scan line are sequentially pixel-by-pixel acquired and stored in a two-dimensional profile plot. After the array of CL intensity profile magnitudes is formed, the numeric data collected have to be smoothed. Actually, three- or five-point smoothing procedure could be enough to get some signal noise reduced.

Due to inhomogeneity of matrix, for instance, caused by distributed impurity or strain field gradient, the local luminescence enhancement can appear which would superpose with own CL contrast of dislocations. The local matrix luminescence enhancement gives an additional background for the CL profile. Therefore, a real CL contrast values could not be measured directly with good accuracy. Contributions of these artefacts have to be subtracted.

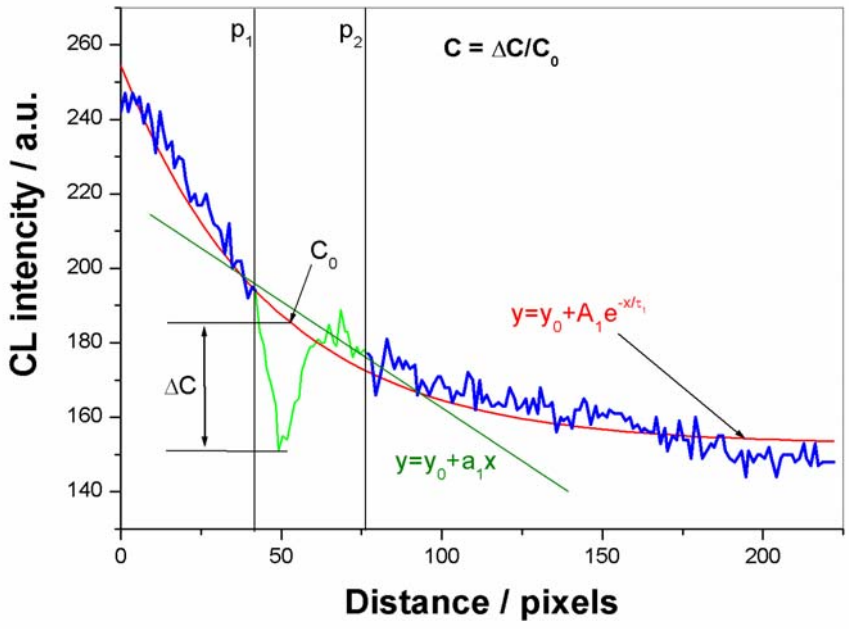

Figure 83. CL profile analysis. The local background near the defect related peak could be fitted by a linear function well, while an exponential function fits general background well.

Good results of local background subtraction have been obtained applying the 6-point linear approximation. The local background is measured apart from the dislocation CL peak. Six data points - three before and three after dislocation peak (Figure 83) have been used to calculate the

coefficients of linear function approximately describing the background. As soon as background is calculated, it is subtracted from as-measured CL profile. Thus, local CL intensity value of defect can be calculated accurate. CL contrast is calculated as a ratio of difference of CL intensity at defect and matrix area to the CL intensity in the matrix. The CL intensity at defect is represented by peak extremum (minimum or maximum), whereas matrix CL intensity has to be measured not in but close to the defect considered.

In case of the background is too wide and smooth enough, it can be fitted by a function i.e. the exponent. In order to increase accuracy, the calculation of exponent fitting parameters must be based only on the data excluding peaks. After the fitting parameters have been calculated and the fitting function describing background is derived, the latter has to be subtracted from as measured original CL intensity profile. Calculation of CL contrast in this case shows also good results.

9.3 Measurement of CL contrast depending on type of dislocation segments in GaAs

Utilization of the Bezier curve guided advanced CL contrast profile analysis to measure at the loop surface parallel structure in GaAs (111) samples is shown in Figure 84.

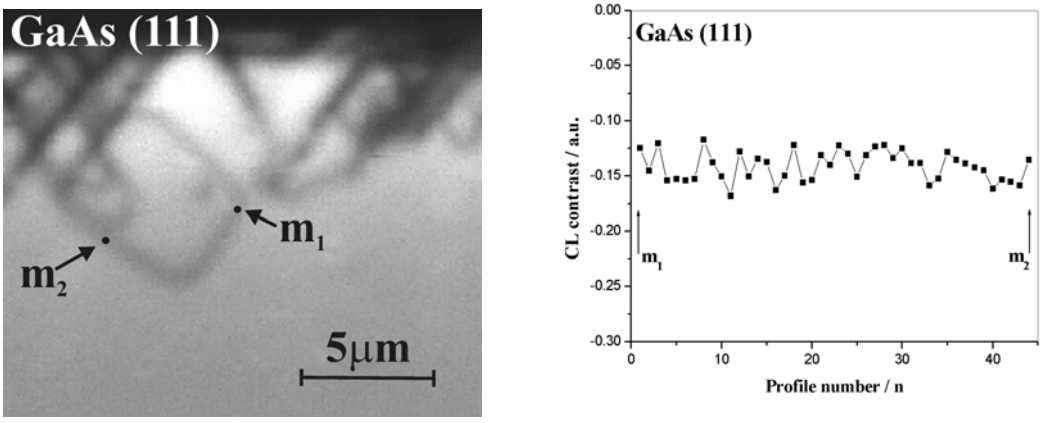

(a) (b)

Figure 84. Advanced CL contrast profile measurement in GaAs. (a) Surface parallel loop in (111). CL contrast was measurement between starting and finishing markers m_1 and m_2 respectively. (b) As measured CL contrast obtained along part of dislocation loop between markers m_1 and m_2.

No any essential dependence of CL contrast on the type of dislocations was found.

For the GaAs deviation of dislocation CL contrast from averaged value was found to be about ±5% that is within the range of measurement error. Meanwhile, for the ZnO the differences of CL contrast for edge- and screw-type dislocations reached 30-40%.

9.4 Revealing of Y-luminescence in CdS and ZnSe

The in-situ indentation and scratching tests performed at 72K under CL observation on CdTe, ZnSe and CdS samples gave evidence for local plastic deformation due to generation and propagation of dislocations carrying CL bright contrasts as displayed in Figure 85.

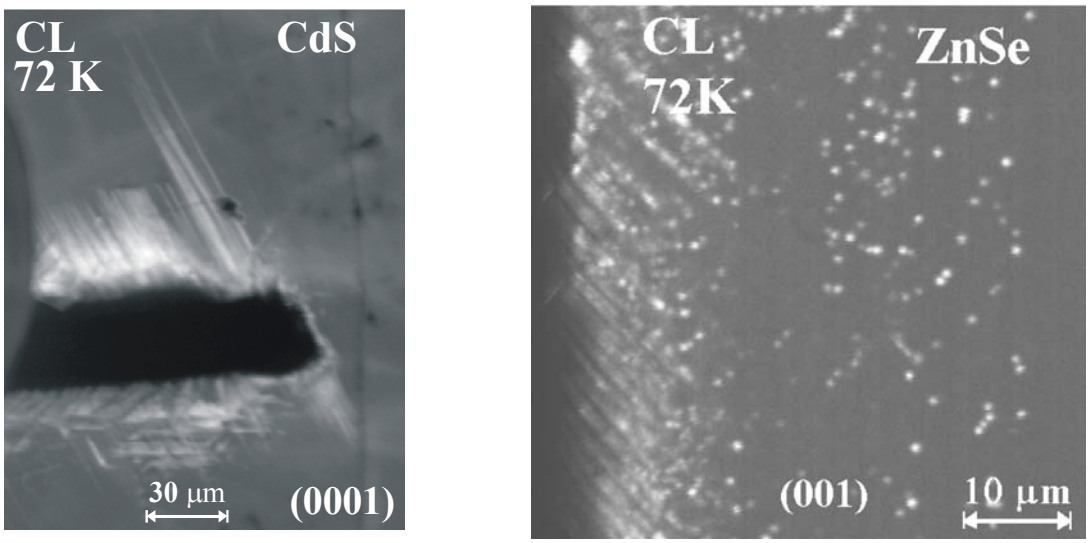

(a) **(b)**

Figure 85. Dislocation luminescence after local plastic deformation. (a) Glide dislocations introduced by in-situ scratching of CdS sample show Y-luminescence. (b) CL bright contrasts (Y luminescence) of B(g) dislocations in ZnSe.

Relatively high dislocation speed even at this low temperature has been registered by means of the CL movies taken. On the other hand, REDG effect could not be verified under excitation conditions applied. Experimental findings from the ZnSe sample which was treated ex-situ at room temperature hint at preferred propagation of B(g)-type threading dislocation segments. Y-luminescence in ZnSe was also observed in [dea79, dea84a, dea84b].

9.5 Abbreviations

III/V	binary semiconductors compound from elements of III. and V. groups
II/VI	binary semiconductors compound from elements of II. and VI. groups
A(g)	dislocation at glide-set with A-atom in core
A(s)	dislocation at shuffle-set with A-atom in core
B(g)	dislocation at glide-set with B-atom in core
B(s)	dislocation at shuffle-set with B-atom in core
gs	glide-set
ss	shuffle-set
CCD	Charge Coupled Device (Detector array)
DCD	Dynamic Contrast Diagram
EHP	extra-half plane
fcc	face centered cubic
FWHM	full width at half maximum
CL	cathodoluminescence
MBE	molecular beam epitaxy
NUV	near ultra violet
REDG	recombination enhanced dislocation glide
REDM	recombination enhanced dislocation motion
SEM	Scanning Electron Microscope(y)
SE	secondary electrons
SRH	Shockley-Read-Hall kinetics
TEM	Transmission Electron Microscope(y)
WZ	wurtzite
ZB	zincblende
Y	Y Luminescence – defect related Luminescence
Dyn-CL	dynamical SEM-CL
α	alpha- dislocation (corresponds to B(g)- or A(s)-dislocation)
β	beta-dislocation (corresponds to A(g)- or B(s)-dislocation)

Acknowledgement

I would like to take this opportunity to thank my scientific adviser Dr. J. Schreiber for inspiration, professional supervision and creative discussions.

I am deeply grateful to Prof. Dr. H.-R. Höche, chief of the Graduiertenkollehs 415 ”Defectstructurbestimte physikalische Eigenschaften von Kristallen” of the Deutsche Forschungsgemeinschaft (DFG), where I have been fortunate to be a scholar during the last three years. I am also very grateful for the financial support obtained from the DFG which in part made my work and stay in Germany possible.

I am thankful to Prof. Dr. G. Dräger for the opportunity to work in his group.

I greatly appreciate the highly productive discussions with Dr. H. S. Leipner and Prof. Dr. R.Krause-Rehberg.

Many thanks to Dipl.-eng. H. Mähl for technical support and help during SEM investigations,
Dr. R. Shantyr and Dr. V. Bondarenko for their cooperation.

I thank Dr. O. Rudenko, Dr. G. Vesna , Prof. Dr. A. Mycielski and Dr. D.M. Hofmann for giving the samples, as well as Ms. K. Lehmann for preparation of the samples and Dr. C. Eisenschmidt for conducting X-ray analysis, Prof.Dr. J.Christen and Dr. F. Bertram for CL WI experiments.

I thank my former scientific advisors: Dr. E. Shishkin and Prof. Dr. Yu. Koval for their guidance throughout my research at the National Academy of Sciences of Ukraine as well as Dr. A. Anukhin who shared his rich experience and taught me the experimental refinements.

My sincere thanks to Ms. H. Voigt as well as Irina Gets and Mikhail Berman for their kindness and profound moral support.

I thank my first scientific advisor Prof. Dr. V. Kopan for giving me deep insights into the science of physics.

Especially, I am grateful to my wife Alla for her patience and love.

CURRICULUM VITÆ

Family name:	Vasnyov
First name:	Serhiy
Patronymic name:	Volodymyrovych
Nationality:	Ukrainian
Date of birth:	11.04.1974
Birth-place:	Kyiv (Kiew), Ukraine
Marital status:	married
Address:	vul. Zapadyns'ka 3-A, k.36 Kyiv 04123, Ukraine

1980-1990	Kyiv secondary school №156.
1990-1995	National Taras Shevchenko University of Kyiv.
June 1995	Diploma of Physicist and Lecturer (Solid state physics)
1995-1999	Institute for Metal Physics of NAS of Ukraine, Kyiv
1999-2001	Scientific and product company "S&PF MODUL", Kyiv
2001-2004	DFG (GRK 415) scholarship for PhD study in Martin-Luther-Universität Halle-Wittenberg, Halle-Saale, Germany

Halle (Saale), October 26, 2004

Eidesstattliche Erklärung

Ich versichere, daß ich die vorliegende Arbeit selbständig und nur unter Verwendung der angegebenen Quellen und Hilfsmittel angefertigt habe. Alle Ausführungen, die wörtlich oder sinngemäß übernommen wurden, sind als solche gekennzeichnet.

Diese Arbeit wurde bisher weder im In- noch im Ausland in dieser oder ähnlicher Form in einem Prüfungsverfahren vorgelegt.

Halle (Saale), den 26 Oktober, 2004 Serhiy Vasnyov